CHAPTER IV

RESULTS AND DISCUSSION

Part I: Preparation of Palladium Membrane Tube Reactor and Its Application in Dry Reforming.

It has already been realized that the advantage of defect free or dense membrane reactor over porous membrane reactor is its high selectivity [32]. In this study, palladium was a selected material for developing the dense membrane reactor using in dry reforming reaction due to its high selectivity for hydrogen. It was thus critical that the prepared dense palladium membrane should have no pin hole or cracked area at all.

The porous 316L stainless steel was chosen as a support since it has high resistance to corrosion and it is tougher and stronger than other materials, for example, ceramic and glass. In addition, the electroless plating technique was used for developing the thin film of palladium membrane on porous stainless steel by following the method of Mardilovich *et al.* [27]. The procedure of palladium plating by electroless plating is composed of 3 important steps: (1) surface cleaning of the support using alkali solution for degreasing, (2) surface activation by $SnCl_2$ solution and $PdCl_2$ solution for reducing the plating time, and (3) palladium plating by $Pd(NH_3)_4Cl_2$ solution. Prior to preparing the palladium membrane reactor, both normal and porous stainless steel square disks, 1x1 cm^2 and 0.1 cm thickness, were used in palladium plating process at various conditions in order to find the most appropriate condition for palladium plating. Then the porous stainless steel tube was treated using such procedures.

4.1 Preparation of palladium membrane disks

4.1.1 Surface activation of porous stainless steel disk

In this experiment, normal and porous stainless steel square disks were used. According to section 3.2.1, the disk was firstly cleaned with alkali solution. Without this step, the palladium plating could not be deposited successfully because of grease, oil, dirt, corrosion products, and others existing on the disk surface. After thoroughly washing with water and isopropanol, it was dried and oxidized in air in order to create a thin metal oxide layer on the disk surface. It was believed that with this treatment, a metal oxide layer could act as a barrier to metallic diffusion between porous stainless steel and palladium membrane later [41]. Though the oxidation was carried out under the same condition as reported by Mardilovich *et al.* [27] with in fact 2 hours longer, the existence of iron, nickel, chromium, and oxygen was detected on the disk surface as revealed by EDS spectrum shown in Figure 4.1.

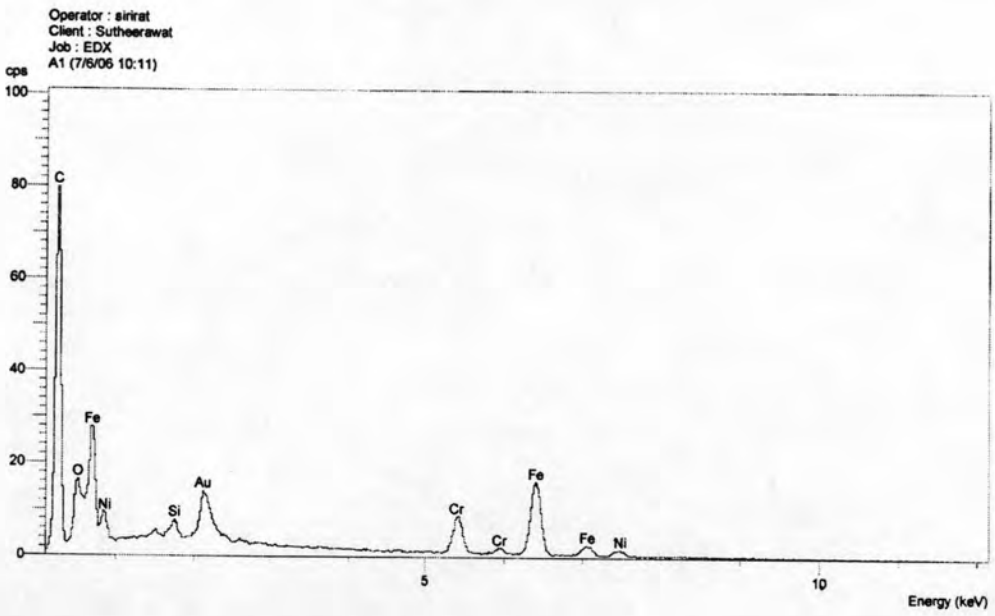

Figure 4.1 EDS spectrum of the porous stainless steel disk surface after oxidation at 450°C for 6 hours.

Next step was to activate the surface of stainless steel disk by preseeding with palladium nuclei in order to initiate an autocatalytic process of the reduction of a metastable metal salt complex on the target surface during electroless plating [65].

This was performed by the alternative treatments with $SnCl_2$ and $PdCl_2$ solutions repeatedly, as described in section 3.2.1.3, to ensure that the entire surface was activated thoroughly.

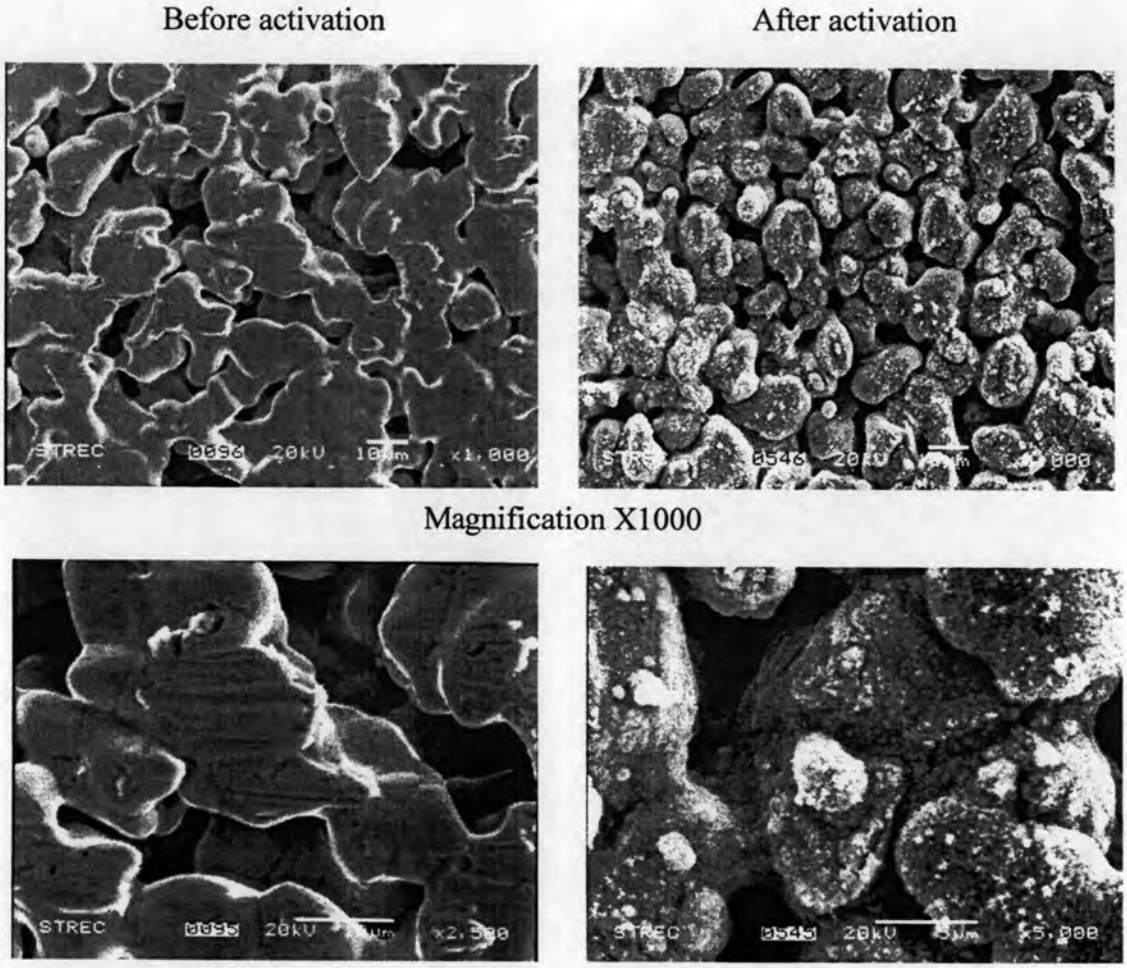

Figure 4.2 SEM micrographs of the porous stainless steel disk before and after surface activation.

The SEM micrographs of the porous stainless steel surfaces before and after surface activation, Figure 4.2 clearly indicated that the surface was effectively activated. A large number of seeds with relatively uniform particle on the support surface were observed. Moreover, the distribution of palladium and tin nuclei deposited on the surface of porous stainless steel disk was investigated by means of scanning electron microscope equipped with an energy dispersive X-ray (SEM-EDS) in mapping mode as shown in Figure 4.3.

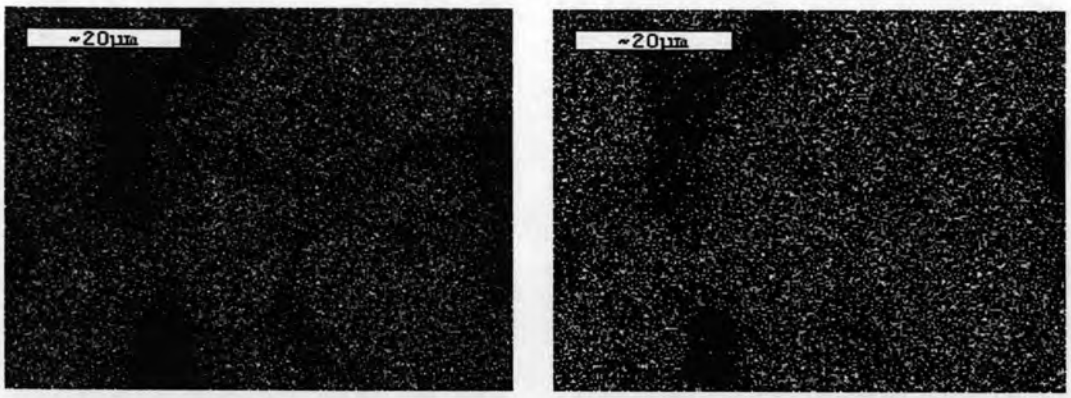

Palladium nuclei Tin nuclei

Figure 4.3 SEM-EDS micrographs of porous stainless steel disk surface after surface activation.

It can be seen that the palladium nuclei and the tin nuclei appear at the same location which is related to the lower right picture in Figure 4.2. It was proposed that tin nuclei were firstly created by decomposing from $SnCl_2$ to $Sn(OH)_{1.5}Cl_{0.5}$ with water according to equation 4.1, then the palladium nuclei were deposited on the tin nuclei *via* the redox process described by equation 4.2 [27].

$$2SnCl_2 + 3H_2O \longrightarrow 2Sn(OH)_{1.5}Cl_{0.5} + 3HCl \qquad 4.1$$

$$Pd^{2+} + Sn^{2+} \longrightarrow Pd^{0} + Sn^{4+} \qquad 4.2$$

This phenomenon was previously proved by Shu *et al* [4.5]. They reported that almost no palladium seed appeared on the surface of porous stainless steel disk when it was immersed only in the acidic palladium-containing solution.

Mardilovich *et al.* [27] had also demonstrated that a thicker activated layer resulted in a higher density of palladium nuclei on the support surface from ten activation cycles, but a diminished adhesion of further deposited palladium layers to the porous stainless steel support was observed. Similar observation was reported by Feidstein *et al.* [67]. Therefore six activation cycles were done in this study.

4.1.2 Palladium plating

After surface activation, the stainless steel disk was plated with palladium by electroless plating technique. The plating solution consisted of tetraaminepalladium (II) chloride, 28% ammonium solution, and ethylene diamine tetraacetate (EDTA). An excess of ammonium hydroxide was added which was necessary to stabilize the plating solution and to maintain the pH of the solution at 10. This plating solution was contained in a plating bath as shown in Figure 4.4.

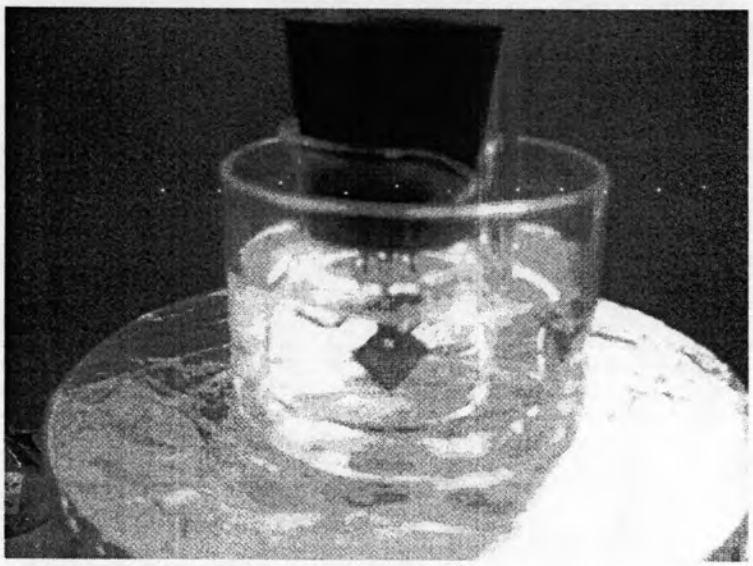

Figure 4.4 Palladium plating bath.

Anhydrous hydrazine, a reducing agent, was then added into the palladium plating solution when its temperature reached to 60°C. During the immersion of the disks some bubbling gases were observed due to the redox reaction as shown in Figure 4.5.

$$2Pd(NH_3)_4^{2+} + 4e^- \longrightarrow 2Pd^0 + 8NH_3 \qquad E^0=0.95\ V$$

$$N_2H_4 + 4OH^- \longrightarrow 4H_2O + N_2 + 4e^- \qquad E^0=1.12\ V$$

$$2Pd(NH_3)_4^{2+} + N_2H_4 + 4OH^- \longrightarrow 2Pd^0 + 4H_2O + N_2 + 8NH_3 \qquad E^0=2.07\ V$$

Figure 4.5 Redox reaction of palladium plating.

At the end of plating step, the disk was cleaned and dried. It appeared in silver-like color. This indicated that palladium plating had occurred. It was explained by several other research groups [4.2 - 4.4] that the reaction occurred on the surface of the support, and preferential around the palladium seeds. The occurrence was initiated by the reaction of hydrazine with hydroxide ions forming nitrogen gas and water with simultaneous release of electron. The electrons were transferred across the palladium island and used for reducing Pd^{2+} complex into palladium metal. The palladium metal was deposited onto the nuclei resulting in growth. Nitrogen and ammonia gases were concomitantly evolved as bubbles during the plating process. By testing in a separate experiment for plating the reactor tube, which the plating cell was used, with wet red litmus paper at the outlet of the plating cell, the blue color on litmus paper was suddenly appeared. It was thus another clue for the occurrence of redox reaction. Figure 4.6 demonstrates the schematic diagram of the redox reaction taken place in palladium plating step.

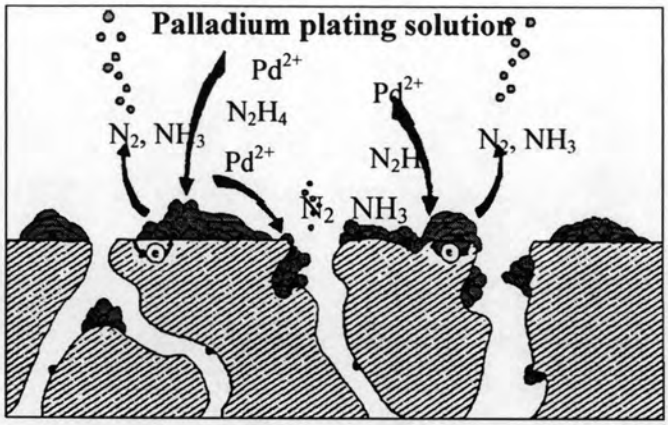

(a) Early stage.

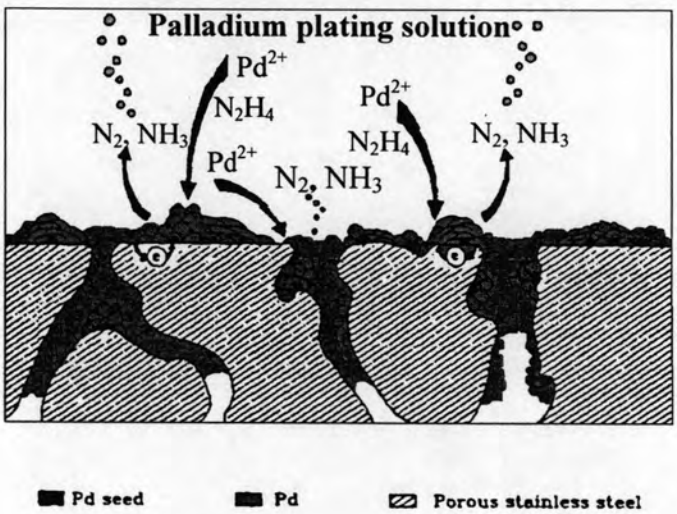

(b) Extension time.

Figure 4.6 Schematic diagram of palladium deposition process.

The evidence of palladium plating was also shown by SEM micrographs of porous stainless steel disk after surface activation then before and after palladium plating as revealed in Figure 4.7.

Before activation

After activation

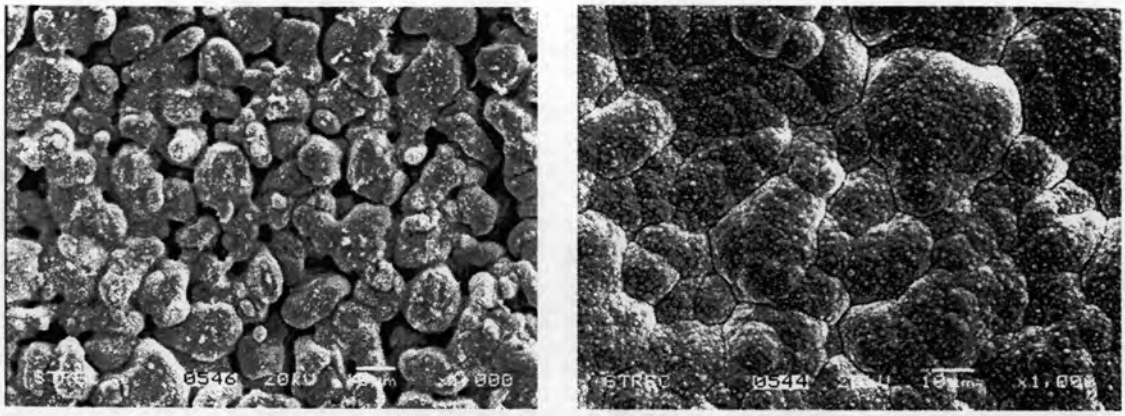

Magnification x 1000

Before activation

After activation

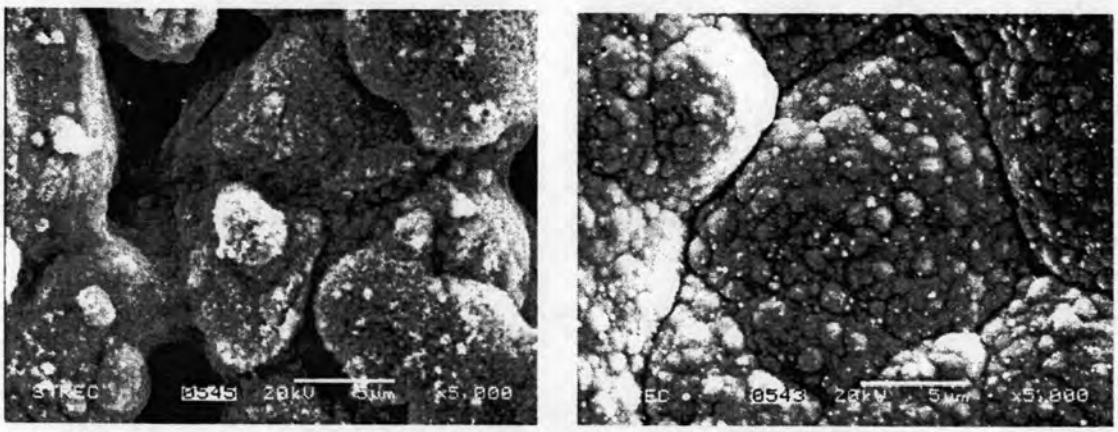

Magnification x 5000

Figure 4.7 SEM micrographs of the activation surface of porous stainless steel before and after palladium plating.

It obviously showed that the smooth surface was obtained resulting from palladium deposition onto the disk surface until a certain thickness was developed. At this point, the reinvestigation for the metal composition at the disk surface by EDS revealed the appearance of palladium only as exhibited in Figure 4.8.

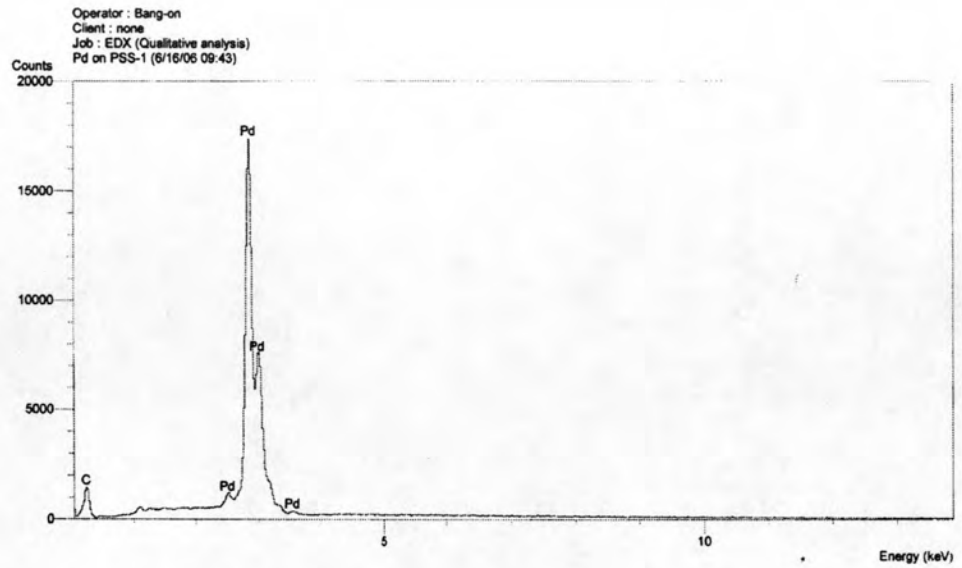

Figure 4.8 EDS spectrum of porous stainless steel disk surface after palladium plating.

In general, the thickness of palladium layer can simply be determined by weighing the disk and calculation. Three square porous stainless steel disks after activation were weighed before palladium plating step in Figure 4.9.

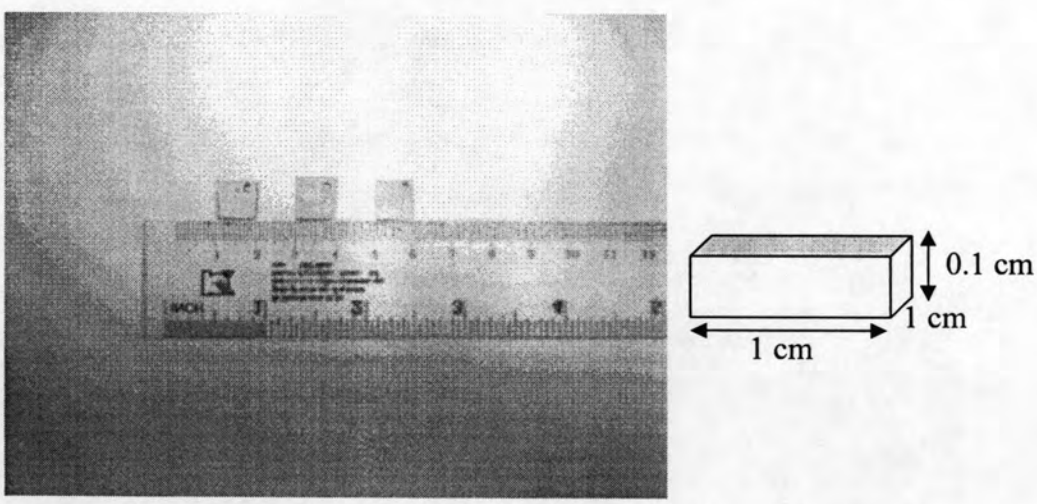

Figure 4.9 Square porous stainless steel disks with schematic dimension.

After palladium plating at different plating time, the plated disks were weighed again. The calculation for the thickness of palladium layer was done by using the following equation 4.3.

$$\text{Pd thickness}(\mu m) = \left(\frac{\text{plateddisk weight} - \text{initialdisk weight}}{\text{surface area of disk} \times \text{densityof palladium}} \right) \times 10^4 \qquad 4.3$$

Where

density of palladium = 12.02 g/mL

surface area = 4(0.1x1)+2(1x1)= 2.4 cm^2

It was assumed that the gained weight of the disk came from plated palladium only and the entire disk surfaces were plated evenly. In addition, the palladium layer thickness of these 3 disks was measured from their SEM micrographs as shown in Figure 4.10. Both measuring methods showed that the palladium layer thickness increased with increasing plating time as illustrated in Table 4.1. It can be seen that the palladium layer thickness measured by weighing is in the thickness range determined by SEM. Therefore, the measurement of palladium layer thickness by weighing could be acceptable.

Table 4.1 Determination of palladium layer thickness on porous stainless steel disks

Disk number	Plating time (min)	Disk weight (g)		Palladium layer thickness (μm)	
		Before plating	After plating	weighing	SEM
1	360	0.8792	0.8974	6.3080	5.0-7.5
2	560	0.8974	0.9260	9.9130	7.5-10.0
3	660	0.9260	0.9597	11.6810	10.0-12.5

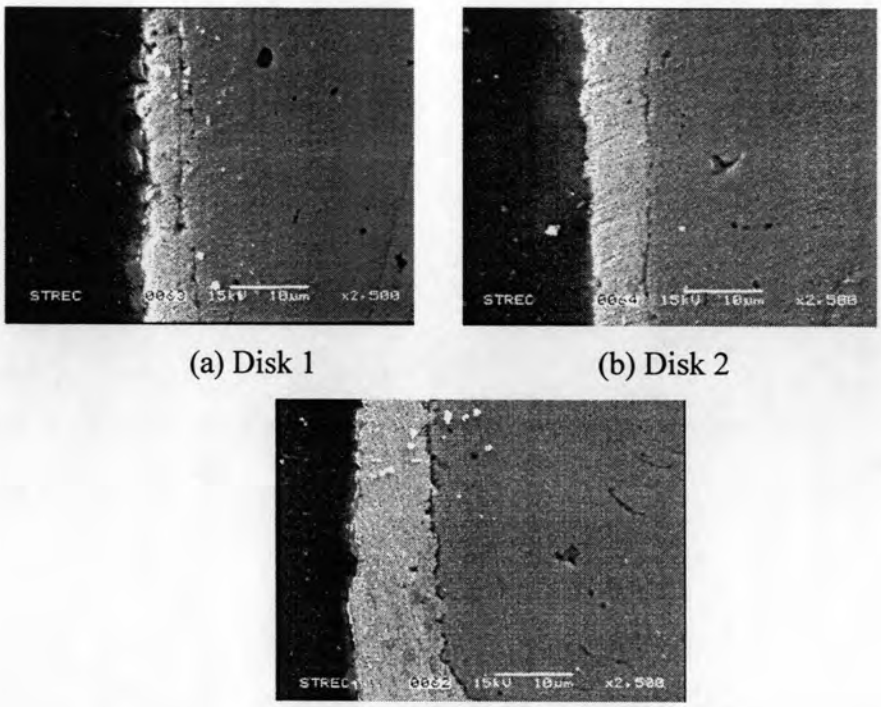

(a) Disk 1 (b) Disk 2

(c) Disk 3.

Figure 4.10 SEM micrographs of cross-section palladium plated porous stainless steel disks.

4.2 Preparation and characterization of palladium membrane reactor tube

The porous 316L stainless steel tubes, 9 mm in outer diameter, 70 mm long and 1 mm wall thickness, were used as the support for palladium membrane in this experiment. These porous stainless steel tubes had the average pore size 0.1 μm and 17% porosity. The porous 316L stainless steel tube welded to non-porous stainless steel tube was commercially available.

In this study, two tubes were used for preparing the palladium membrane reactor tubes, Tube 1 and Tube 2. They were subjected to surface cleaning with alkali solution, surface activation using $SnCl_2/PdCl_2$ solution, and finally palladium plating by palladium complex solution as described in section 3.2.1.3. The palladium plated area covered the entire porous stainless steel and some parts of the non-porous stainless steel at both sides of the tube as shown in Figure 4.11.

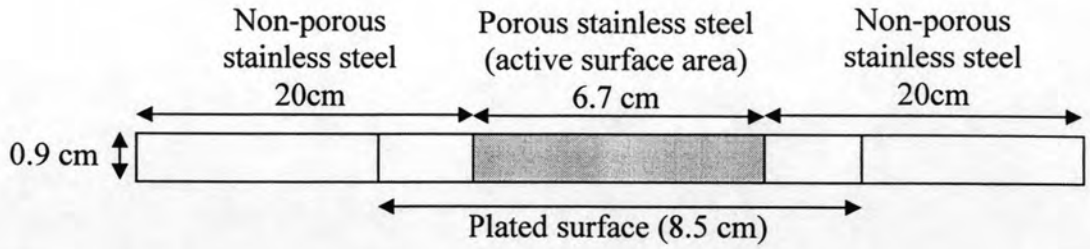

Figure 4.11 Palladium membrane reactor tube dimension.

Before plating, the tube was weighed and subjected to the helium flux measurement using helium flux testing cell in Figure 4.12 as described in section 3.2.2.2. After each time of plating, the tube was weighed and subjected to helium flux measurement again until no more helium flux was detected from the outlet of helium flux testing cell indicating that palladium membrane had been covered completely on the porous stainless steel area.

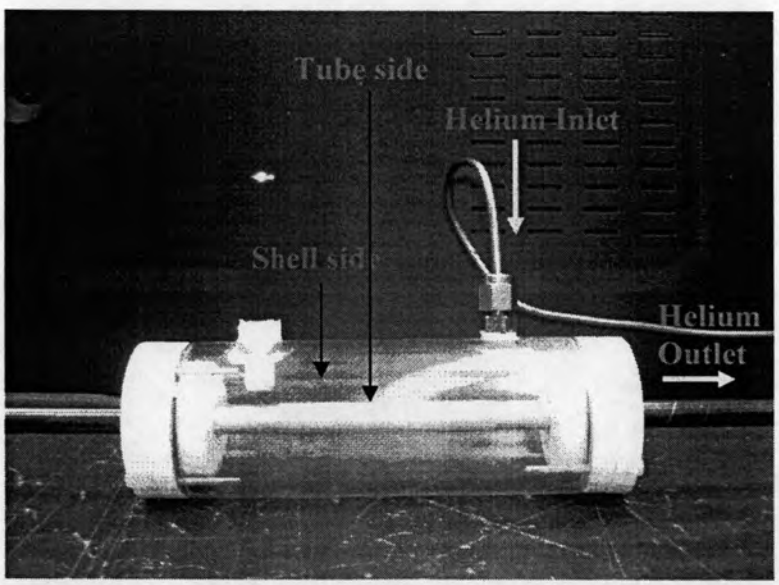

Figure 4.12 Helium flux testing cell.

By measuring the flow rate of helium gas at the outlet, helium flux can be calculated by using equation 4.4

$$\text{He flux}\,(\text{m}^3/\text{m}^2\text{h}) = \left(\frac{\text{Flow rate of He in tube side (ml/min)}}{\text{Active surface area of palladium (cm}^2)}\right) \times 0.6 \qquad 4.4$$

If helium at the cell outlet was detected, it meant that palladium plating was not completely done and the palladium membrane was not dense. The results were presents in Table 4.2.

Table 4.2 Palladium layer thickness and helium flux measurement of palladium membrane reactor tube

Number of Pd plating	Tube Weight after plating (g)	Palladium weight (g)	Pd Thickness* (μm)	He flux (m^3/m^2h)
Tube 1				
Before Pd plating	129.99	-	-	179.56
After plating				
1	130.27	0.28	5.99	115.10
2	130.50	0.51	10.91	0.0021**
3	130.78	0.79	16.90	0.0007**
4	130.89	0.90	19.25	Dense**
Tube 2				
Before Pd plating	130.47	-	-	173.77
After plating				
1	130.66	0.21	4.49	52.05
2	130.89	0.44	9.41	0.0257**
3	131.07	0.62	13.26	0.0005**
4	131.28	0.82	17.54	Dense**

Remark: * by calculation using equation 4.3 which would give the approximate thickness

** He flux measured by using capillary flow meter

Before plating, helium flux was measured to be 180 m^3/m^2h for Tube 1 and 173 m^3/m^2h for Tube 2. This implied that Tube 1 had more pores than Tube 2. After each plating, higher palladium layer thickness was obtained and lower helium flux at the cell outlet was found. Finally, no helium flux was obtained after 4 times of plating in both cases.

Accordingly, two dense palladium membrane reactor tubes were successfully prepared by using electroless plating technique with the calculated palladium layer thickness 19.3 μm for Tube 1 and 17.5 μm for Tube 2.

4.3 Performance testing of palladium membrane reactor tube

4.3.1 Hydrogen permeation flux and selectivity coefficient

The two prepared palladium membrane tubes were evaluated for their performance on hydrogen permeation by measuring the hydrogen permeation flux at various pressure difference between shell side and tube side. This experiment was performed at higher temperature than 300°C. This is important since palladium layer can be damaged by hydrogen at the temperature lower than 300°C which is known as hydrogen embrittlement. Figure 4.13 presents the photograph of an embrittled palladium membrane caused by a small amount of hydrogen contaminated in helium during flushing the palladium membrane reactor at room temperature.

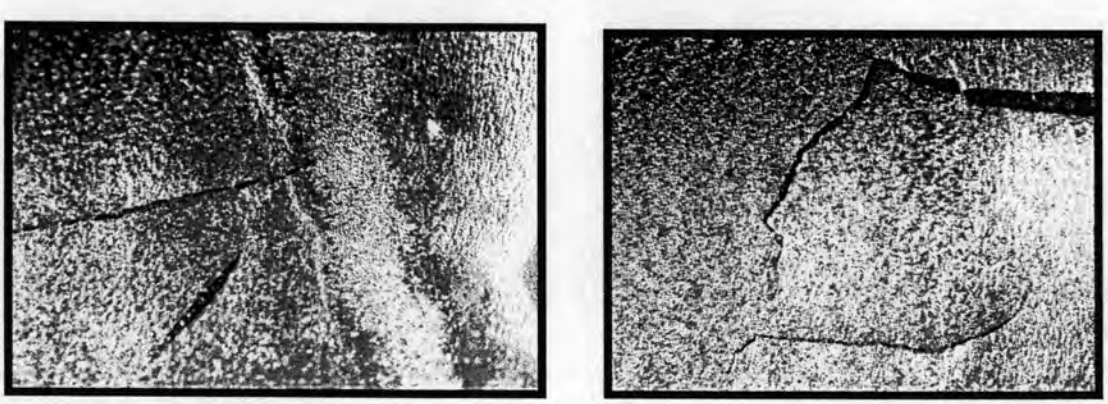

Figure 4.13 The crack taking place on the membrane surface because of the H_2 embrittlement.

The experimental setup was shown in Figure 4.14. The measurement of H_2 permeate flow rate was started after the required temperature was reached and the flow rate of H_2 permeate was observed to be constant as described in section 3.2.3.3.

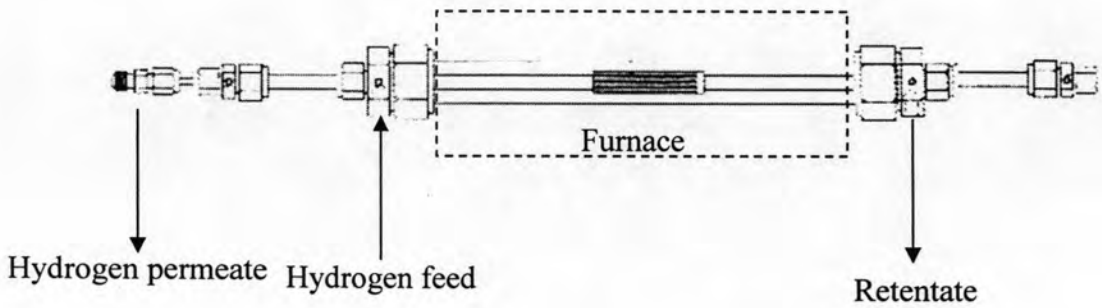

Figure 4.14 Schematic diagram of H_2 permeation experimental setup.

At one temperature, the hydrogen permeation flux could be calculated for each pressure difference between shell side and tube side of the reactor. Figure 4.15 is the plot of hydrogen permeation flux and the difference of the square root of pressure in shell side and tube side of the tube reactor. For each temperature, hydrogen permeation flux increased with increasing pressure difference. At higher temperatures more hydrogen permeation flux was obtained. Their results clearly indicated that hydrogen permeation depended on both temperature and the pressure differences in shell and tube sides.

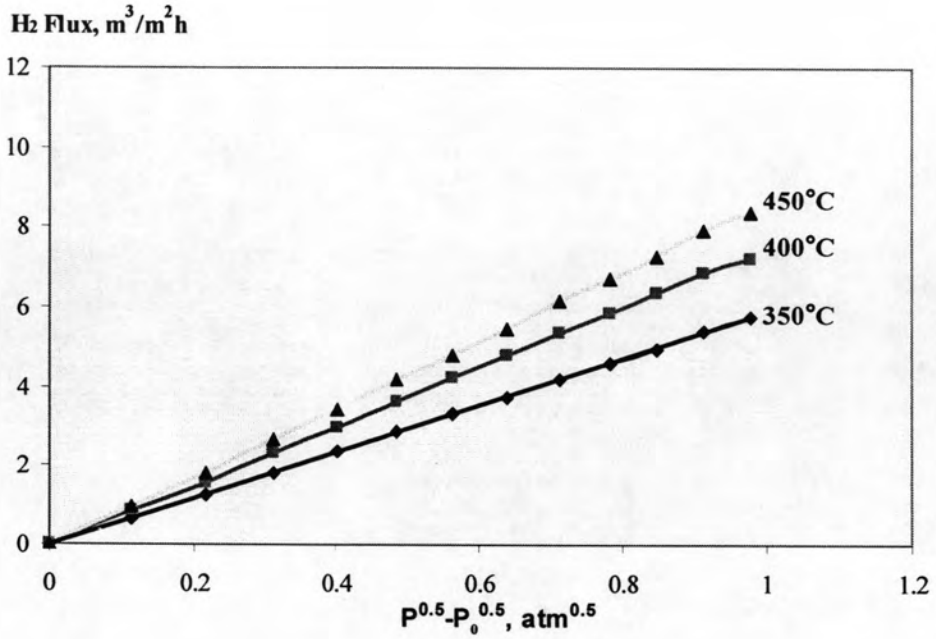

(a) Tube 1, 19.5μm thickness

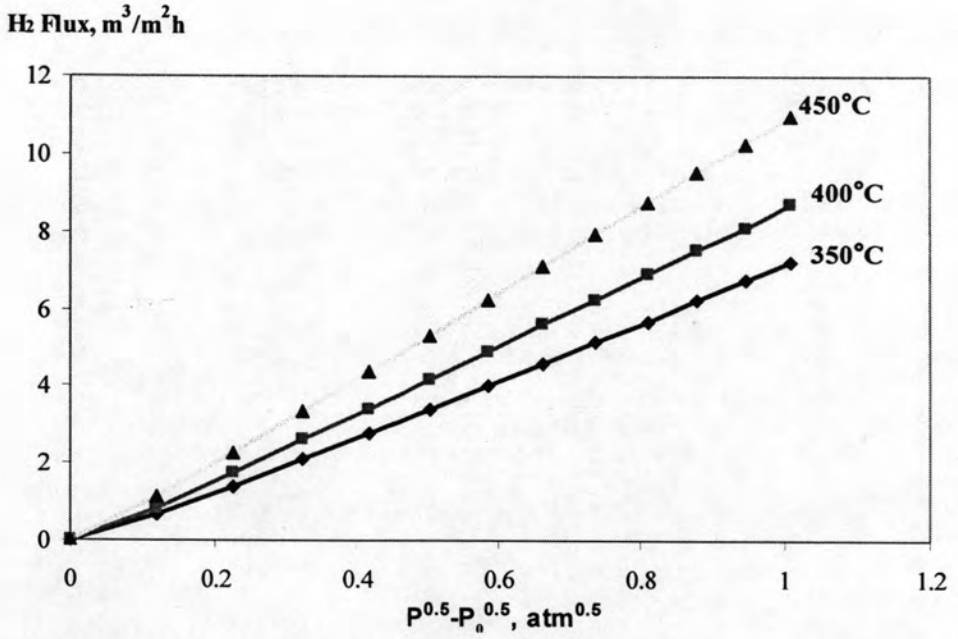

(b) Tube 2, 17.3μm thickness

Figure 4.15 The relation of hydrogen permeation flux and the difference of the square root of pressure in shell side and tube side at various temperatures.

It was found that hydrogen permeation flux at 350°C, 400°C, and 450°C and the square root of pressure difference 0.4 atm was 2.3, 3.0, and 3.4 $m^3(STP)/m^2.h$ for Tube 1 and 2.8, 3.4, and 4.4 $m^3(STP)/m^2.h$ for Tube 2, respectively. The relationship

between the hydrogen permeation flux and the square root of pressure difference $(P^{0.5} - P_0^{0.5})$ was plotted in Figure 4.15 which showed a linear relationship between the hydrogen flux and the difference of the square root of pressure. This is clear indicated that the Sieverts' law was followed and the slope of the lines gives the permeance of the membrane, which are 5.9, 7.5, and 8.6 $m^3(STP)/(m^2.h.atm^{0.5})$ for Tube 1 and 7.3, 8.7, and 11.0 $m^3(STP)/(m^2.h.atm^{0.5})$ for Tube 2, The hydrogen permeation also showed that the mechanism of hydrogen gas diffusing through the bulk of palladium layer is the solution-diffusion mechanism. Moreover, the rate-determining step for the hydrogen permeation of tube1 and tube 2 was the hydrogen diffusion through the bulk of palladium layer. It meant that both tubes were the dense palladium membranes.

Normally, the ideal separation factor or selectivity coefficient ($\alpha^*_{i/j}$), is defined as the ratio of the fluxes of two pure gases, i and j, as follows:

$$\alpha^*_{i/j} = \frac{J_i}{J_j} \qquad 4.7$$

For this study, hydrogen and helium were used. It was found that the selectivity coefficient at pressure difference 1 atm for Tube 1 could not be calculated but should be high because of no detected helium flux. The selectivity coefficient of Tube 2 was 78,270, 74,923, and 8,604 at 350°C, 400°C and 450°C, respectively. Tube 2 had lower selectivity than Tube 1. Moreover, the higher temperature increased, the lower selectivity coefficient decreased. The attribution to this result might be due to higher thickness of Tube 2. This probably caused by the generation of the micro-crack on membrane surface at higher temperature. However, the selectivity coefficient of Tube 1 was still high even the different pressure was upto 3 atm shown in Appendix A.

4.3.2 Activation Energy

Since, Tube 1 and Tube 2 were dense palladium membrane tubes, the mechanism of hydrogen diffusion was the solution-diffusion. In order to evaluate the activation energy of hydrogen permeation through the palladium membrane, the activation energy value was calculated from the slope of the plot between the

hydrogen permeance and the inverse temperature in Kelvin degree. These plots were exhibited in Figure 4.16. It was found that the activation energies were 15.4 kJ/mol for Tube 1 and 14.3 kJ/mol for Tube 2.

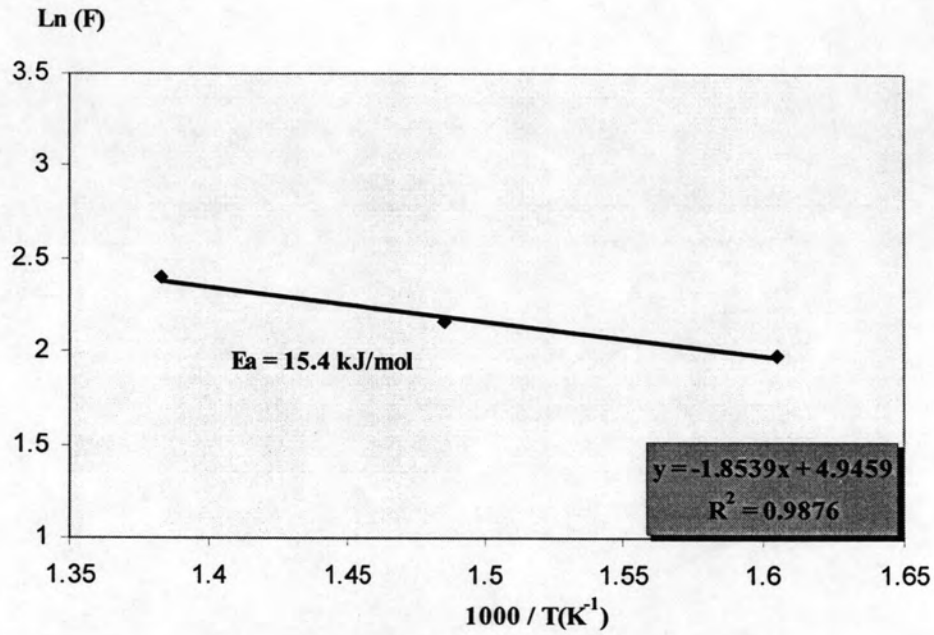

Tube 1, 19.5 μm thickness

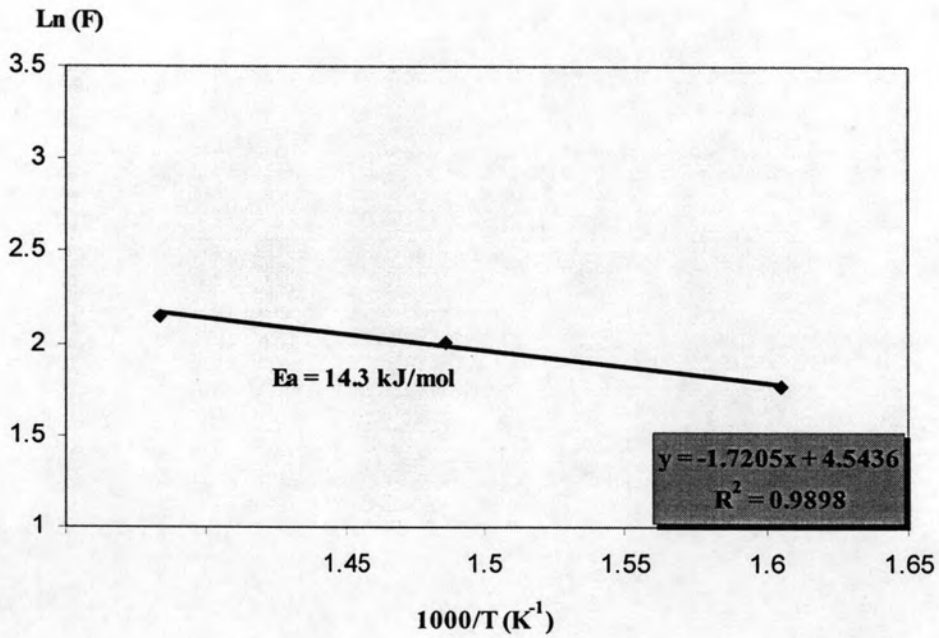

Tube 2, 17.3μm thickness

Figure 4.16 Arrhenius relations between the hydrogen permeance and inverse temperature.

4.3.3 Performance comparison of the prepared palladium membrane reactor tube with Mardilovich's tube

Table 4.3 shows that Tube 1 and Tube 2 were significantly better than Mardilovich's tube for both selectivity and permeance. However, the selectivity coefficient of Tube 1 was higher than Tube 2.

Table 4.3 Performance comparison of the prepared palladium membrane reactor tubes with Mardilovich's tube

	Tube 1	Tube 2	Mardilovich's tube[1]
Thickness (μm)	19.3	17.5	19-28
Hydrogen permeation flux (m^3/m^2h), ΔP= 1 atm			
Hydrogen gas[2]			
350 °C	2.35	2.78	2-4
400 °C	3.00	3.41	-
450 °C	3.44	4.37	-
Helium gas[3]			
350 °C	0.0000	0.00003	0.002
400 °C	0.0000	0.00004	-
450 °C	0.0000	0.0004	-
Selectivity coefficient, ΔP= 1 atm			
350 °C	Higher	78,270	1,000-2,000
400 °C	Higher	74,923	-
450 °C	Higher	8,604	-
Permeance ($m^3/m^2h\ atm^{0.5}$)			
350 °C	5.88	7.26	7.8
400 °C	7.46	8.71	-
450 °C	8.60	10.98	-
Activation energy (kJ/mol)	15.4	14.3	16.4

Remark 1 Mardilovich's tube using 316L porous stainless steel which was the same with this work and the palladium thickness was calculated in the same way.

2 using the digital flow meter

3 using the capillary bubble flow meter

It was found that the performance of Tube 1 and Tube 2 prepared for this study was significantly better than the reference one, especially selectivity coefficient.

4.4 The performance of palladium membrane reactor for dry reforming reaction

4.4.1 Theoretical calculation of predicted values for thermodynamics equilibrium conversion in dry reforming

It should be noted that the main reaction in dry reforming takes place according to equation 4.8.

$$CH_{4(g)} + CO_{2(g)} \rightleftharpoons 2H_{2(g)} + 2CO_{(g)} \qquad 4.8$$

$$\Delta H_f^0 = 247 kJ/mol \text{ and } \Delta G_f^0 = 61770 - 67.32T$$

This is an increment in the number of moles produced, such that operation at high pressure does not favor the progress of the reaction. The theoretical conversion values were calculated for an equimolar mixture of methane (CH_4) and carbon dioxide (CO_2) from the Gibbs free energy value of reactants and products at different temperature [35] according to the stoichiometry of equation 4.6. The detail of calculation was exhibited in Appendix B and the calculated values are shown in Table 4.4.

Table 4.4 Calculated values for thermodynamics equilibrium conversion of dry reforming as a function of the reaction temperature

Temperature, °C	Conversion, %	
	CH_4	CO_2
350	1	1
400	3	3
450	8	8
500	15	15

Remark CH_4:CO_2 (1:1) operated at the atmospheric pressure

From Table 4.4, it clearly shows that at higher reaction temperature, the conversion increases. It implies that if the experimental results become the same as the calculated values CH_4:CO_2 converted equal to 1 using the same condition parameters, no other side reaction occurs in the experiment and *vice versa*. Normally, the known side reaction in dry reforming is reverse water gas shift as presented in equation 4.9 [33].

$$H_{2(g)} + CO_{2(g)} \rightleftharpoons H_2O_{(l)} + CO_{(g)} \qquad 4.9$$

$$\Delta H_f^0 = 41 kJ/mol \text{ and } \Delta G_f^0 = -8545 + 7.84T$$

Due to the occurrence of this parallel reaction, CO_2 conversion usually exceeds that of CH_4, obtained H_2:CO ratios are typically <1.0, and water appears as byproduct. However, if hydrogen is removed efficiently from the reaction once it is formed, it is possible to prevent this side reaction. Then the reaction of CH_4:CO_2 converted will be always equal to one. In this study, the palladium membrane reactor tube had been used for this purpose which was discussed in next section.

4.4.2 Dry reforming reaction

To evaluate the performance of palladium membrane tube reactor, the methane and carbon dioxide conversion in dry reforming using conventional tube reactor and palladium membrane tube reactor were compared. An equimolar mixture of CH_4 and CO_2 with total pressure of 1 atm. The atmospheric pressure was used and the reaction temperature was varied from 350 to 450°C. The reaction temperature is not allowed to be higher than 450°C in order to prevent the intermetallic diffusion from porous stainless steel to palladium membrane. In addition, the reaction temperature cannot be lower than 350°C because the palladium membrane surface will be damaged due to hydrogen embrittlement.

4.4.2.1 The analysis of gas composition from reaction by GC-TCD

In this work, the reaction was monitored by on-line gas chromatography using two analytical columns containing Hayesep Q and Molecular sieve 13x, in a

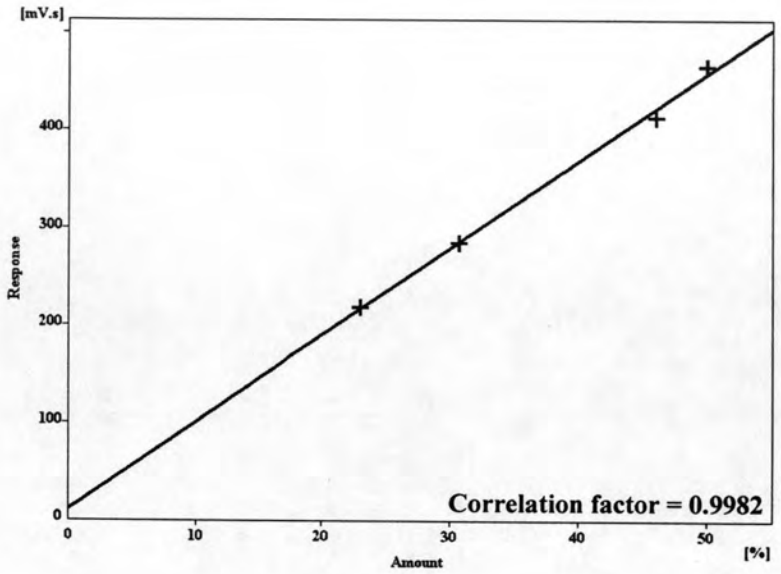

(a)

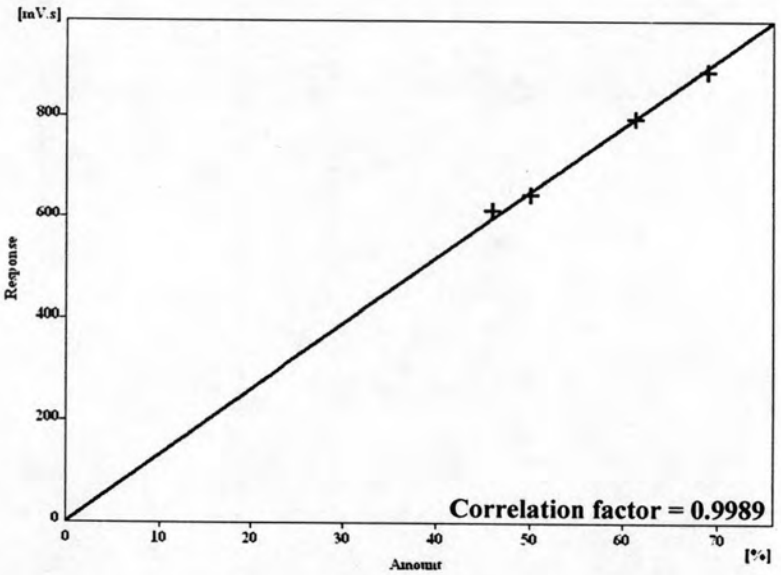

(b)

Figure 4.18 Calibration curves of (a) methane and (b) carbon dioxide.

It was found that the correlation factor (R^2) of calibration curve of both methane and carbon dioxide were 0.9982 and 0.9989, respectively. They were higher than 0.995, implying that both calibration curves were accepted at the confidence level around 99.5%. From gas chromatograph, the area under the peak of CH_4 and CO_2 in both feed and the reaction can be converted into the corresponding amount of those calibration curves. Accordingly, the percentage of methane and carbon dioxide conversions were calculated by equations 4.10 and 4.11.

sequence. Since dry reforming involves with CH_4, CO_2, CO, and H_2, gas chromatograph equipped with thermal conductive detector was used. The Hayesep Q column could separate the higher molecule such as CH_4 and CO_2 and the Molecular sieve 13x column would separate the small molecule like CO and H_2. Figure 4.17 presents the chromatogram of the gas mixture from the reactor shell side outlet.

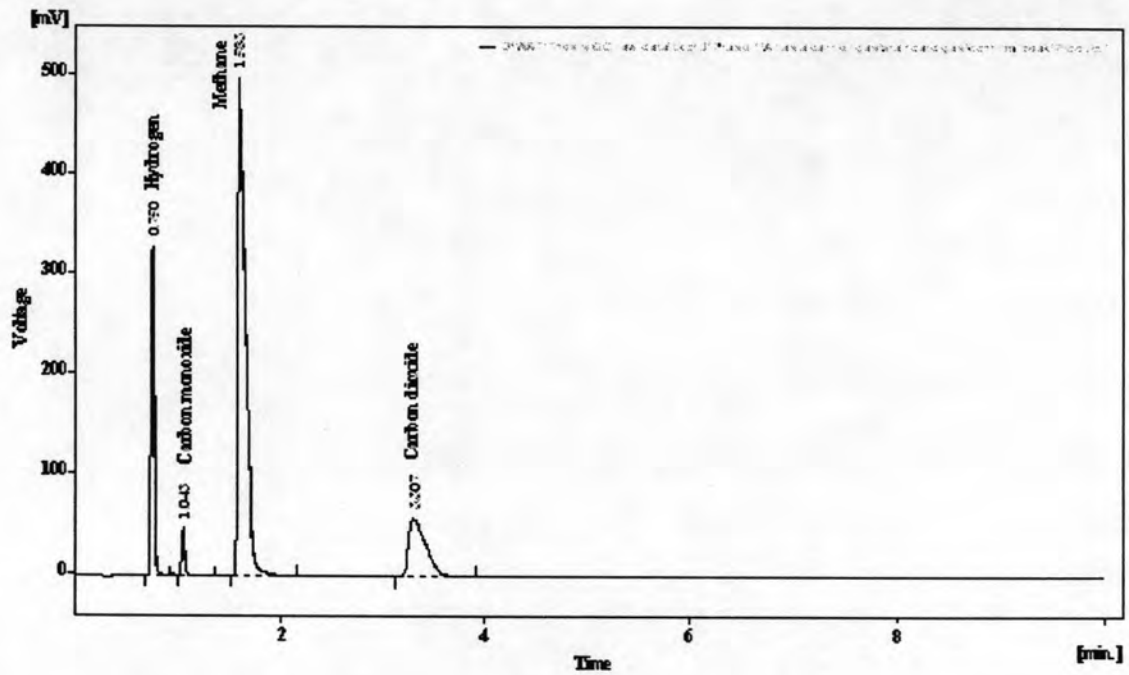

Figure 4.17 The GC chromatogram of gas mixture in the reaction from the reactor shell side.

The suitable GC condition was found to be varied by several factors such as temperature and flow rate of carrier gas. Four completely resolved peaks were at retention time 0.750, 1.043, 1.583, and 3.307 min corresponding to H_2, CO, CH_4, and CO_2, respectively. For quantitative analysis, two different techniques were applied. The external standard technique was used for quantitative analysis of CH_4 and CO_2 due to the availability of four gas mixtures with known composition. Figure 4.18a and b were the calibration curves of methane and carbon dioxide.

$$CH_4\ conversion,\% = \left(\frac{F_{CH4,Feed} - F_{CH4,Out}}{F_{CH4,Feed}} \right) x100 \qquad 4.10$$

$$CO_2\ conversion,\% = \left(\frac{F_{CO2,Feed} - F_{CO2,Out}}{F_{CO2,Feed}} \right) x100 \qquad 4.11$$

4.4.2.2 Dry reforming using conventional tube reactor

In order to find the proper operation condition for applying on palladium membrane reactor such as the optimum feed of reactant, the proper reaction time and the suitable catalyst type, it was performed by using the conventional tube reactor. To investigate the blank data for confirming that the experimental set up has no effect on the reaction, the gas mixture of methane and carbon dioxide (1:1) was fed in the conventional tube reactor, stainless steel tube, with flow rate at 20 mL/min and 60 mL/min without catalyst. The reaction was observed at 450°C, pressure 1, 2 and 3 atm during 72 hours. It was found that both pressure of reactor and flow rate of feed of mixed gas was varied, without catalyst not only the conversion of methane and carbon dioxide but also yield of hydrogen and carbon monoxide could not be observed. It could be concluded that there was no reaction taking place in the reactor at all if there was no catalyst.

4.4.2.2.1 The effect of catalyst type

In this study, three types of catalysts were used, *i.e.*, 0.5%Ru/Al_2O_3, 0.5%Pt/Al_2O_3, and 1.0%Pt/Al_2O_3. In order to obtain the suitable catalyst, 1.0 g of these catalysts were carried out in the conventional tube reactor with 20 mL/min feed flow rate of the gas mixture of methane and carbon dioxide (1:1) at 450°C, pressure 1 atm. The results are exhibited in Figure 4.19.

When 0.5%Ru/Al_2O_3, 0.5%Pt/Al_2O_3, and 1.0%Pt/Al_2O_3 were used, the percentages of methane conversions were 5.1%, 5.2%, and 6.5%, respectively. Besides, the percentages of carbon dioxide conversions were 7.5%, 7.7%, and 9.7%.

It was found that the higher temperature was, the higher conversion and yield were. It also indicated clearly that the conversions of methane and carbon dioxide between 0.5%Ru/Al_2O_3 and 0.5%Pt/Al_2O_3 closed to each other. Furthermore when the platinum loading in Pt/Al_2O_3 catalyst was increased, the higher conversion and yield were obtained. This agreed with Andrew *et al.* [68] and Paturzo *et al.* [69]. As the above mention, 1.0%Pt/Al_2O_3 was chosen for the next experiment. Moreover, the CH_4:CO_2 ratio was always less than one. It meant that there was some side reactions taking place. The possible side reaction should be the reverse water gas shift reaction as Equation 4.9 but the water content cannot be detected in this analysis condition. In case of carbon deposition, all catalysts after performed the reaction at 450°C pressure 1 atm were also investigated by means of thermal gravimetric analyzer. There was no carbon detected. Normally carbon will be formed from methane cracking of the Boudouard reaction as Equation 2.2 in the temperature range of 557–700°C [70].

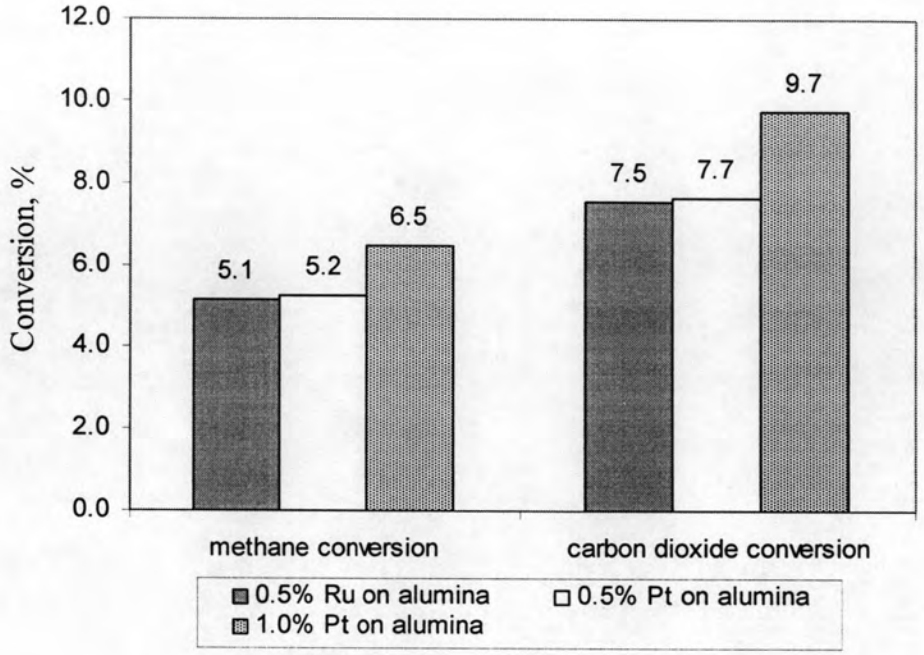

(a)

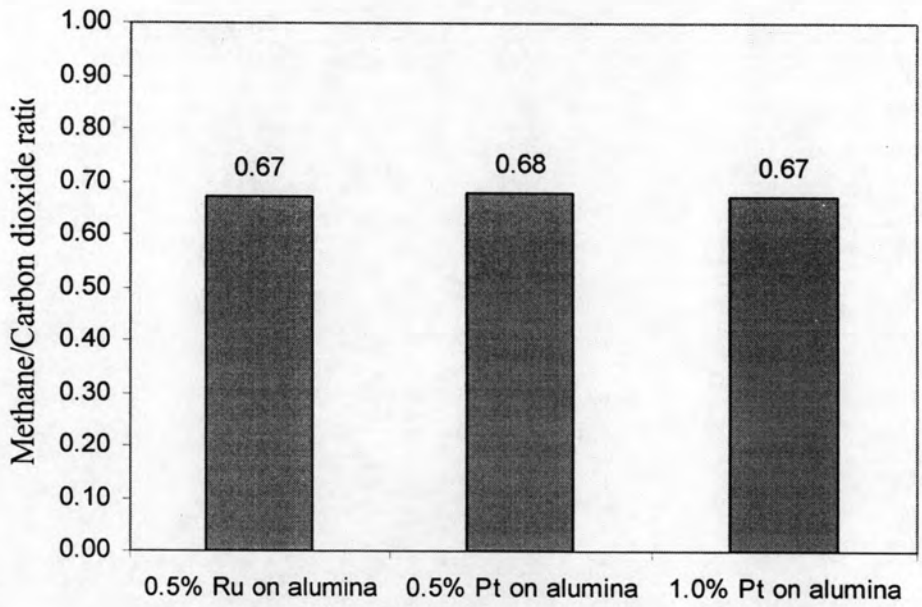

(b)

Figure 4.19 The effect of types of catalysts in dry reforming reaction at 450 °C, pressure 1 atm (a) methane and carbon dioxide conversion (b) methane/carbon dioxide ratio.

4.4.2.2.2 Dry reformimg stability

The catalyst stability was examined in the conventional tube reactor at 450°C with a CH_4/CO_2 ratio of 1:1, 20 mL/min flow rate, 1.0 g of 1.0%Pt/Al_2O_3 catalyst with 500 μm size packed in the reactor. The reaction was performed for about 86 hours. Figure 4.9 showed not only methane but also carbon dioxide conversion as a function of time. Both conversions started to be stable after the reaction proceeded for about 5 hour. In order to make a correct comparison of the reactions in both the palladium membrane and conventional tube reactors, the activity of the catalyst should be in stable state during the measurements.

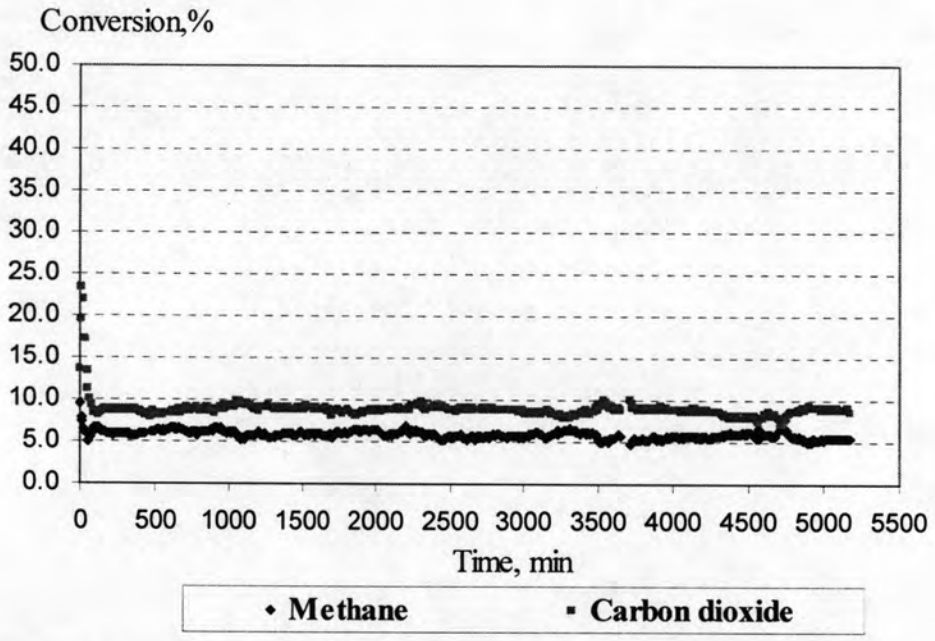

Figure 4.20 Dry reforming reaction using 1.0%Pt/Al_2O_3 at 450 °C, pressure 1 atm at various time.

From Figure 4.20, the conversions of methane and carbon dioxide were constant for long time at the operation temperature of 450°C. From now on, all the experiments would be done from2-20 hours for data collection.

4.4.2.2.3 The effect of total flow rate of methane and carbon dioxide

This preliminary experiments were carried out to find a suitable condition of feed flow rate. Considering the effect of the total flow rate of gas mixture of CH_4/CO_2 (1:1), it was varied from 5 mL/min. The reaction was performed by using 1.0 g of 1.0%Pt/Al_2O_3 at 450°C, pressure 1 atm. The collected data from 2 hours to 20 hours were analyzed. All average data of conversion were exhibited in Figure 4.21.

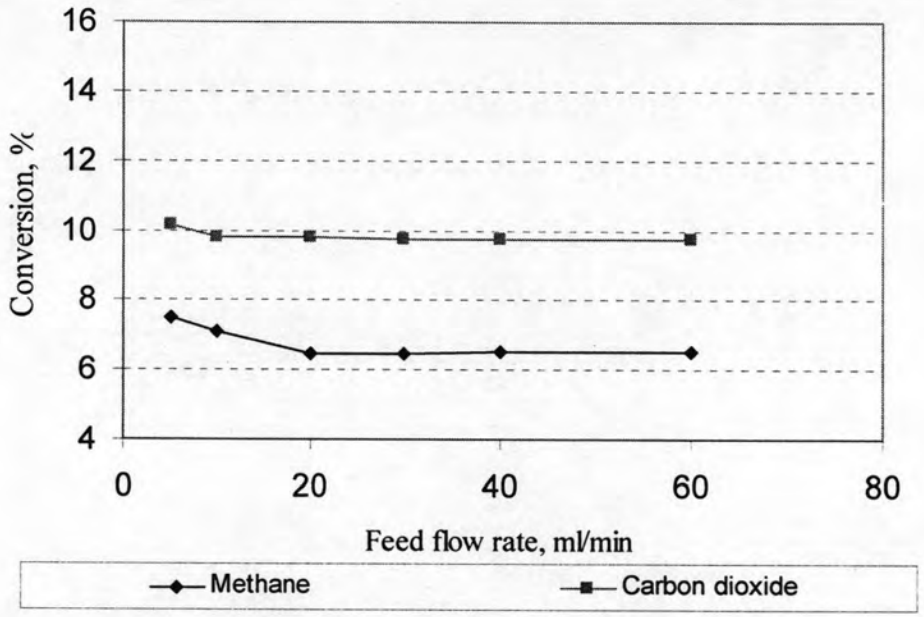

Figure 4.21 Effect of the total gas flow rate on the conversion and yield from the dry reforming.

It was found that at high flow rate, both methane and carbon dioxide conversions were very low because of not enough time for the reaction. However, they were constant at the flow rate of 20 mL/min. It meant that the reforming rate was independent of the gas velocity when the gas flow rate was higher than 20 mL/min. Therefore, in the following studies, the total flow rate was kept constant at 30 mL/min.

4.4.3 Dry reforming reaction using palladium membrane tube reactor

To evaluate the performance of palladium membrane tube reactor, the methane and carbon dioxide conversion in dry reforming using conventional tube reactor and palladium membrane tube reactor were compared. An equimolar mixture of methane and carbon dioxide at the atmospheric pressure were used and temperature of the reaction was varied from 350°C to 450°C. The reaction temperature cannot be higher than 450°C in order to prevent the intermetallic diffusion from porous stainless steel support to palladium membrane. In addition, the reaction temperature can not be lower than 350°C because the palladium membrane surface will be damaged due to hydrogen embrittlement. Moreover, not only the effect of reaction temperature but also the effect of total pressure and sweep gas were investigated as following.

4.4.3.1 The effect of temperature

In order to evaluate the influence of reaction temperature on the methane conversion in dry reforming reaction, not only palladium membrane tube reactor but also conventional tube reactor was investigated. The reaction was carried out using CH_4/CO_2 (1:1) with 1.0g of 1.0%Pt/Al_2O_3 catalyst at various reaction temperature from 350°C to 450°C at pressure 1 atm. Figure 4.22 presents the conversion as a function of temperature.

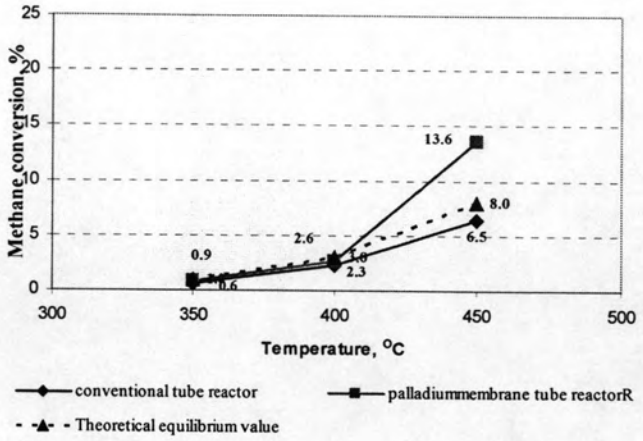

(a)

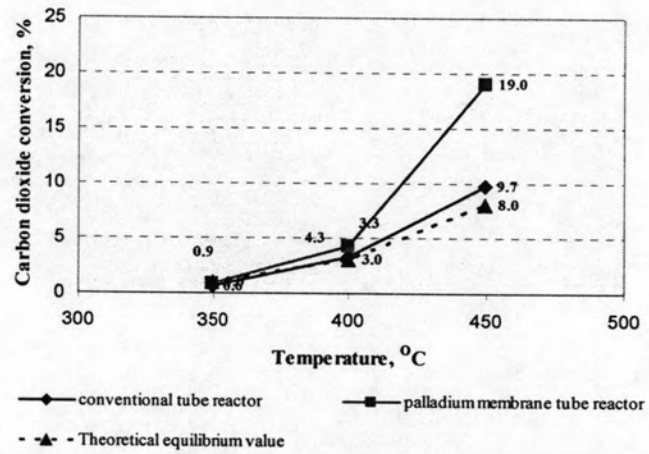

(b)

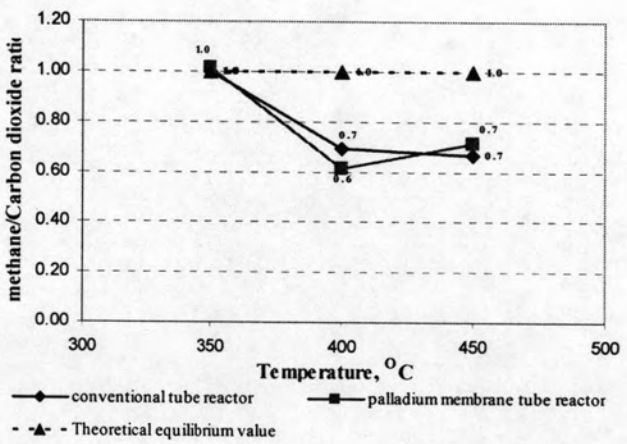

(c)

Figure 4.22 CH_4 conversions as a function of temperature; (a) methane conversion, (b) carbon dioxide conversion, (c) methane / carbon dioxide ratio.

When the reaction temperature was raised, the conversion of both methane and carbon dioxide was increased. It is because the dry reforming is an endothermic reaction. From Figure 4.20(a), the methane conversion was changed from 0.6% to 6.5% for conventional tube reactor and 0.9% to 13.6% for palladium membrane tube reactor when the temperature was varied from 350-450°C. Moreover, the methane conversion using conventional tube reactor was lower than not only the methane conversion from theoretical but also from palladium membrane reactor. However, the methane conversion of dry reforming reaction using palladium membrane tube reactor was always higher than the theoretical one. It was because the hydrogen was removed from the reaction by diffusing through the palladium membrane. Especially at high temperature region, more hydrogen gas was produced in the reaction and removed from the palladium membrane reactor. Therefore, the methane conversion using palladium membrane tube reactor was always higher than conventional tube reactor.

From Figure 4.22 (b) the tendency of carbon dioxide conversion was similar to methane conversion. Figure 4.22 (c) presents the methane/carbon dioxide ratio. It was found that it closed to 1

Moreover, It was found that there were no carbons obtained on the catalyst carried at the reaction temperature from 350°C to 450°C. It was the same conclusion that the noble metal catalysts promisingly performed for reforming reaction without carbon formation [69].

4.4.3.2 The effect of total pressure

Since dry reforming of methane related gas phase reaction, the effect of pressure on the methane conversion of dry reforming was taken into account. Both the conventional tube reactor and palladium membrane tube reactor were performed by using 1.0 g of 1.0%Pt/Al_2O_3 at 450°C with 30 mL/min of feed flow rate of CH_4/CO_2 (1:1) except pressure varied as 0.5 atm, 1.0 atm, and 1.5 atm, respectively. Their results are exhibited in Figure 4.23.

From Figure 4.23 in case of conventional tube reactor, when total pressure was altered from 0.5 atm to 1.5 atm, the conversion of methane and carbon dioxide also decreased from 7.8% to 6.2 % and 11.5% to 9.6%, respectively. However, It indicated clearly that the conversions of both methane and carbon dioxide employing palladium membrane tube reactor were higher than the conventional tube reactor.

Unfortunately, both methane and carbon dioxide conversions using palladium membrane tube reactor declined when total pressure was increased. Commonly, when the palladium membrane tube reactor is employed the conversion may increase with pressure due to the selective removal of hydrogen by permeation with increasing of pressure. Thus the concentration of hydrogen permeated across of the palladium membrane layer in tube side is higher. It will affect the rate of hydrogen diffusing through the palladium layer is lest. Therefore, in this case the increasing of total pressure could not improve both the conversion of methane and carbon dioxide. To solve this problem the effect of sweep gas was investigated.

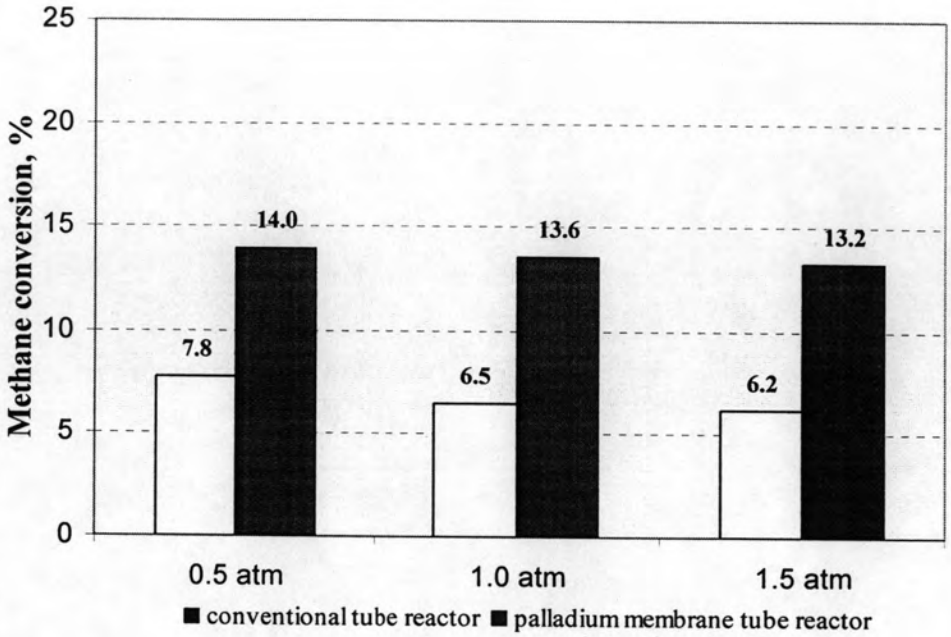

(a)

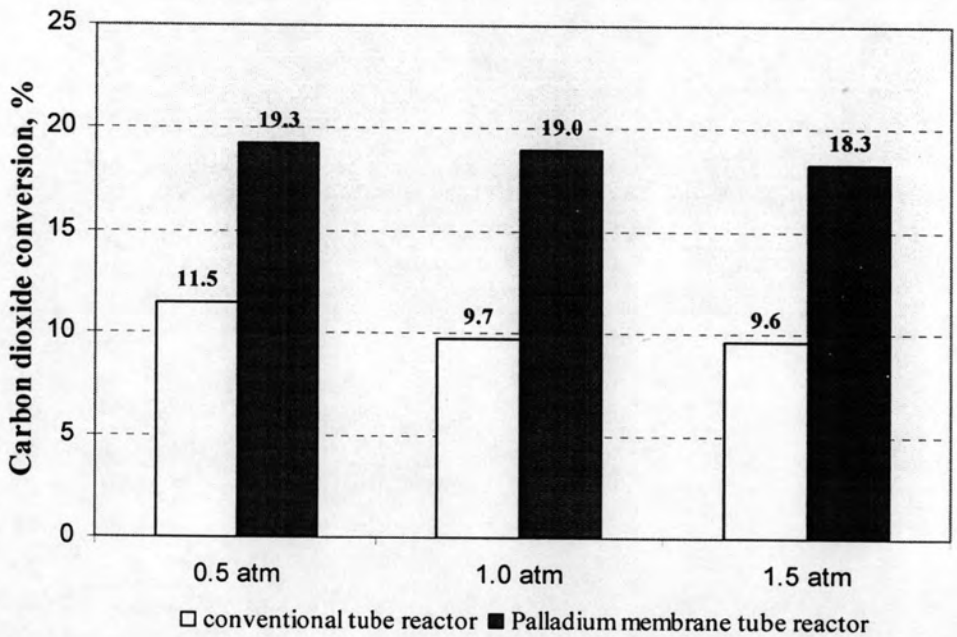

(b)

Figure 4.23 The percentage of conversion of dry reforming using 1.0% Pt/Al_2O_3 performed both conventional tube reactor and palladium membrane tube reactor at 450°C, pressure 0.5 atm, 1.0 atm, and 1.5 atm, respectively (a) methane conversion and (b) carbon dioxide conversion.

4.4.3.3 The effect of sweep gas in the palladium membrane tube reactor

The difference in the hydrogen partial pressure between the reaction and permeation side is the driving force for hydrogen permeation. The rate of hydrogen permeation should be enhanced by the sweep gas flow rate. In this study only palladium membrane tube reactor was employed by using 1.0 g of 1.0% Pt/Al_2O_3 (500 μm) with 30 mL/min flow rate of gas mixture of CH_4:CO_2 (1:1).

In addition, the flow rate of argon gas used as a sweep gas on the tube side of palladium membrane tube reactor was varied Figure 4.21 presents the conversion as a function of sweep gas flow rate.

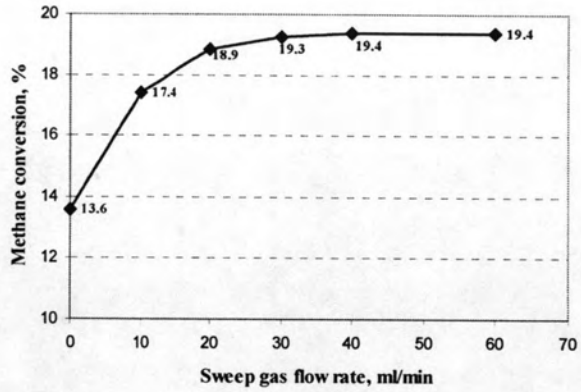

(a)

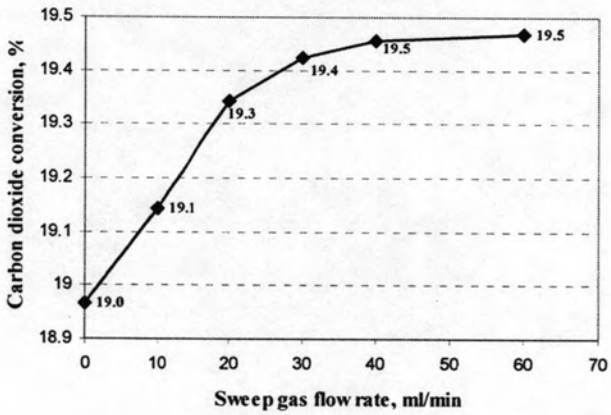

(b)

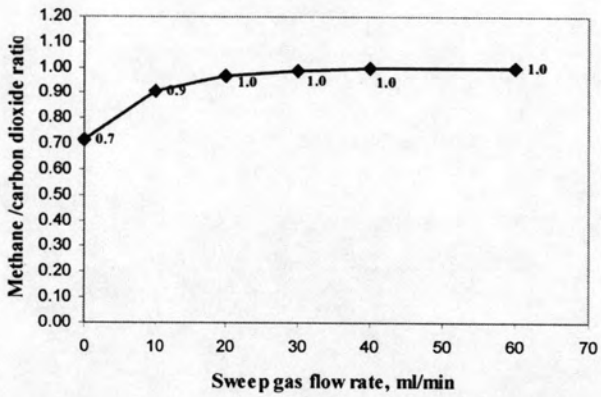

(c)

Figure 4.24 Effect of the sweep gas flow rate on the reactor performance (a) methane conversion, (b) carbon dioxide conversion, (c) methane/carbon dioxide ratio.

It was found that when the sweep gas flow rate was no flow, the methane conversion was 13.6% when no sweep gas was used. When the sweep gas flow rate was increased, the methane conversion was higher. However, the methane conversion was quite constant starting from the sweep gas flow rate around 40 mL/min. The carbon dioxide conversion was stable at the sweep gas flow rate about 40 mL/min. Moreover, the ratio of methane /carbon dioxide was perfectly close to 1 when the sweep gas was also applied. It was found that the methane and carbon dioxide conversion using palladium membrane tube reactor were improved by using the sweep gas. The results agreed with Ferreira-Aparicio *et al.*[57] and Munera *et al.*[58] that an increase in the flow rate of sweep gas reduced the partial pressure of hydrogen at the permeate side, resulting in an increase in the rate of hydrogen permeation through the membrane from the reaction side [33]. The chemical equilibrium of the reforming reaction was considerably shifted to the product side. This is reflected in an improvement of the methane conversion.

It can be concluded clearly that the optimum sweep gas flow rate in tube side of palladium membrane tube reactor was 40 mL/min that the reaction was operated with feed flow rate of gas mixture CH_4:CO_2 (1:1) around 30 mL/min at 450°C, pressure 1 atm.

In summary, to improve the performance of reaction, the palladium membrane tube reactor was introduced. The optimum condition of dry reforming in this study was as follows: 1.0 g of 1.0%Pt/Al_2O_3 (500μm) with 30 mL/min of the gas mixture of CH_4:CO_2 (1:1) as a feed at 450 °C, pressure 1 atm. Moreover, argon gas was used as a sweep gas with at least 40 mL/min in order to obtain the maximum conversion and yield.

Part II: Palladium Membrane Reactor Tube Containing the Intermetallic Diffusion Barrier

4.5 The effect of intermetallic diffusion on the performance of palladium membrane reactor

In part I, it was shown that using palladium membrane tube reactor in dry reforming gave higher methane conversion than using the conventional tube reactor at the same conditions. However, all the reactions were carried out at 450°C, the highest temperature which was reported by other research groups [55-58], in order to avoid the intermetallic diffusion from porous stainless steel to palladium layer.

This study was designed for the investigation of such intermetallic diffusion. Another dense palladium membrane tube with 18 μm palladium thickness was thus prepared in the same manner as the previous two tubes. The hydrogen permeation flux of this tube was measured according to section 3.2.2.3 Figure 4.25 shows the hydrogen permeation flux as a function of the exposure temperature.

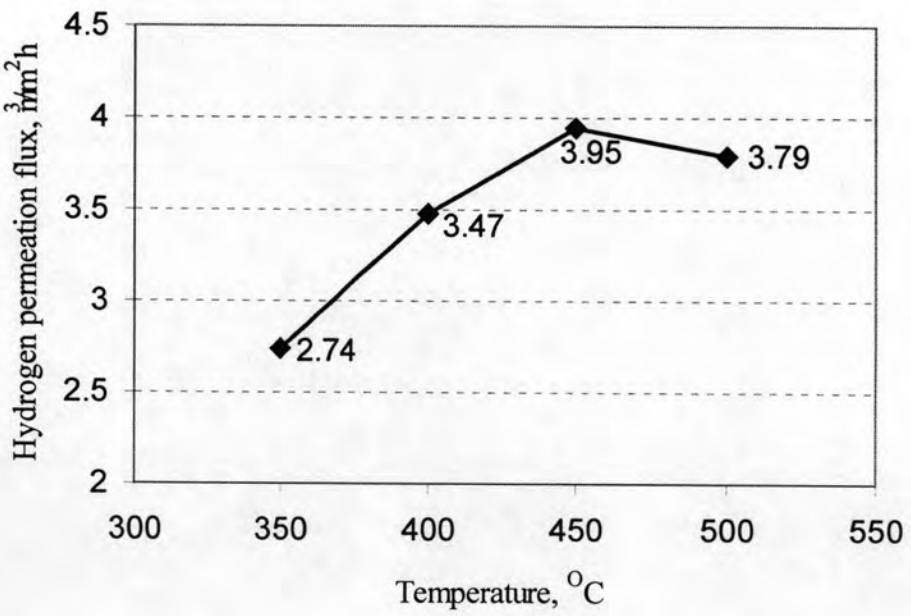

Figure 4.25 The relationship between hydrogen permeation flux after 24 hours of exposure and the exposure temperature.

It was found that the hydrogen permeation flux was higher when the exposure temperature was elevated. However, when the temperature was 500°C, the hydrogen permeation flux was decreased. One reasonable explanation for these results was that the intermetallic diffusion had occurred which could inhibit hydrogen permeation. Similar observation was reported by Edlund and McCarthy [64]. In addition, Marlidovish *et al.* [27] stated that when the operation temperature was higher than 450°C, hydrogen permeation flux would decline due to the intermetallic diffusion.

In order to prove the intermetallic diffusion, the palladium membrane tube, after exposure at 500°C, was cut into a small thin ring. By using Scanning Electron Microscope equipped with Energy Dispersive X-ray Spectrometer (SEM-EDS) in the mode of mapping, the distribution of each metal, *i.e.*, iron, chromium, and nickel in palladium layer could be observed. Figure 4.26 shows the SEM micrographs of the cross-section palladium membrane tube. With EDS mapping scan for the individual metal, it can obviously be seen that iron, chromium, and nickel, the main components of stainless steel, had diffused into palladium layer.

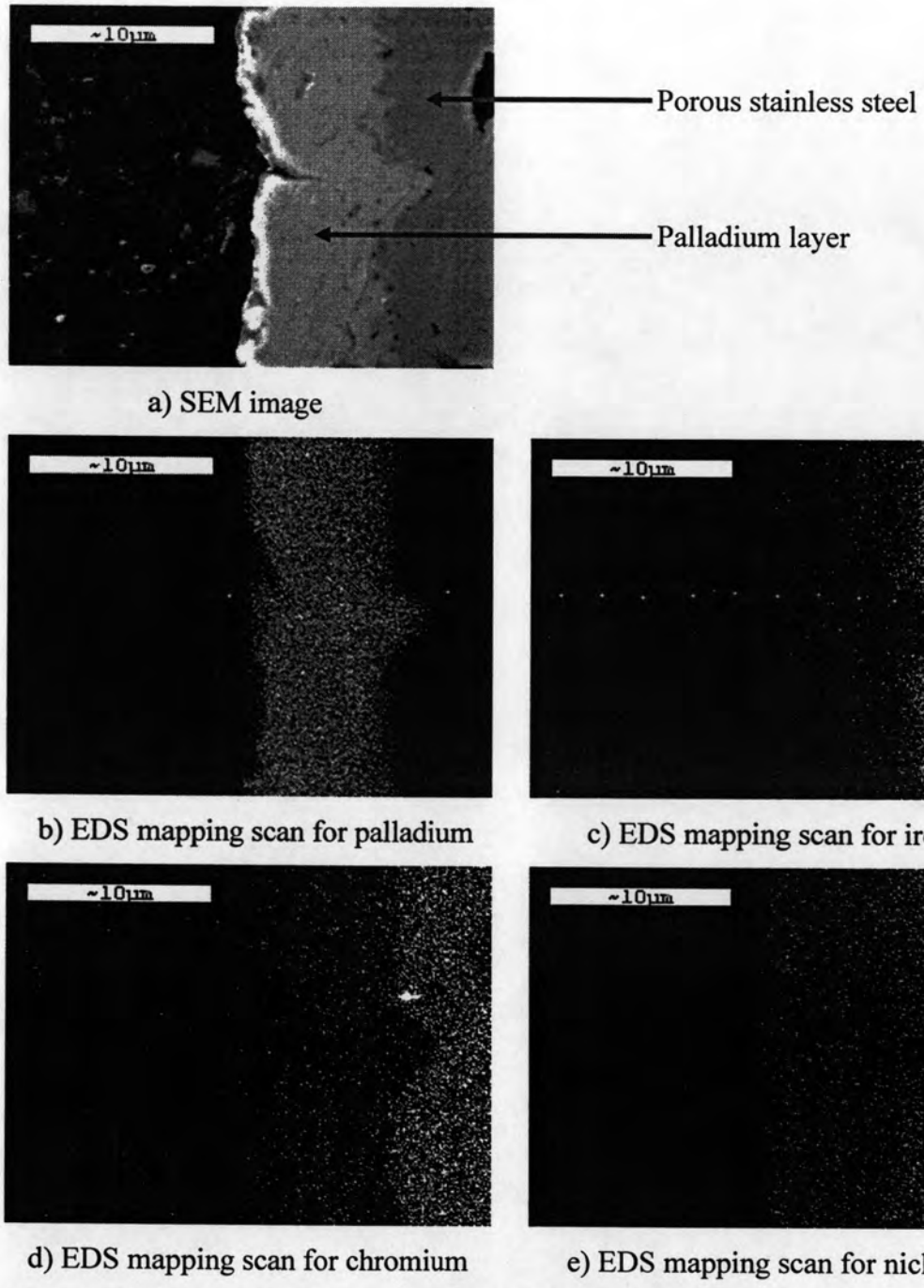

a) SEM image

b) EDS mapping scan for palladium

c) EDS mapping scan for iron

d) EDS mapping scan for chromium

e) EDS mapping scan for nickel

Figure 4.26 SEM micrographs (2500x) with EDS mapping scan of the cross-section palladium membrane tube after hydrogen exposure at 500°C for 24 hours.

Therefore, it could be concluded that hydrogen permeation flux decrease was due to the metal diffusion from the porous stainless steel to the palladium layer.

4.6 Formation of intermetallic diffusion barrier on porous stainless steel disk

In order to prevent the intermetallic diffusion, a barrier must be created as an interlayer between the palladium layer and the porous stainless steel. Figure 4.27 illustrated that the location of the barrier can inhibit the direct contact between those two materials.

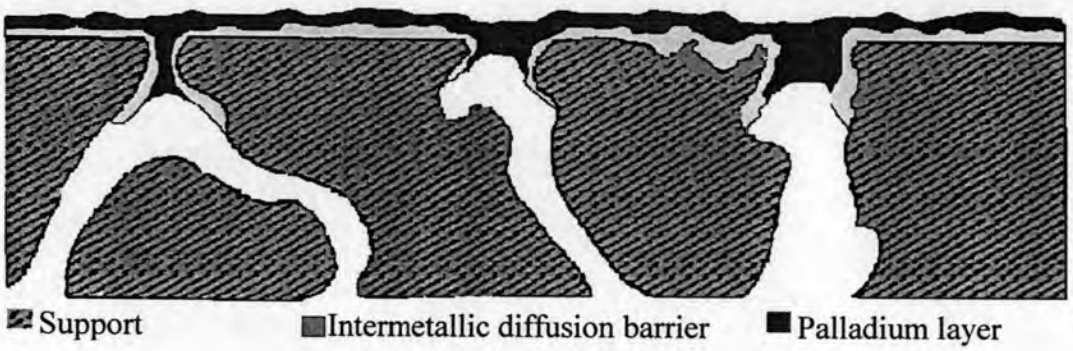

Figure 4.27 The intermetallic diffusion barrier located between the palladium layer and porous stainless steel.

The barrier material should be chemically stable under operating conditions (at least 500°C) with respect to reduction of the oxide by either hydrogen or the base metal. Several materials such as silver-tungsten, silica, chromium, chromium oxide and oxidized stainless steel were chosen for this study.

4.6.1 Silver-tungsten layer by electroless plating technique

Since tungsten is the highest melting metal and its Tamman temperature is higher than the working temperature of the palladium membrane tube (see Appendix C), it can be one of the good candidates for an intermetallic diffusion barrier. Unfortunately, there is no report for pure tungsten plating, neither electroplating nor electroless plating. The tungsten alloys like Co-W [71], Ni-W-P [72], Ni-W [73] and Ag-W [74] were considered instead. Due to Tamman temperatures of Ni, Co, P, and Ag which were close to the working temperature at 500°C, they could diffuse into the palladium layer. However, the palladium–silver alloy could resist the hydrogen-embrittlement [12]. Therefore, Ag-W might be a good choice.

The Ag-W plating condition was followed the method of Bogush *et al.* using electroless plating technique [59]. The silver-tungsten layer was generated from aqueous solution of the silver-benzoate complex. Benzoic acid was used as the complexing agent to stabilize the solution at room temperature and under light [61]. Using the hydrazine hydrate as the reducing agent allowed the formation of thin uniform layer by heterogeneous nucleation at the catalytic surface without homogeneous silver nucleation in the solution. The concentration of the basic component such as silver ion, benzoic complexing agent, and reducing agent was optimized to reach the best condition for plating observed by having no precipitation of silver particles After 60 min, the surface of the porous stainless steel disk was completely covered with silver-tungsten as revealed in Figure 4.28.

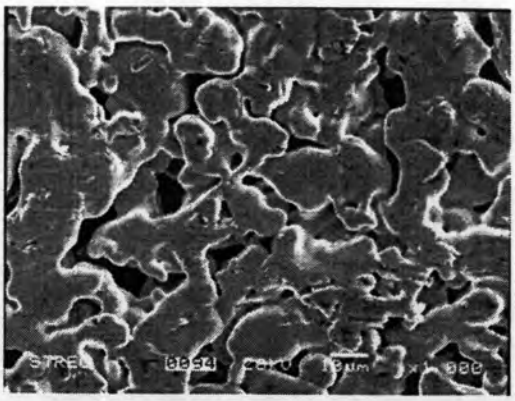

Before plating (1000x)

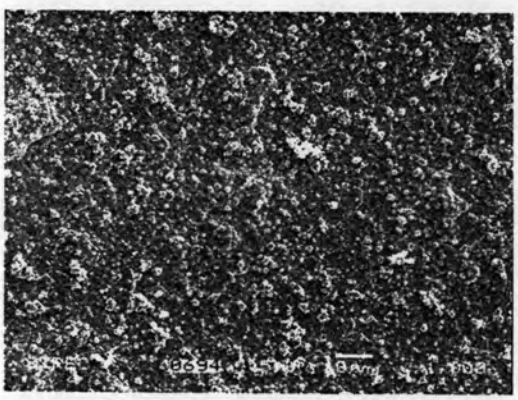

After plating (1000x)

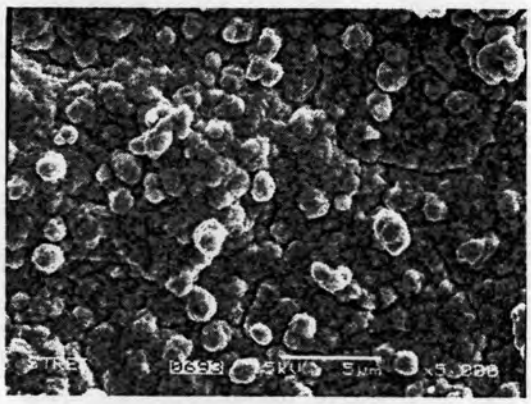

After plating (5000x)

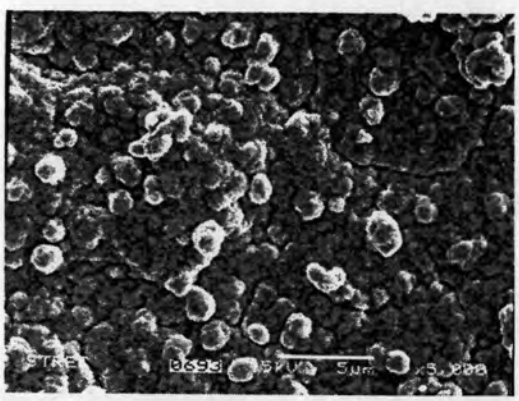

After plating (10000x)

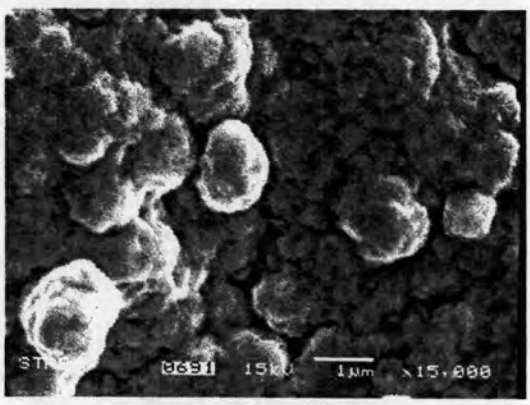

After plating (15000x)

Figure 4.28 SEM micrographs of porous stainless steel disk before and after silver-tungsten plating for 60 min.

Moreover, the presence of tungsten and silver on the surface layer was confirmed by EDS spectrum as shown in Figure 4.29.

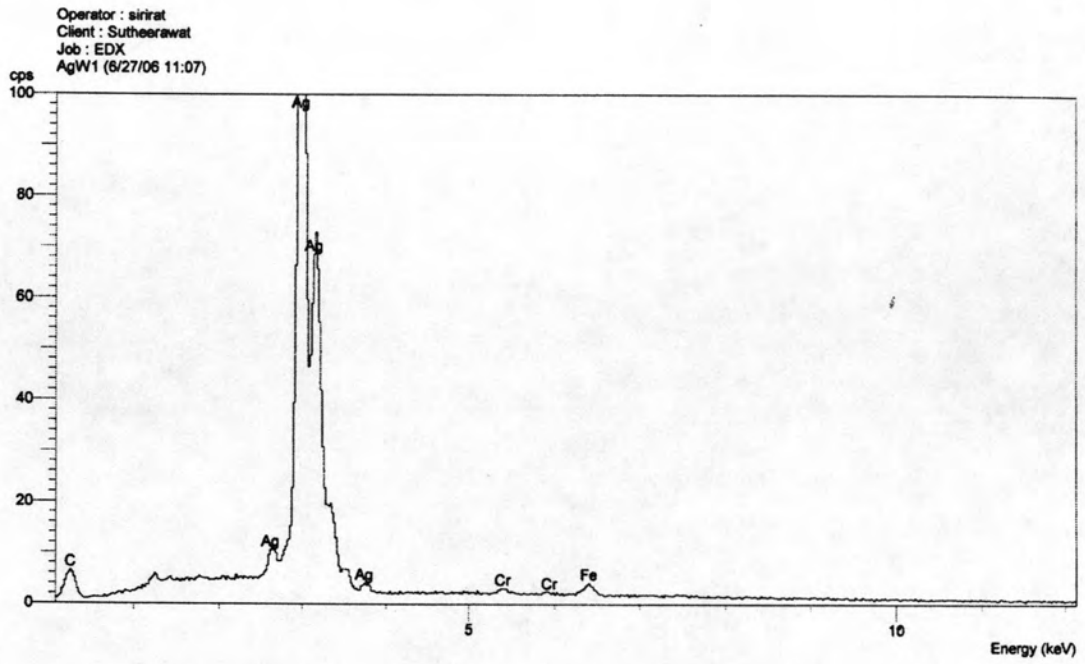

Figure 4.29 EDS spectrum of silver-tungsten deposited on porous stainless steel disk.

The quantitative analysis by EDS spot scan indicated that the silver-tungsten deposited on porous stainless steel was composed of tungsten weight 0.72% and silver wt 94.31%. This result was similar to Glickman *et al.*'s work [66]. Anyway it was subjected to palladium plating, which from now on was referred as Pd/Ag-W/PSS. It was then exposed in helium at 500°C for 24 hours.

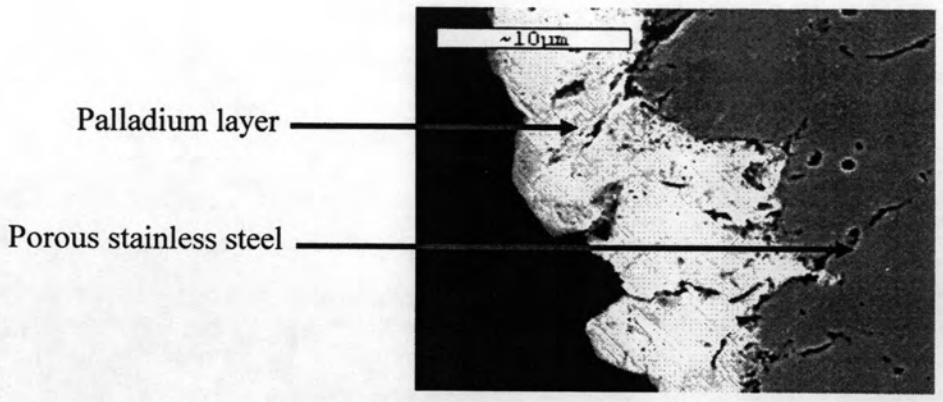

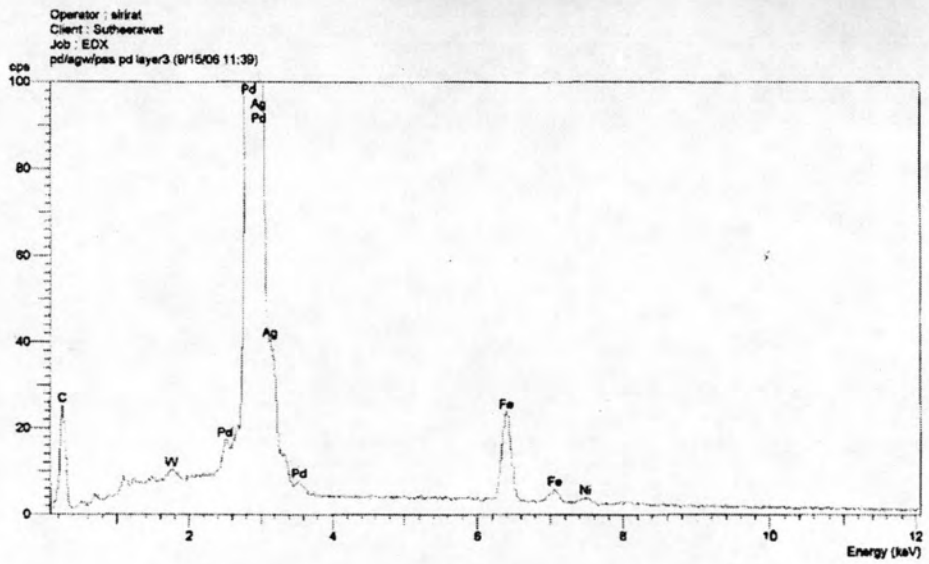

a) EDS spectrum of palladium layer

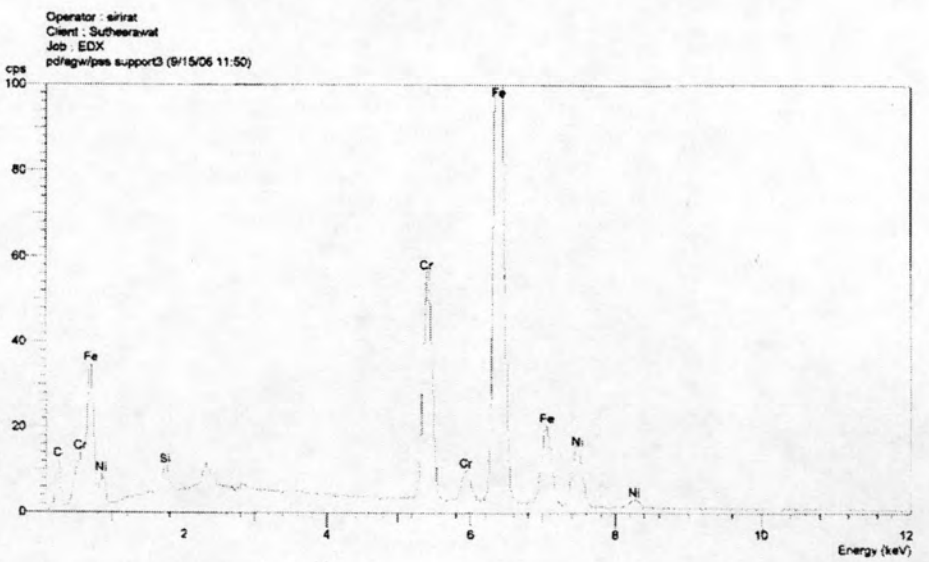

b) EDS spectrum of porous stainless steel

Figure 4.30 SEM micrograph (2500x) with EDS spectrum of the cross-section Pd/Ag-W/PSS disk exposed in helium at 500°C for 24 hours.

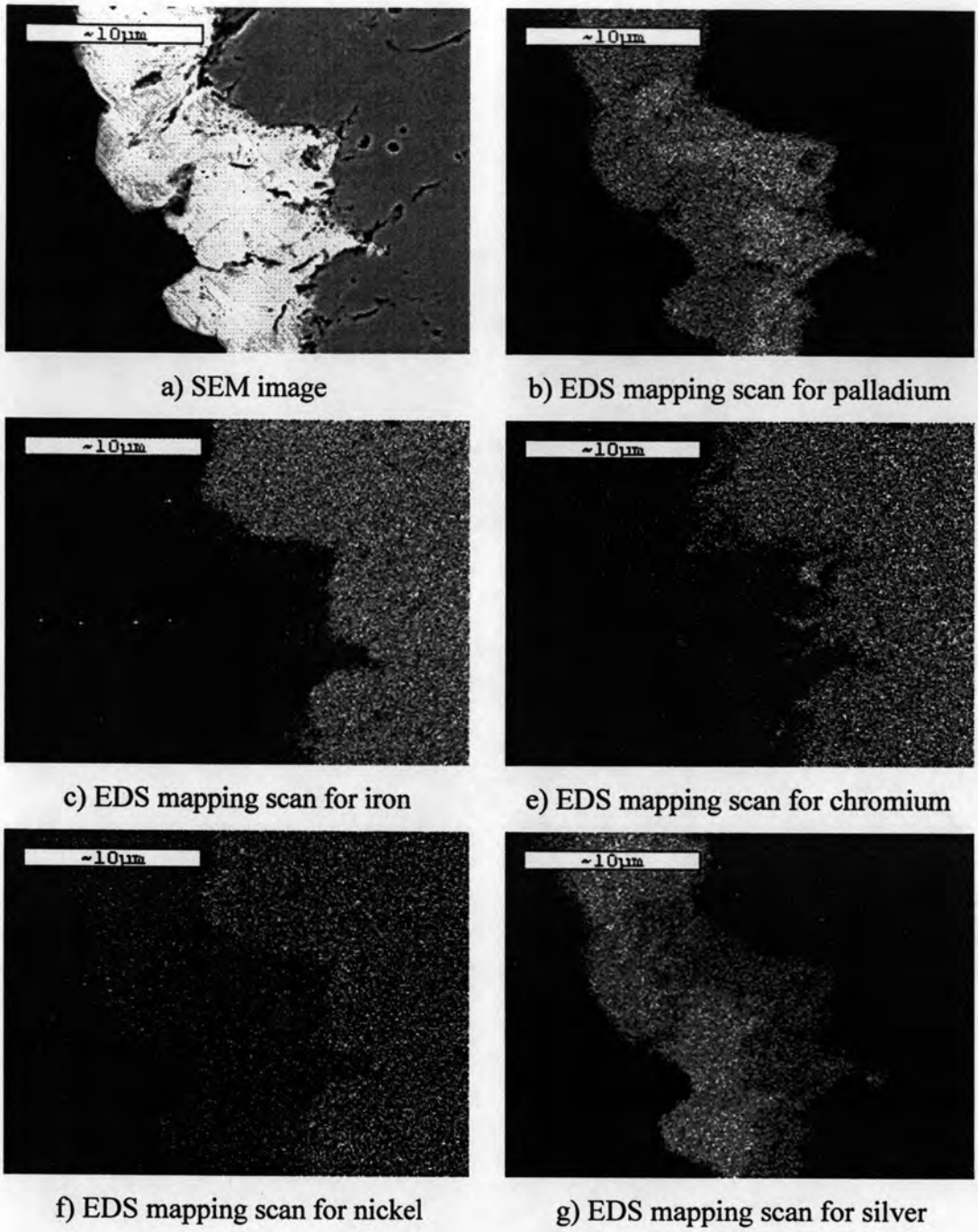

a) SEM image

b) EDS mapping scan for palladium

c) EDS mapping scan for iron

e) EDS mapping scan for chromium

f) EDS mapping scan for nickel

g) EDS mapping scan for silver

Figure 4.31 SEM micrographs (2500x) with EDS mapping scan of the cross-section Pd/Ag-W/PSS disk exposed in helium at 500°C for 24 hours.

Figure 4.31 showed that Fe, Cr, and Ni from porous stainless steel could diffuse into the palladium layer. In addition, the silver-tungsten layer could not be observed, probably due to their diffusion into the palladium layer. Indeed, the analysis EDS spot scan clearly revealed the presence of both silver and tungsten in palladium

layer as shown in Table 4.5. Furthermore, the component of porous stainless steel were detected in palladium layer as well.

Table 4.5 The metal distribution in palladium layer and porous stainless steel of Pd/Ag-W/PSS

		Pd layer (%)						Porous stainless steel (%)					
		Pd	Fe	Cr	Ni	Ag	W	Pd	Fe	Cr	Ni	Ag	W
Pd/Ag-W/PSS	1	78.52	13.37	0.41	0.52	6.42	0.76	0.42	71.78	16.61	11.13	0.06	-
	2	80.11	14.36	0.37	0.51	5.72	0.65	0.43	71.16	17.31	11.15	0.06	-
	3	76.82	15.83	0.34	0.57	5.69	0.75	0.46	71.13	16.98	11.38	0.05	-
	Avg	78.48	14.52	0.37	0.53	5.94	0.72	0.44	71.36	16.97	11.22	0.06	-
	SD	1.65	1.24	0.04	0.03	0.41	0.06	0.02	0.37	0.35	0.14	0.01	-
	RSD	2.10	8.52	9.41	6.03	6.95	8.45	4.77	0.51	2.06	1.24	10.19	-

Avg = Average
SD = Standard deviation
RSD = Relative standard deviation

Accordingly, silver-tungsten could not be used as the intermetallic diffusion barrier.

4.6.2 Silica layer by sol-gel technique

Silica had been reported to be an intermetallic diffusion barrier [75, 62]. The preparation of silica layer on porous stainless steel was followed Lee Dong-Wook et al. by using the sol-gel method [62]. The reaction was exhibited in Figure 4.32.

$$\equiv Si-\underset{(TEOS)}{OC_2H_5} + H_2O \underset{\text{Esterification}}{\overset{\text{Hydrolysis}}{\rightleftharpoons}} \equiv Si-OH + ROH$$

$$\equiv Si-OH + C_2H_5O-Si\equiv \underset{\text{Alcoholysis}}{\overset{\text{Alcohol condensation}}{\rightleftharpoons}} \equiv Si-O-Si\equiv + C_2H_5OH$$

$$\equiv Si-OH + HO-Si\equiv \underset{\text{Hydrolysis}}{\overset{\text{Water condensation}}{\rightleftharpoons}} \equiv Si-O-Si\equiv + H_2O$$

Figure 4.32 Reactions of TEOS in alcohol as a co-solvent to produce silica layer.

Solubility of silica particles in alcohol solution is proportional to surface curvature of particles. If particle size of silica is more than about 0.1μm, reverse reaction of alcoholysis is not important. But small silica particle are dissolved and provided as a monomer in solution, due to reverse reaction of hydrolysis. As the monomers react with large silica particles, number of silica particles in solution decrease and remaining particle size increases. This phenomenon is called Ostwald ripening [76]. Particles grow continuously until solubility of particles decrease enough, and stable silica sol with average particle size above 0.1μm is produced. Figure 4.33 reveals the sphere-shaped silica particles deposited on porous stainless steel disk.

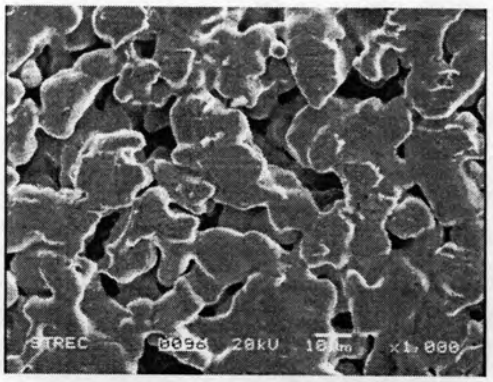

Before plating (1000x)

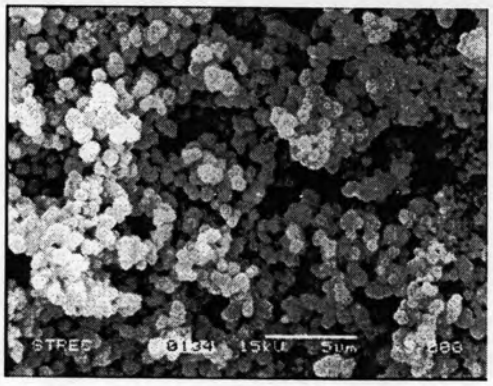

After plating (5000x)

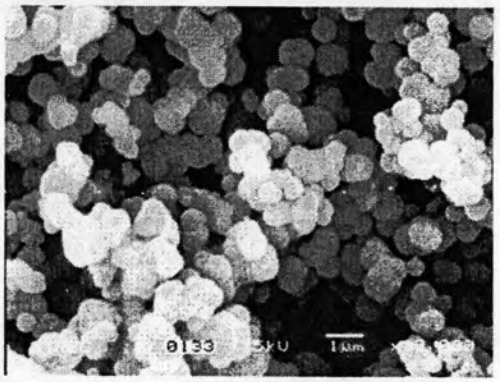

After plating (10000x)

Figure 4.33 SEM micrographs of porous stainless steel disk before and after silica plating.

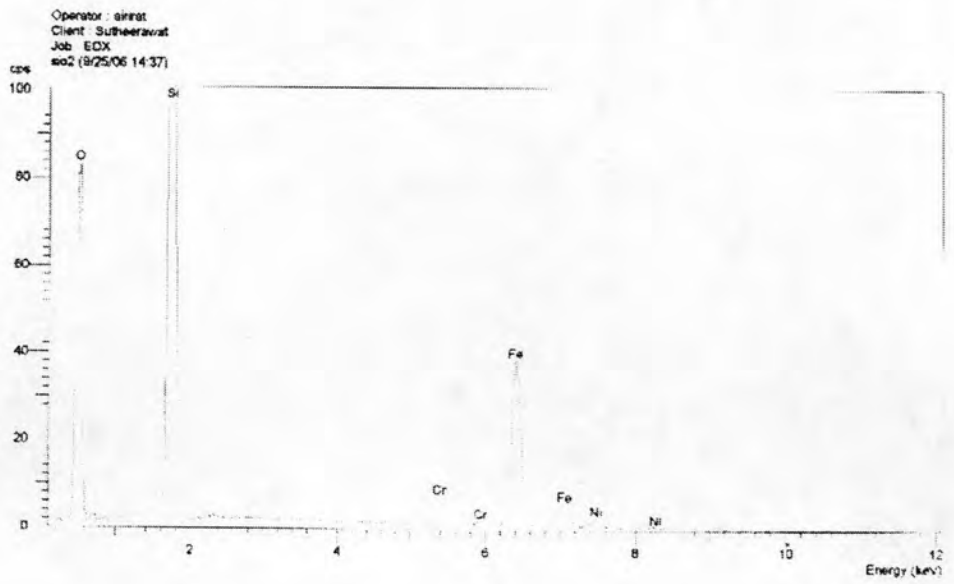

Figure 4.34 EDS spectrum of silica deposited on porous stainless steel.

Its EDS spectrum exhibited the presence of Si and O atoms as shown in Figure 4.34. In addition, the components of porous stainless steel, i.e., Cr, Fe, and Ni were also recorded. It could be concluded that the deposition of silica on porous stainless steel by sol-gel technique was successful. Then it was plated with palladium which from now on was referred as $Pd/SiO_2/PSS$.

The cross-section of $Pd/SiO_2/PSS$ disk was investigated for the metallic diffusion by SEM-EDS mapping scan and EDS spot scan. Their results were exhibited in Figure 4.35, Figure 4.36, and Table 4.6.

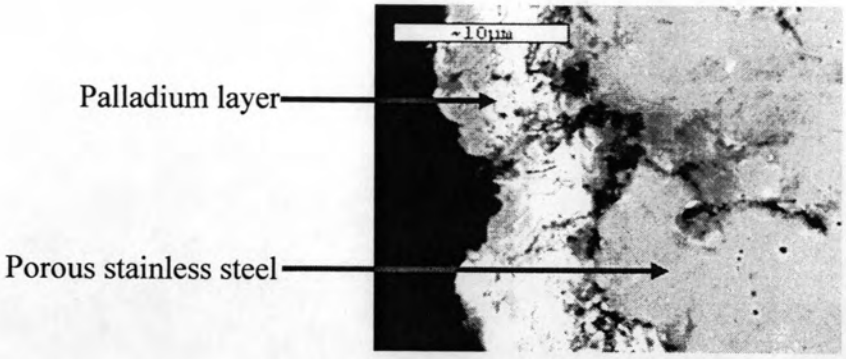

SEM image (2500x)

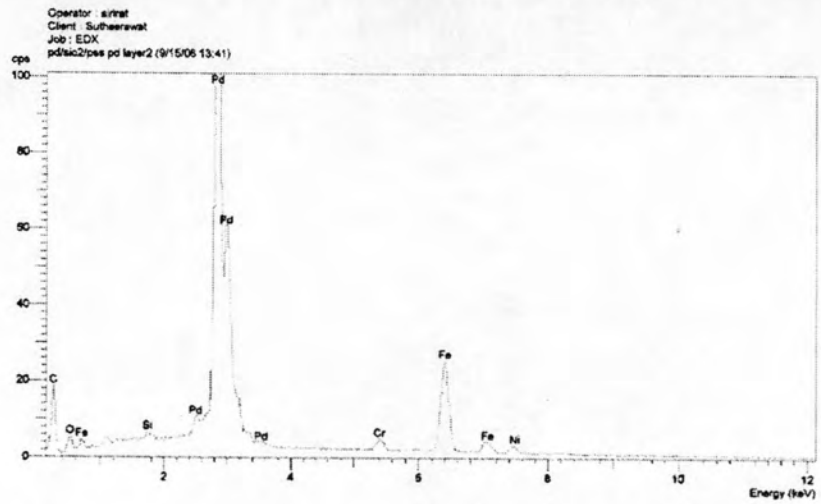

a) EDS spectrum of palladium layer

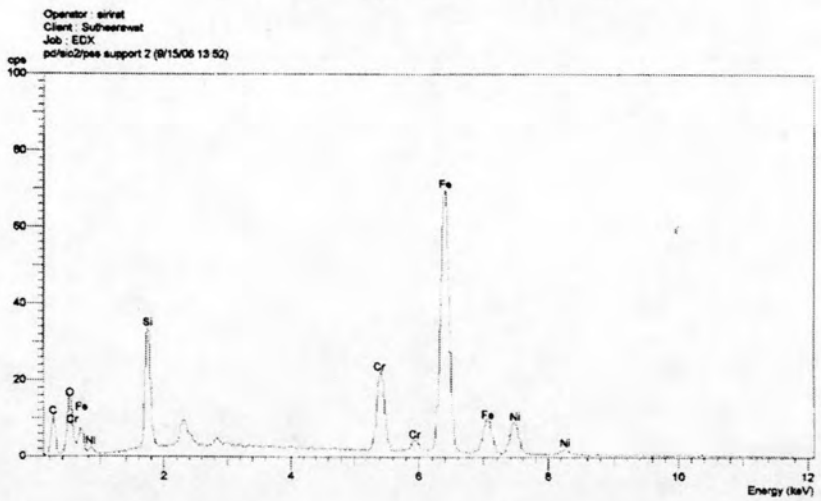

b) EDS spectrum of porous stainless steel section

Figure 4.35 SEM micrograph (2500x) and EDS spectra of the cross-section $Pd/SiO_2/PSS$ disk exposed in helium at 500°C for 24 hours.

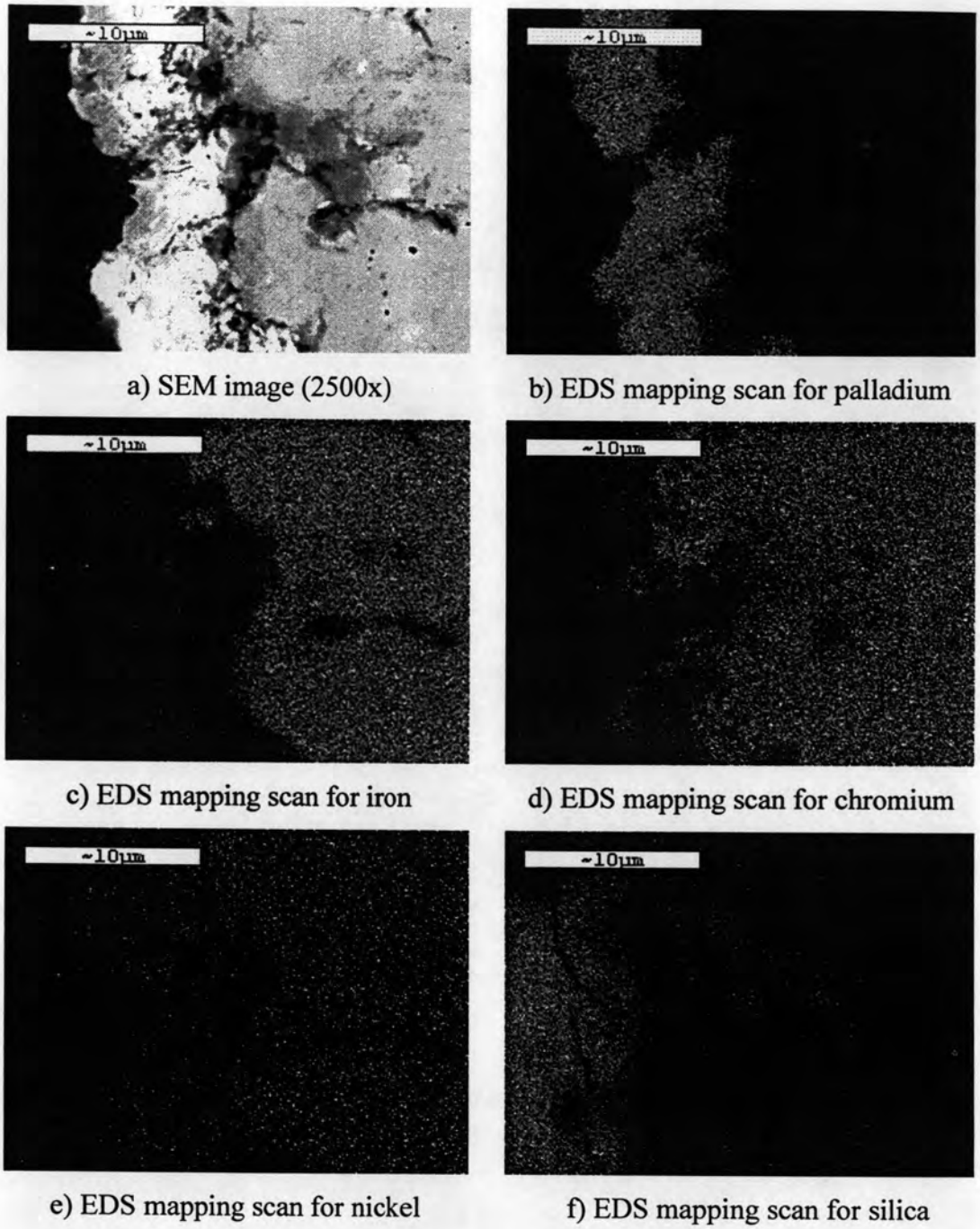

a) SEM image (2500x)

b) EDS mapping scan for palladium

c) EDS mapping scan for iron

d) EDS mapping scan for chromium

e) EDS mapping scan for nickel

f) EDS mapping scan for silica

Figure 4.36 SEM micrographs (2500x) with EDS mapping scan of the cross-section $Pd/SiO_2/PSS$ disk exposed in helium at 500°C for 24 hours.

Table 4.6 The metal distribution in palladium layer and porous stainless steel of $Ps/SiO_2/PSS$

		Pd layer (%)					Porous stainless steel (%)				
		Pd	Fe	Cr	Ni	Si	Pd	Fe	Cr	Ni	Si
$Pd/SiO_2/PSS$	1	79.88	16.57	2.00	1.80	1.05	null	71.08	16.98	10.77	1.06
	2	78.15	17.92	1.78	1.97	0.93	null	70.54	16.14	12.33	1.07
	3	79.48	16.46	2.12	1.90	1.10	null	70.82	16.42	11.65	1.11
	Avg	79.17	16.98	1.97	1.89	1.03	null	70.81	16.51	11.58	1.08
	SD	0.91	0.81	0.17	0.09	0.09	-	0.27	0.43	0.78	0.03
	RSD	1.14	4.79	8.77	4.52	8.51	-	0.38	2.59	6.75	2.45

null = cannot BE detected
Avg = Average
SD = Standard deviation
RSD = Relative standard deviation

The results in Table 4.6 indicated that Fe, Cr, and Ni from stainless steel had diffused into the palladium layer. It meant that silica could not prevent the metallic diffusion. Besides, Figure 4.37 presented the damage surface of silica layer which was very brittle and cracked off easily. Therefore, silica was not a suitable material for an intermetallic diffusion barrier.

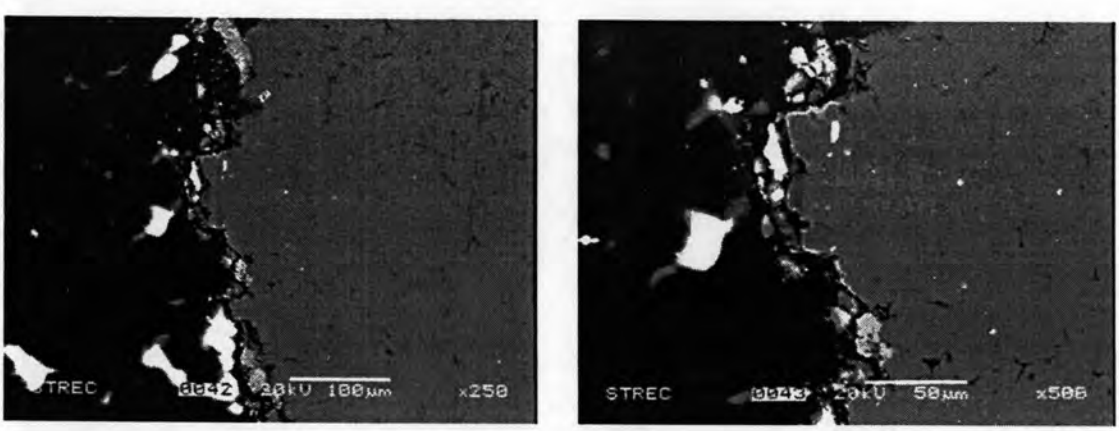

(250x) (500x)

Figure 4.37 SEM micrographs of the cross-section $Pd/SiO_2/PSS$ disk at the damage area.

4.6.3 Oxidation of porous stainless steel surface

Ma *et al.* [77] claimed that a thin metal oxide formed on the surface of the porous stainless steel by controlled oxidation at high temperature using an oxidizing agent such as air or oxygen could act as the metallic diffusion barrier. Therefore, the oxidation of porous stainless steel disk were performed at 450°C and 800°C in air. Then they were plated with palladium. Figures 4.38, 4.39, and 4.40 show the morphology and EDS spectra of porous stainless steel disks which were unoxidized, oxidized at 450°C, and oxidized at 800°C, respectively. It can be seen that the oxidized disk Figure 4.40, had rougher surface than the oxidized disk at 450°C and unoxidized one.

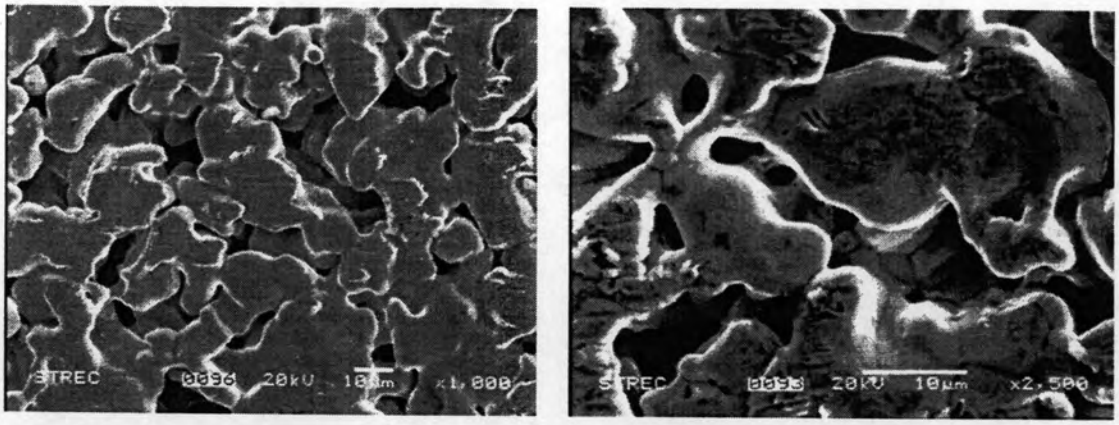

(1000x) (2500x)

(a) SEM images

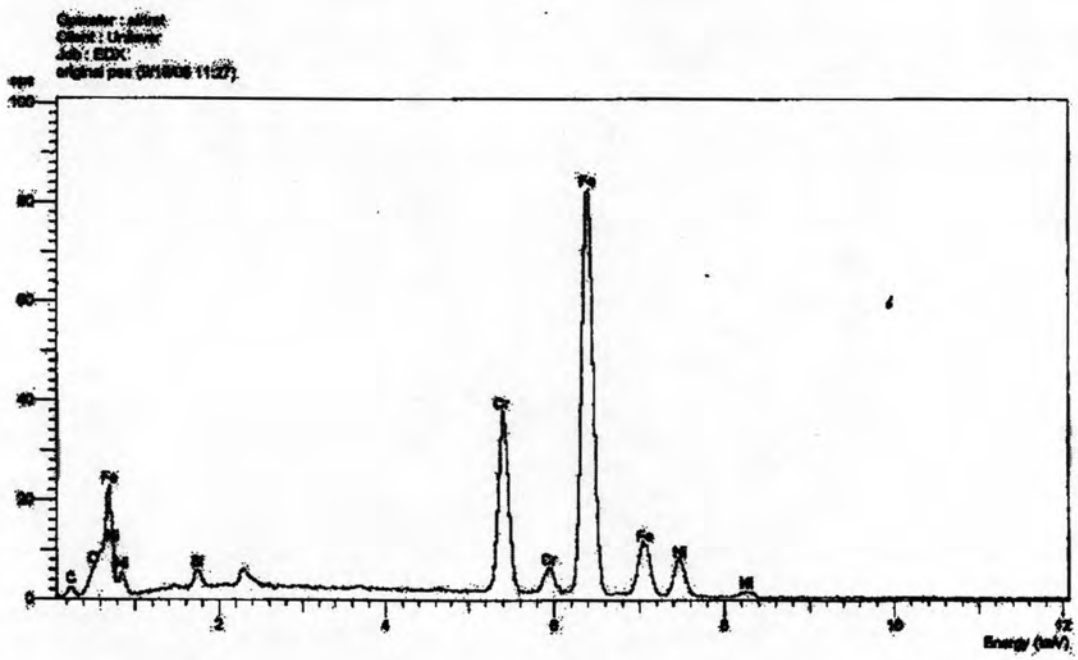

(b) EDS spectrum of un-oxidized stainless steel.

Figure 4.38 SEM micrographs and EDS spectrum of unoxidized porous stainless steel disk.

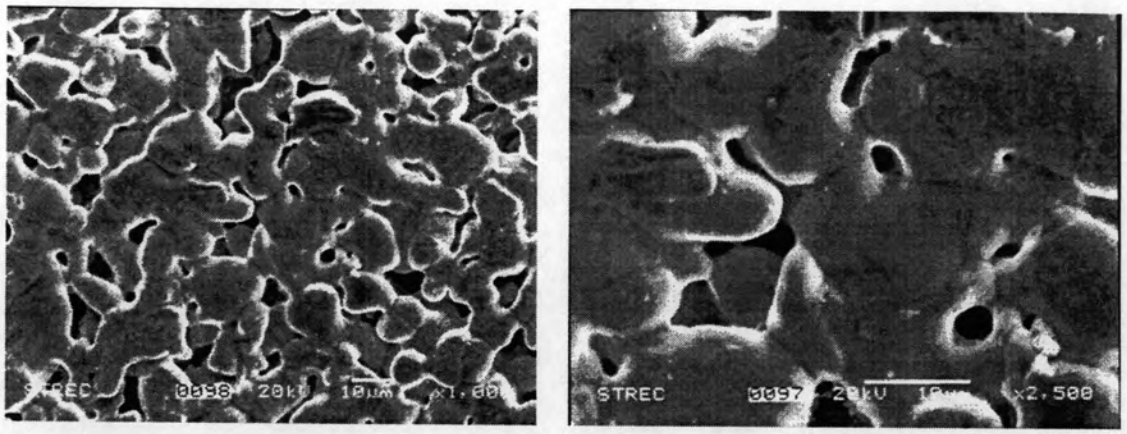

(1000x) (2500x)

(a) SEM images

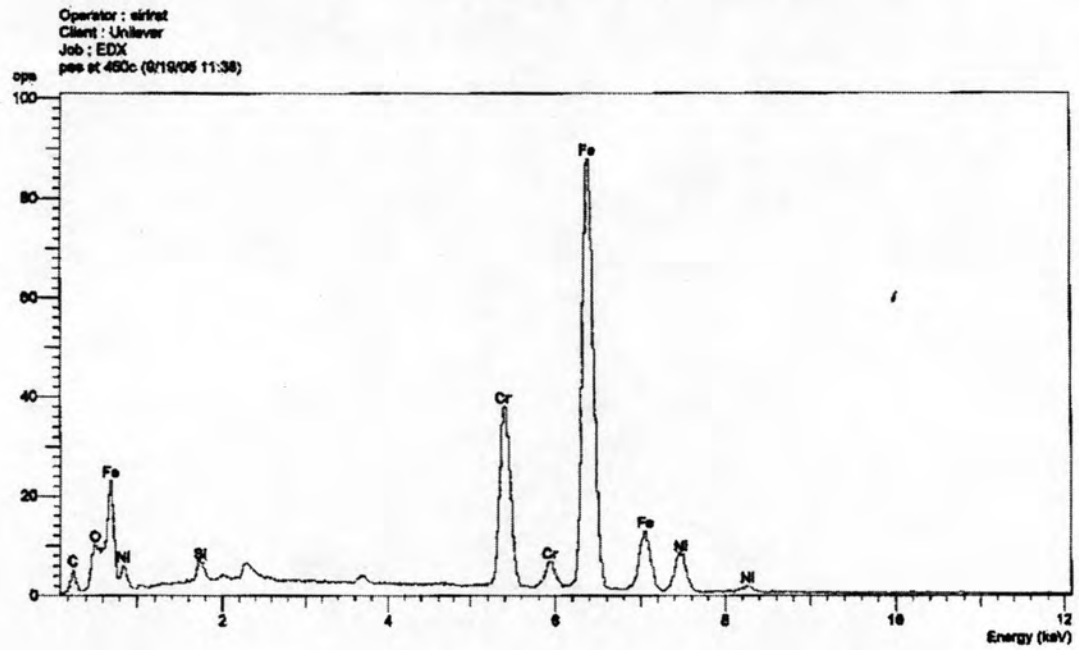

(b) EDS spectrum of oxidized porous stainless steel.

Figure 4.39 SEM micrographs and EDS spectrum of porous stainless steel disk oxidized in air at 450°C for 6 hours.

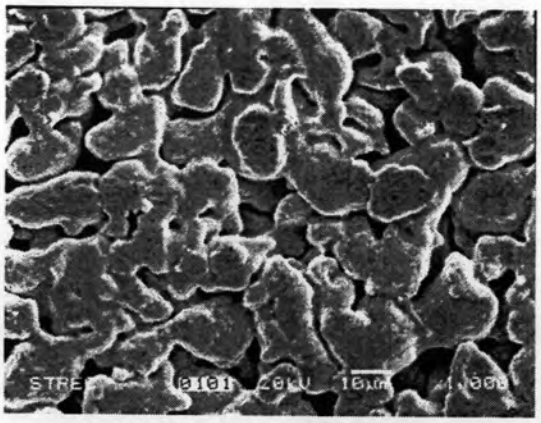

(1000x)

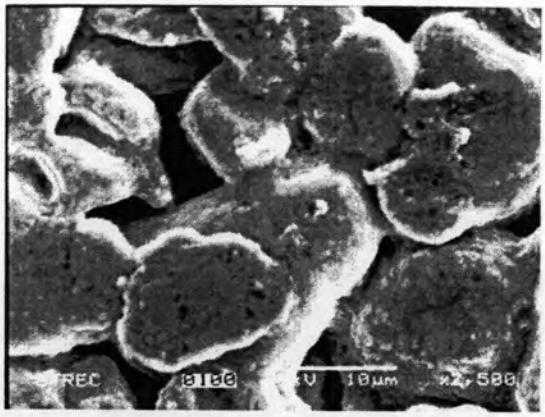

(2500x)

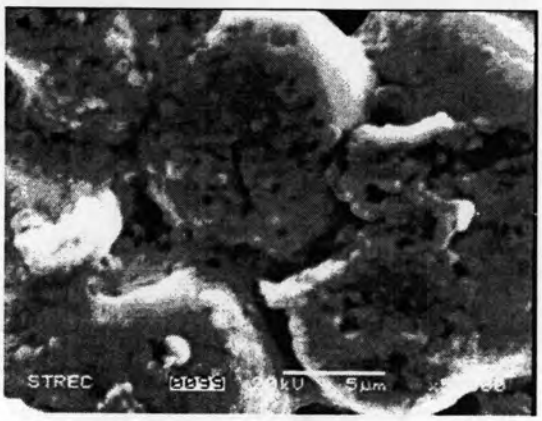

(5000x)

(a) SEM images

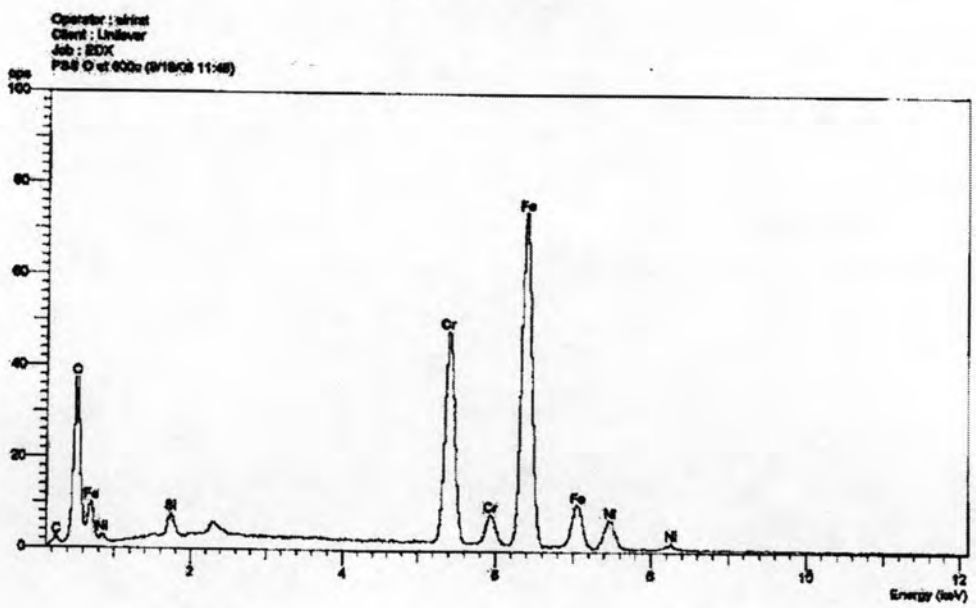

(b) EDS spectrum of oxidized porous stainless steel.

Figure 4.40 SEM micrographs and EDS spectrum of porous stainless steel disk oxidized in air at 800°C for 6 hours.

In addition, the oxidized disk at higher temperature appeared to be darker. EDS spectra also confirmed the surface oxidation by observing the oxygen peak on the left of EDS spectrum. The oxide layer was generated more at higher oxidation temperatures. Since the stainless steel comprises of Cr (16-18 %), Ni (10-14%), others (3.03%) and Fe (balance) [78], iron oxide (Fe_2O_3), Chromium oxide (Cr_2O_3) and nickel oxide (NiO) could be formed. Among the oxides that can be formed, Cr_2O_3 is the most stable oxide due to its low Gibbs free energy, the low diffusion rates of elements in the oxide scale, and it is the most desirable oxide phase for use as an intermetallic diffusion barrier layer.

Then all these three disks were plated with palladium referred as Pd/PSS, Pd/Oxidized PSS at 450°C, and Pd/Oxidized PSS at 800°C, respectively. After annealing at 500°C for 24 hours under helium atmosphere, the EDS mapping scan and the EDS spot scan of their cross-section disks were performed as exhibited in Figures 4.41-4.46. However, the metal oxide interlayer could not be seen in the SEM micrographs. This was perhaps because it was too thin to be observed.

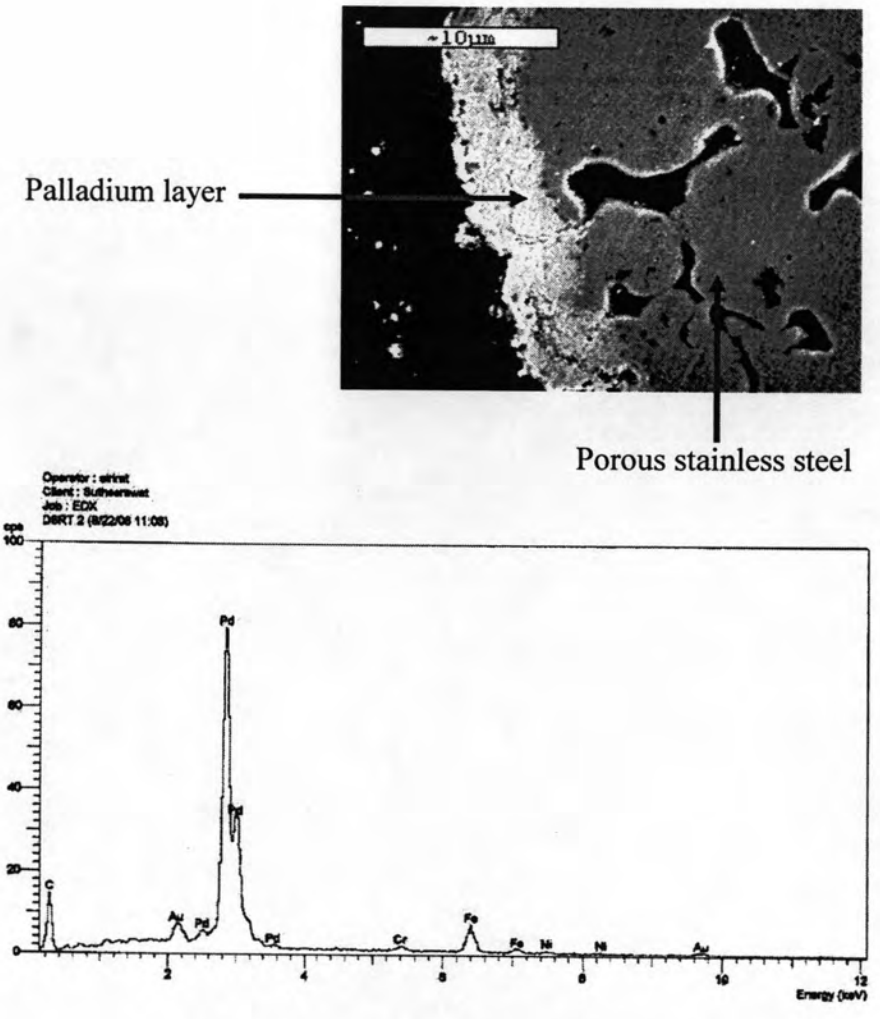

(a) EDS spectrum of palladium layer.

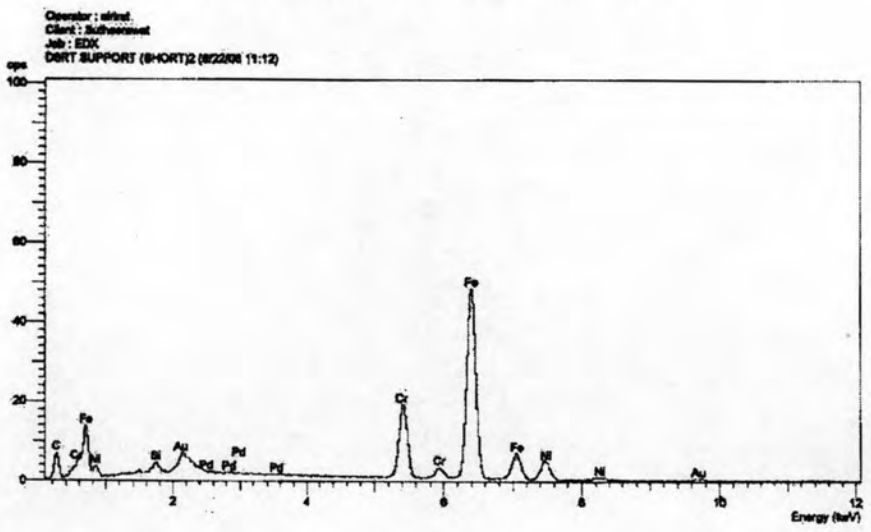

(b) EDS spectrum of porous stainless steel.

Figure 4.41 SEM micrograph (2500x) and EDS spectra of the cross-section Pd/un-oxidized PSS disk exposed in helium at 500°C for 24 hours.

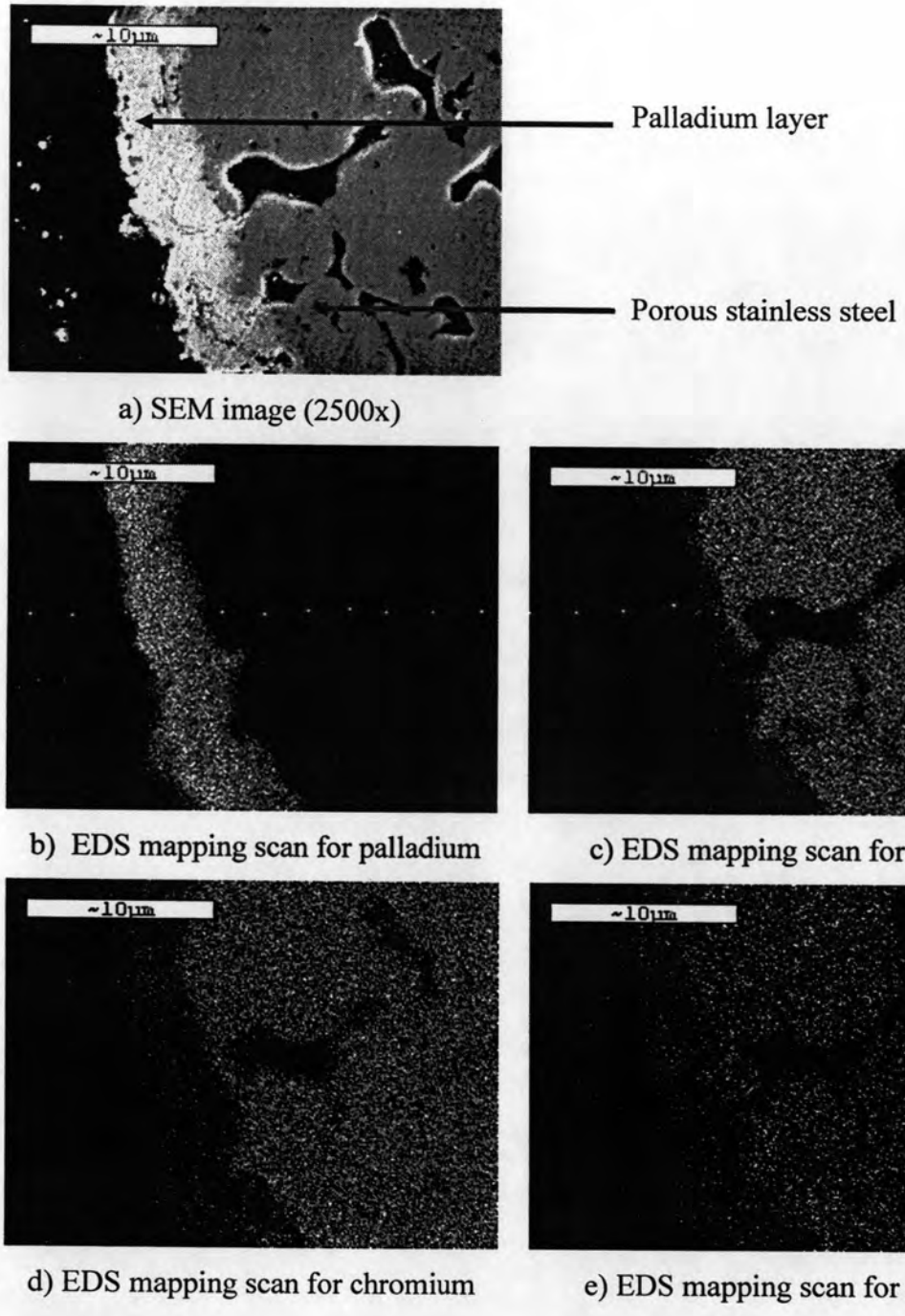

Figure 4.42 SEM micrographs (2500x) with EDS mapping scan of the cross-section Pd/un-oxidized PSS disk exposed in helium at 500°C for 24 hours.

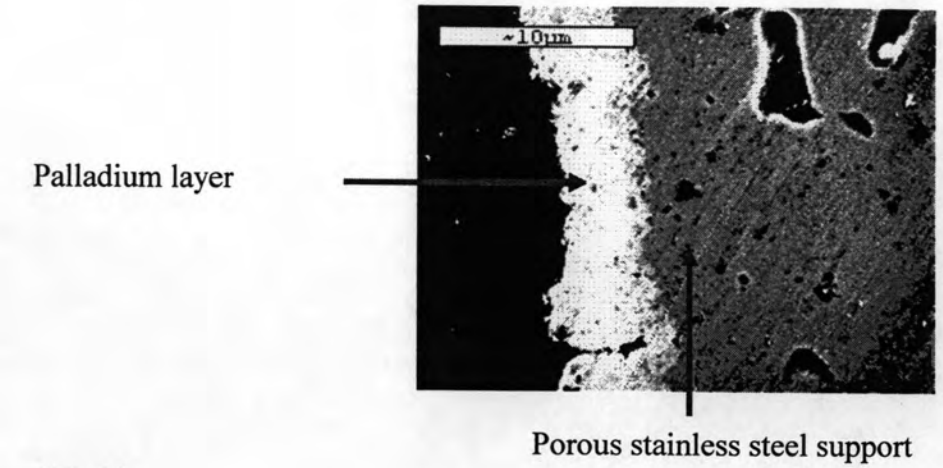

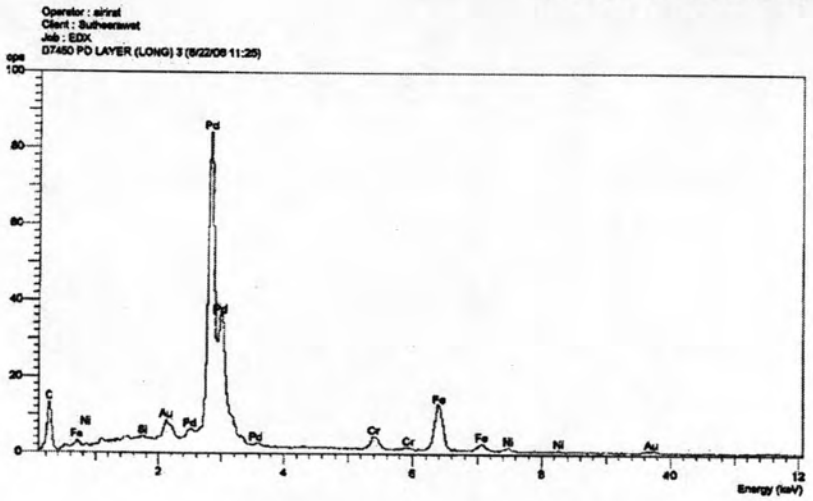

(a) EDS spectrum of palladium layer.

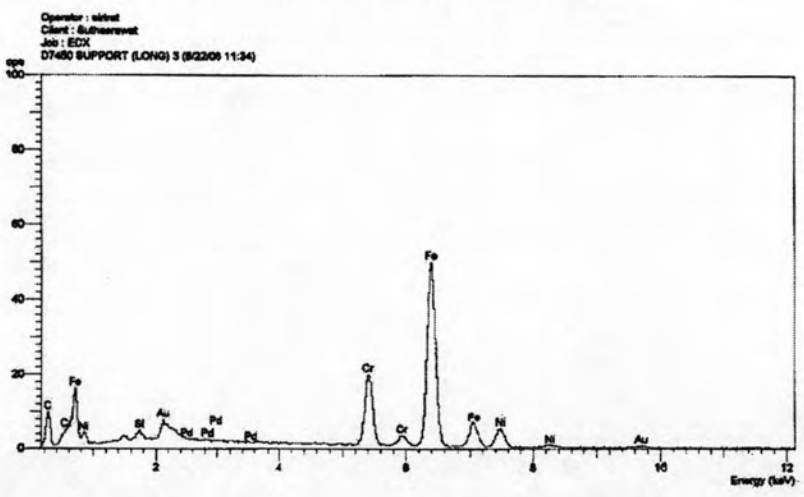

(b) EDS spectrum of porous stainless steel.

Figure 4.43 SEM micrograph (2500x) and EDS spectra of the cross-section of Pd/Oxidized (450°C) PSS disk exposed in helium at 500°C for 24 hours.

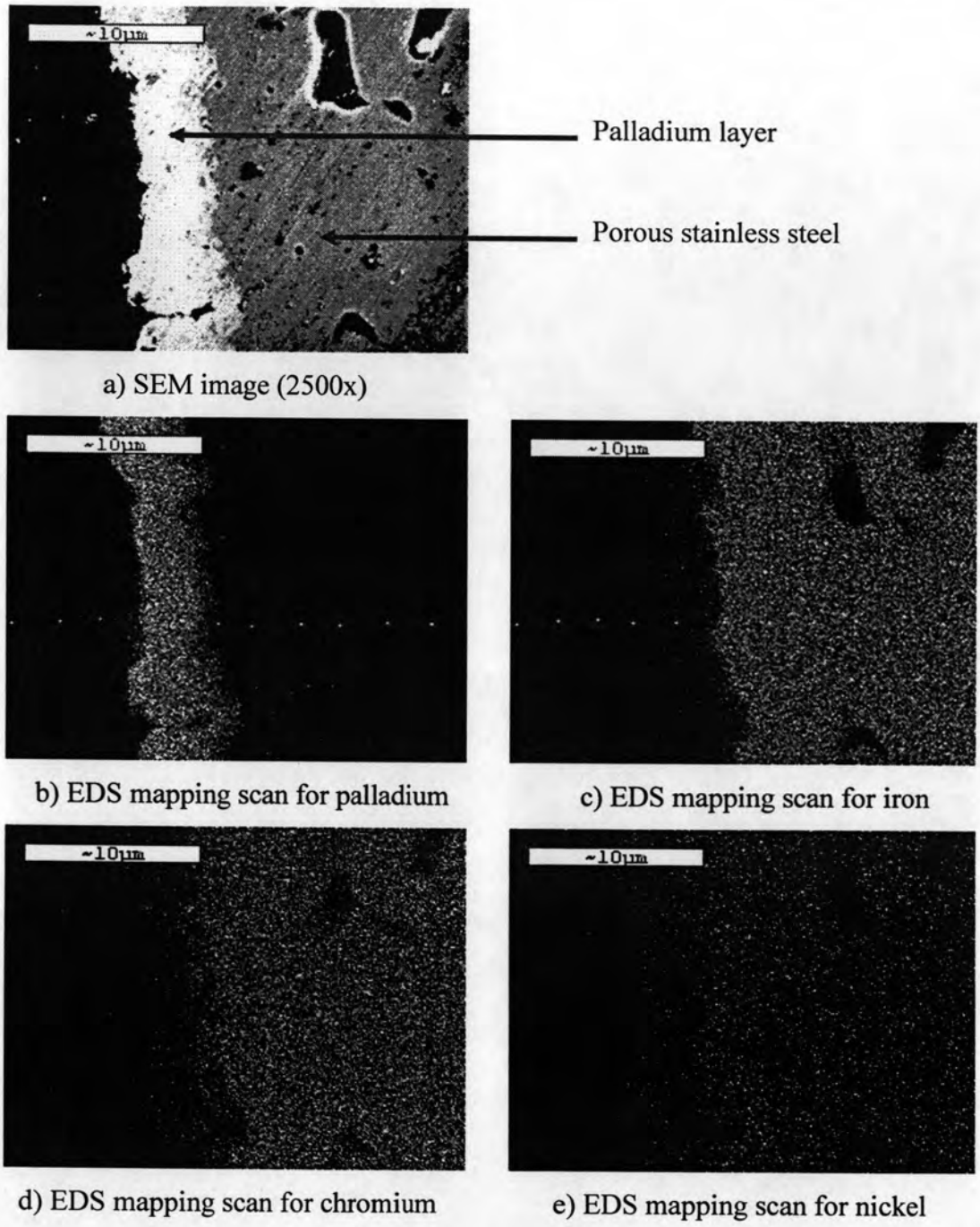

Figure 4.44 SEM micrographs (2500x) with EDS mapping scan of the cross-section Pd/Oxidized (450°C) PSS disk exposed in helium at 500°C for 24 hours.

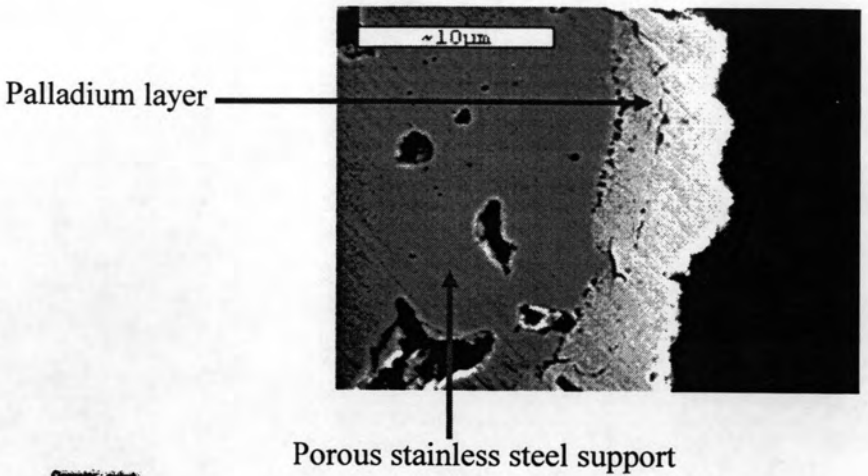

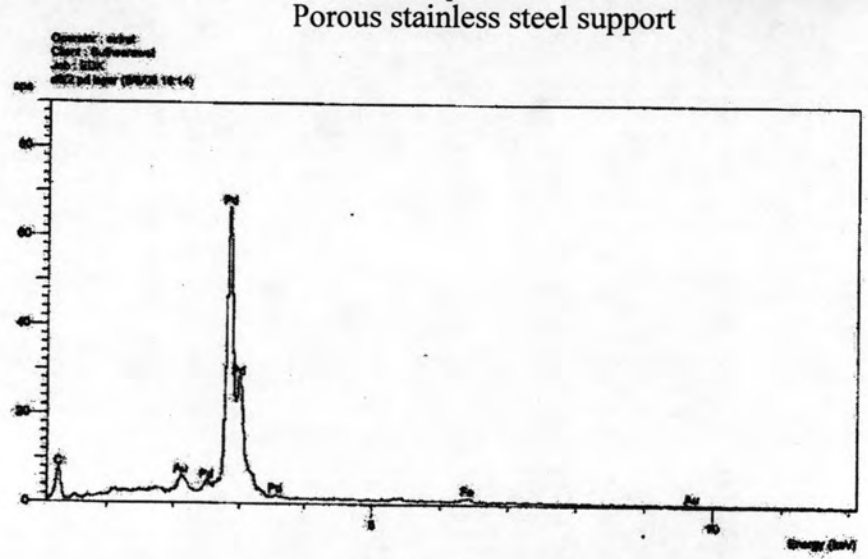

(a) EDS spectrum of palladium layer.

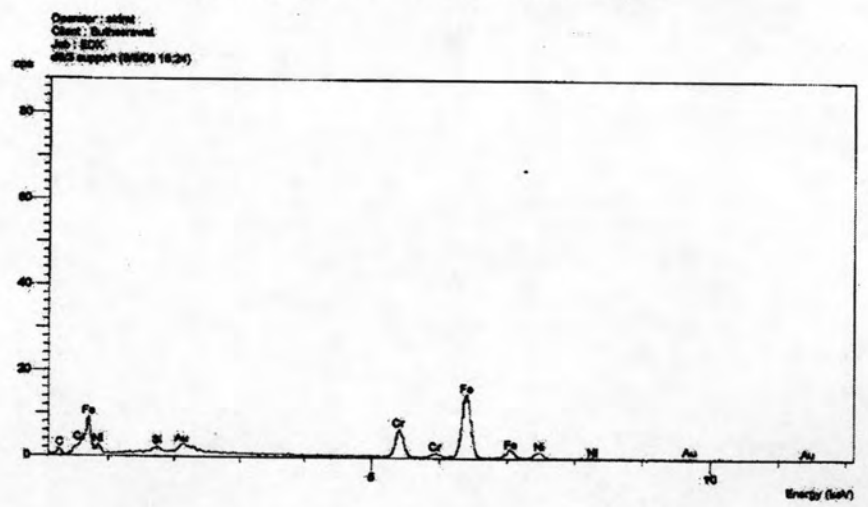

(b) EDS spectrum of porous stainless steel support.

Figure 4.45 SEM micrograph (2500x) and EDS spectra of the cross-section Pd/Oxidized (800°C) PSS disk exposed in helium at 500°C for 24 hours.

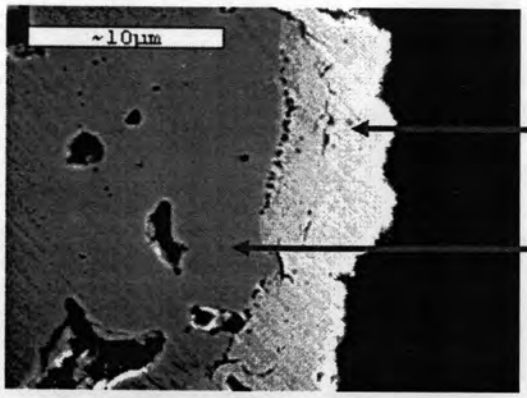

Palladium layer

Porous stainless steel

a) SEM image (2500x)

b) EDS mapping scan for palladium

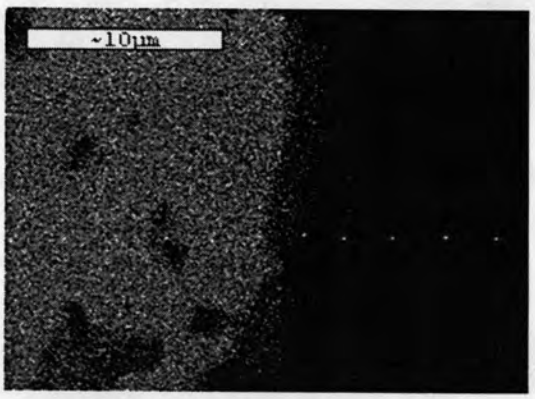

c) EDS mapping scan for iron

d) EDS mapping scan for chromium

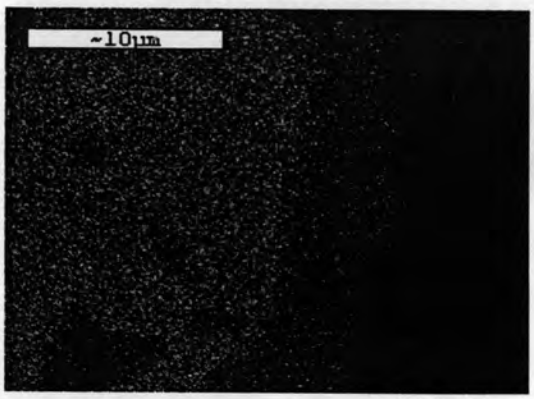

e) EDS mapping scan for nickel

Figure 4.46 SEM micrographs (2500x) with EDS mapping scan of the cross-section Pd/Oxidized (800°C) PSS disk exposed in helium at 500°C for 24 hours.

By EDS mapping scan, it exhibited obviously that the Fe, Cr, and Ni from porous support could diffuse into the palladium layer as shown in Table 4.7.

Table 4.7 The metal distribution in palladium layer and porous stainless steel of Pd/PSS and Pd/Oxidized PSS

		Pd layer (%)				Porous stainless steel (%)			
		Pd	Fe	Cr	Ni	Pd	Fe	Cr	Ni
Pd/PSS	1	83.21	13.02	2.80	0.97	null	71.38	17.1	11.22
	2	81.40	14.35	2.31	1.09	null	71.73	16.94	11.12
	3	81.45	14.97	2.67	0.91	null	71.69	17.15	11.17
	Avg	82.02	14.11	2.59	0.99	null	71.60	17.06	11.17
	SD	1.03	1.00	0.25	0.09	-	0.19	0.11	0.05
	RSD	1.26	7.06	9.79	9.26	-	0.27	0.64	0.45
Pd/Oxidized PSS at 450°C	1	75.21	19.28	2.61	2.9	null	70.92	17.76	11.04
	2	71.44	22.73	2.9	2.93	null	70.23	17.65	11.66
	3	74.29	21.21	2.39	2.54	null	70.83	17.34	11.46
	Avg	73.65	21.07	2.63	2.79	null	70.66	17.58	11.39
	SD	1.97	1.73	0.26	0.22	-	0.38	0.22	0.32
	RSD	2.67	8.20	9.71	7.78	-	0.53	1.24	2.78
Pd/Oxidized PSS at 800°C	1	97.19	2.37	null	0.44	null	71.55	17.70	10.75
	2	97.01	2.45	0.55	null	null	71.17	17.76	11.07
	3	97.53	2.47	null	null	null	71.93	17.95	10.12
	Avg	97.24	2.43	null	null	null	71.55	17.80	10.65
	SD	0.26	0.05	-	-	-	0.38	0.13	0.48
	RSD	0.27	2.18	-	-	-	0.53	0.73	4.54

null = cannot be detected
Avg = Average
SD = Standard deviation
RSD = Relative standard deviation

Interestingly, Cr and Ni were not present in palladium layer in case of Pd/Oxidized PSS at 800°C comparing to Pd/PSS and Pd/Oxidized PSS at 450°C. The surface of porous stainless steel oxidized at 800°C should contains Fe_2O_3, NiO, and Cr_2O_3. Tanabe and Imoto [79] used SEM to show the lava like Fe oxide on PSS 316 L type stainless steel after oxidation at 800°C in air. Moreover, Sivaramon *et al.* [80] reported that the oxide layer consisted of chromium oxide (Cr_2O_3) after oxidation at 700°C in air.

Among these metal oxides, Cr_2O_3 can inhibit the intermetallic diffusion probably due to the Tamman temperature of Cr_2O_3 which is much higher than the working temperature of the palladium membrane. However, the thickness of Cr_2O_3 from oxidation of porous stainless steel might not be enough to prevent intermetallic diffusion completely.

4.6.4 Chromium oxide layer by using electroplating and oxidation

From section 4.6.3, it was found that chromium oxide was possibly used as an intermetallic diffusion barrier, but a certain thickness of chromium oxide was required to inhibit the metal diffusion completely. Accordingly, the porous stainless steel disk was firstly plated with chromium by the chromium electroplating technique using a chromic acid solution and concentrated sulfuric acid in the ratio of CrO_3/H_2SO_4 (100/1) at 50-55°C with 31 A/dm^2 of current density. The chromium plating apparatus was exhibited in Figure 4.47.

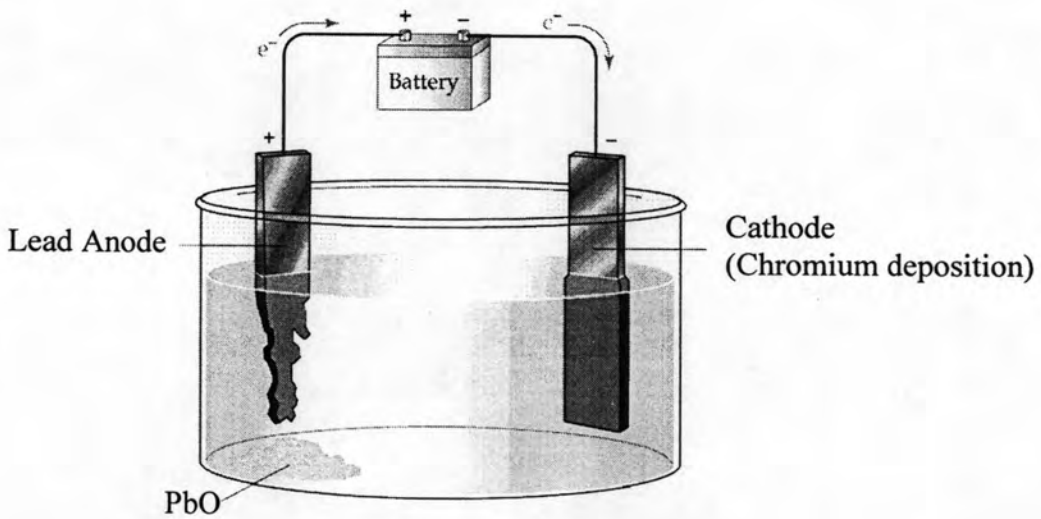

Figure 4.47 Chromium plating apparatus.

The chemical reaction of chromium plating taking place was explained by Ref. [82] as following

At the cathode, deposition of metallic chromium takes place accompanied by the liberation of hydrogen and the reduction of hexavalent chromium (CrO_3) to trivalent chromium (Cr_2O_3). The reaction was shown in equations 4.12 to 4.14.

Deposition of chromium

$$Cr_2O_7^{2-} + 14H^+ + 12e^- \longrightarrow 2Cr + 2H_2O \quad 4.12$$

Evolution of hydrogen gas

$$2H^+ + 2e^- \longrightarrow H_2 \quad 4.13$$

Formation of chromium (III)

$$Cr_2O_7^{2-} + 14H^+ + 6e^- \longrightarrow 2Cr^{3+} + 7H_2O \quad 4.14$$

At the anode, liberation of oxygen is accompanied by the oxidation of trivalent of hexavalent chromium, i.e., the regeneration of chromic acid. The reaction was exhibited in equations 4.15 to 4.17.

Evolution of oxygen gas

$$2H_2O \longrightarrow O_2 + 4H^+ + 4e^- \quad 4.15$$

Oxidation of chromium (III) to chromium (VI)

$$2CR^{3+} + 6H_2O \longrightarrow 2CrO_3 + 12H^+ + 6e^- \quad 4.16$$

Formation of lead oxide

$$Pb + 2H_2O \longrightarrow PbO_2 + 4H^+ + 4e^- \quad 4.17$$

The SEM images of porous stainless steel after chromium plating were exhibited in Figure 4.48.

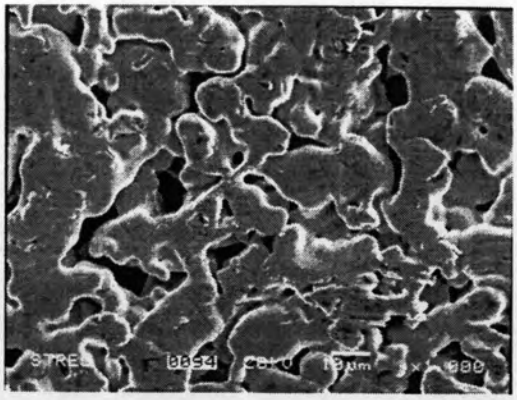

Before chromium plating (1000x)

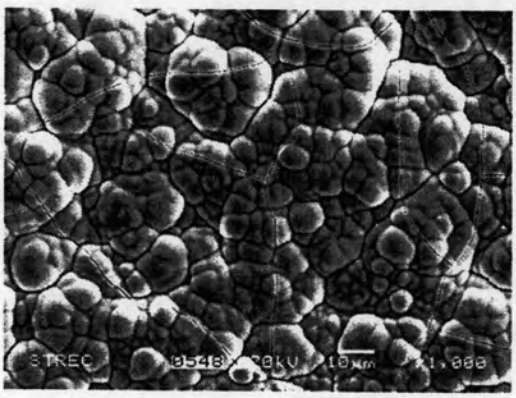

After chromium plating (1000x)

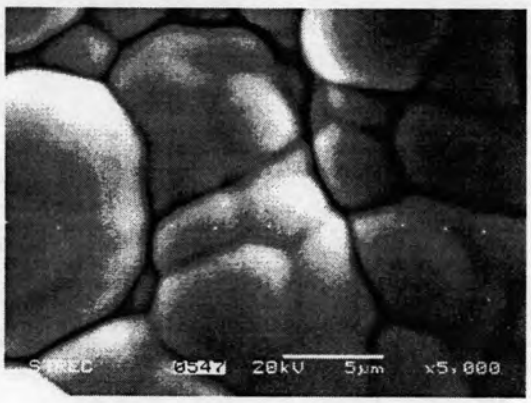

After chromium plating (5000x)

Figure 4.48 SEM micrographs of porous stainless steel disk before and after chromium electroplating.

Its surface became rough and there was some streaks on its surface because of hydrogen embrittlement caused by hydrogen generated during chromium plating. In addition. Moreover, the composition of surface was investigated by SEM and EDS. The result is shown in Figure 4.49.

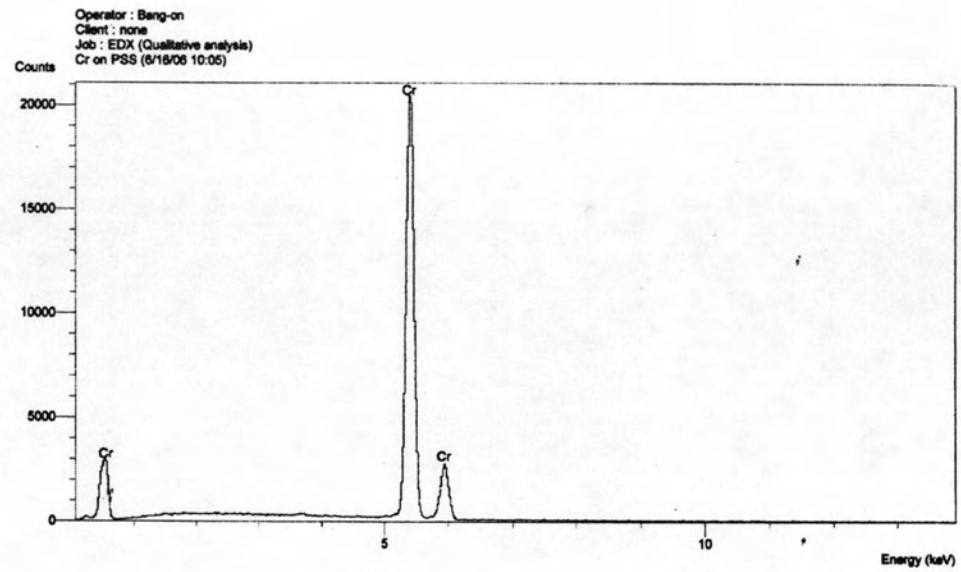

Figure 4.49 EDS spectrum of chromium plated on porous stainless steel disk.

Its EDS spectrum confirmed that chromium was deposited on the porous stainless steel disk.

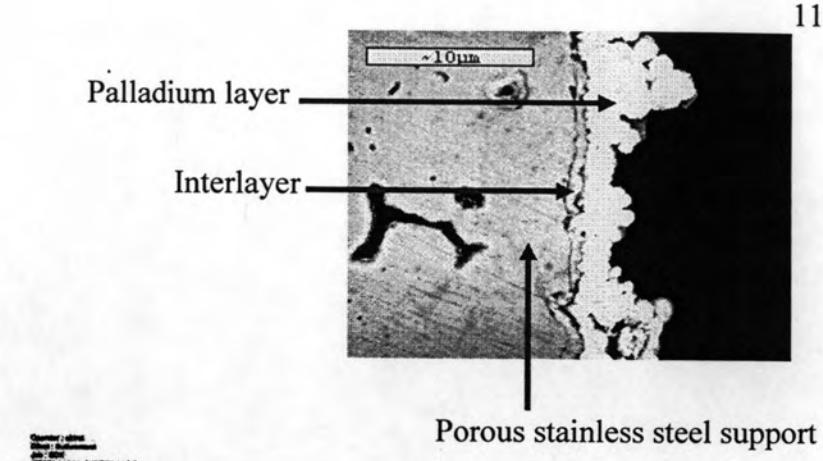

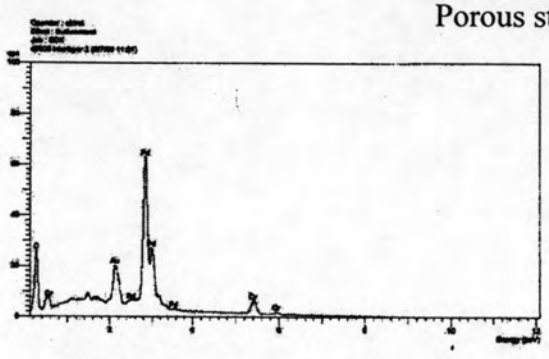

(a) EDS spectrum of palladium layer.

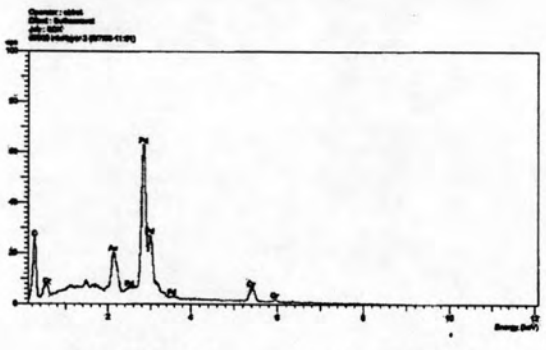

(b) EDS spectrum of interlayer.

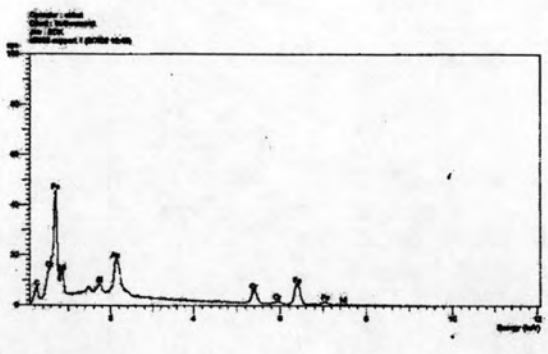

(c) EDS spectrum of porous stainless steel support.

Figure 4.50 SEM micrograph (2500x) and EDS spectra of the cross-section Pd/Cr/Oxidized (800°C) PSS disk exposed in helium at 500°C for 24 hours.

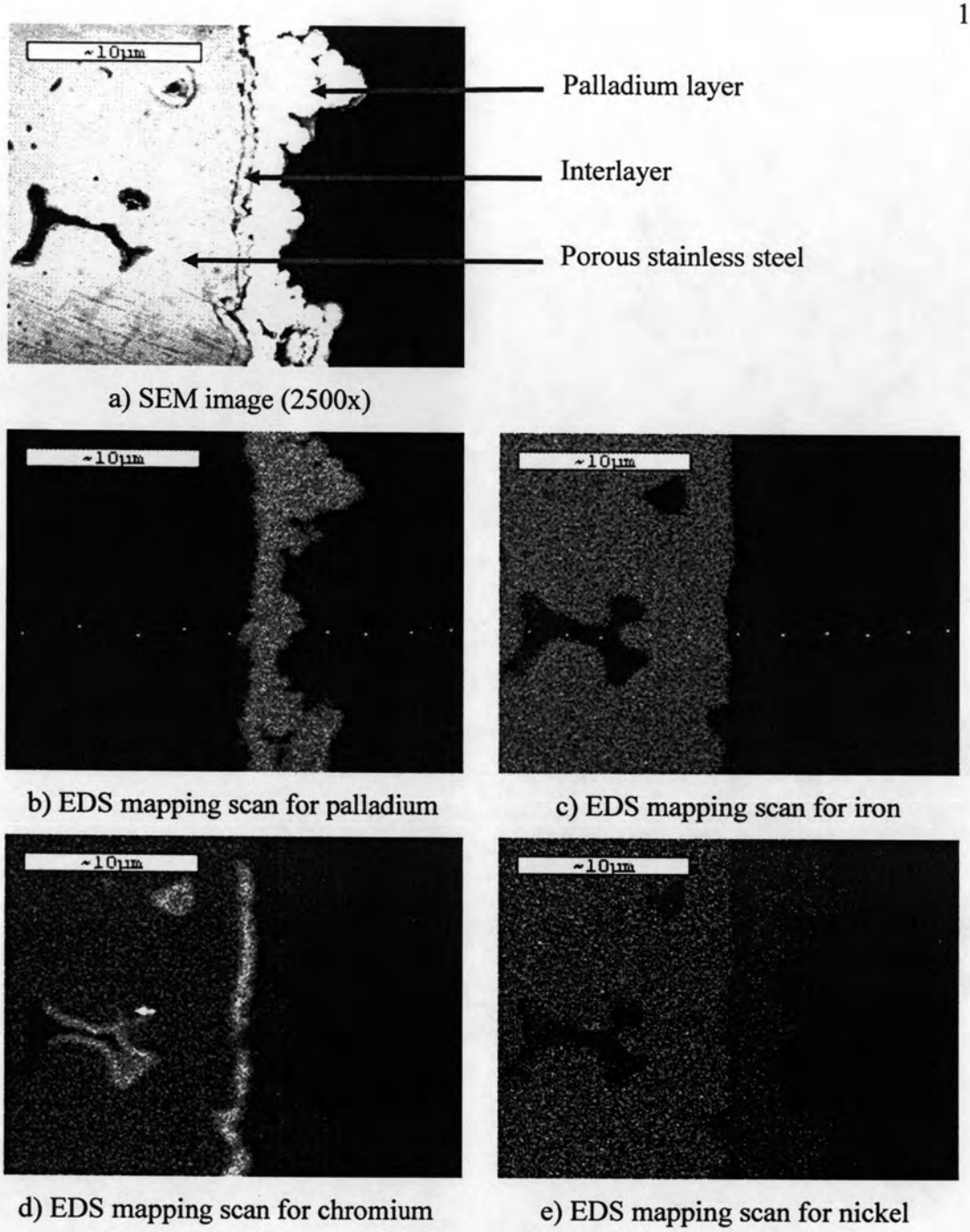

Figure 4.51 SEM micrographs (2500x) with EDS mapping scan of the cross-section Pd/Cr/Oxidized (800°C) PSS disk exposed in helium at 500°C for 24 hours.

Table 4.8 The metal distribution in palladium layer and porous stainless steel of Pd/Cr/Oxidized (800°C) PSS disk exposed in helium atmosphere at 500°C for 24 hours

		Pd layer (%)				Interlayer (%)				Porous stainless steel (%)			
		Pd	Fe	Cr	Ni	Pd	Fe	Cr	Ni	Pd	Fe	Cr	Ni
Pd/Cr/PSS	1	82.73	0.40	16.85	null	86.40	null	13.34	null	null	66.49	30.13	3.46
	2	79.72	0.41	19.74	null	91.18	null	8.42	null	null	69.63	26.98	3.68
	3	82.91	0.47	16.26	null	91.75	null	7.86	null	null	67.93	28.49	3.23
	Avg	81.79	0.43	17.62	null	89.78	null	9.87	null	null	68.02	28.53	3.46
	SD	1.79	0.04	1.86	null	2.94	null	3.02	null	null	1.57	1.58	0.23
	RSD	2.19	8.87	10.57	null	3.27	null	30.54	null	null	2.31	5.52	6.51

null = cannot be detected
Avg = Average
SD = Standard deviation
RSD = Relative standard deviation

It was found that chromium was successfully deposited on the surface of porous stainless steel disk by electroplating. However, the diffusion of Fe and Cr from porous stainless steel into the palladium layer. It can be concluded that the chromium metal could not be used as the intermetallic diffusion.

Since Tamman temperature of Cr_2O_3 is 1081°C which is higher than chromium metal, It may be used as an intermetallic diffusion barrier. Therefore, the porous stainless steel disk was cleaned and oxidized at 800°C. Then the treated porous stainless steel disk was plated with the chromium later by electroplating. To create the chromium oxide layer, the plated disk was oxidized at 800°C for 6 hours in air. Its color was dark green and its morphology was as shown in Figure 4.52 and 4.53.

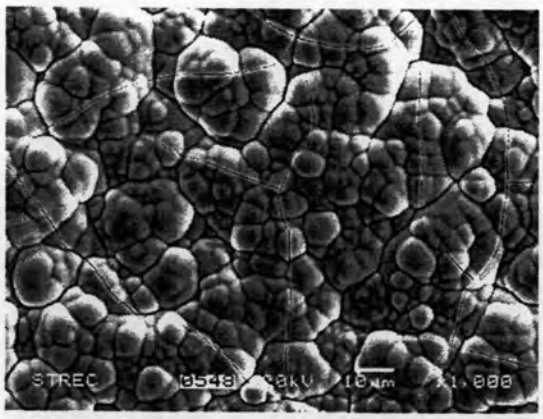

Before oxidation (1000x)

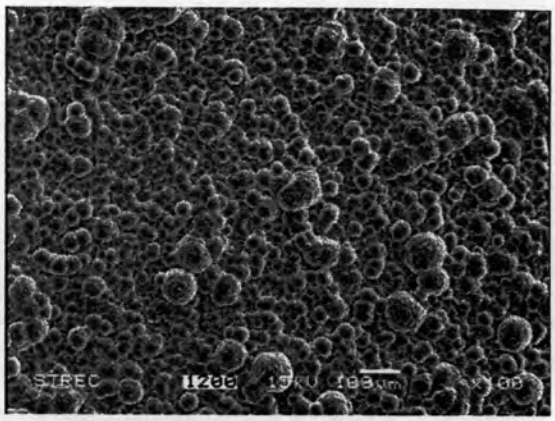

After oxidation (100x)

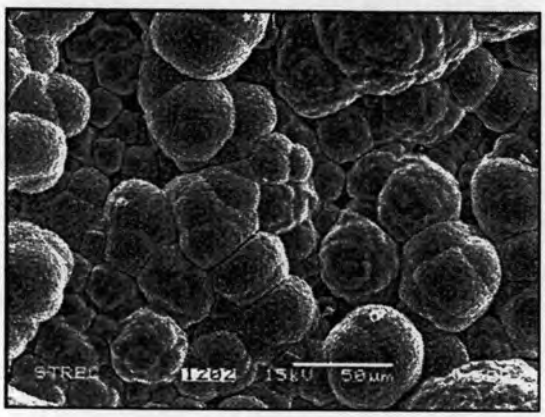

After oxidation (500x)

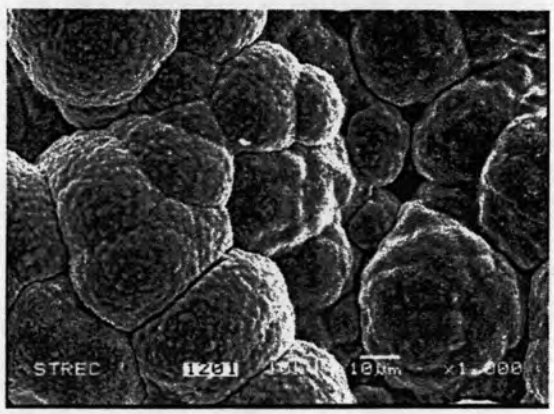

After oxidation (1000x)

Figure 4.52 SEM micrographs of chromium oxide layer on porous stainless steel disk.

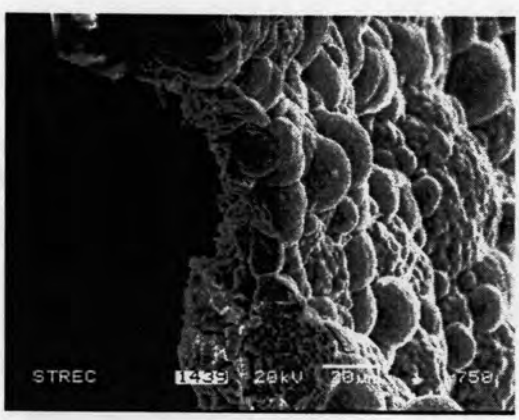

SEM image (750 x)

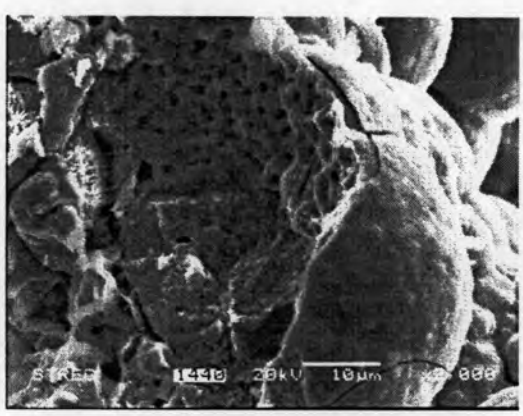

SEM image (2000 x)

Figure 4.53 SEM micrographs of chromium oxide layer (cross-section).

It exhibited obviously that the surface of Cr_2O_3 layer was round and rough. It was also found that Cr_2O_3 was porous. In addition, EDS spectrum in Figure 4.54 revealed that chromium oxide was present in this layer.

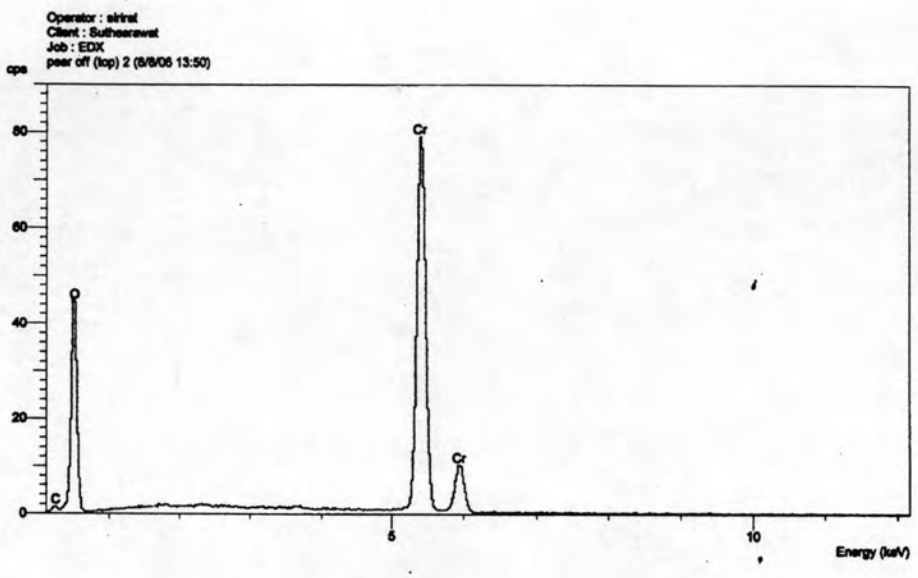

Figure 4.54 EDS spectrum of chromium oxide layer on porous stainless steel disk.

Disk at 800°C for 6 hours was plated with chromium by electroplating. Then it was oxidized at 800°C in air for 6 hours and deposited with palladium metal on top by electroless plating. It was called that Pd/Cr_2O_3/oxidized PSS at 800°C. Then the Pd/Cr_2O_3/oxidized (800°C) PSS was exposed in helium atmosphere at 500°C for 24 hours. Furthermore, the effect of chromium layer thickness was also investigated. The chromium thickness was varied from 1.2 μm to 8 μm. Both mapping scan and EDS spot scan of the cross-section are exhibited in Figures 4.55-4.64 and Table 4.9

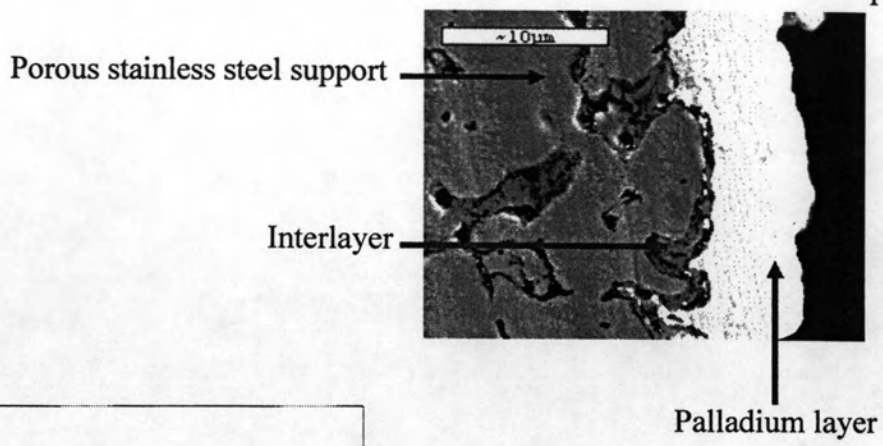

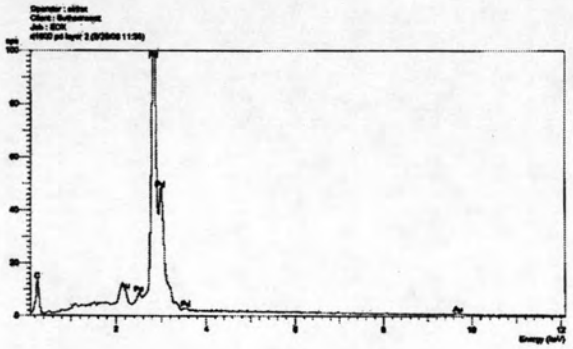

(a) EDS spectrum of palladium layer.

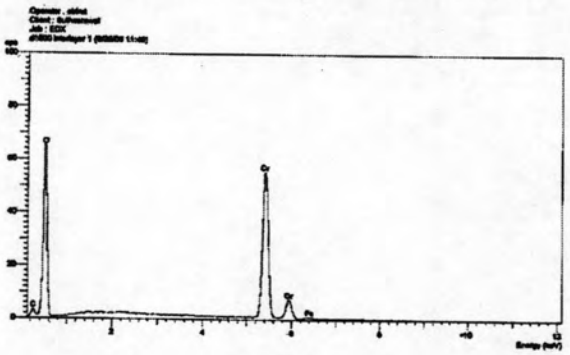

(b) EDS spectrum of interlayer.

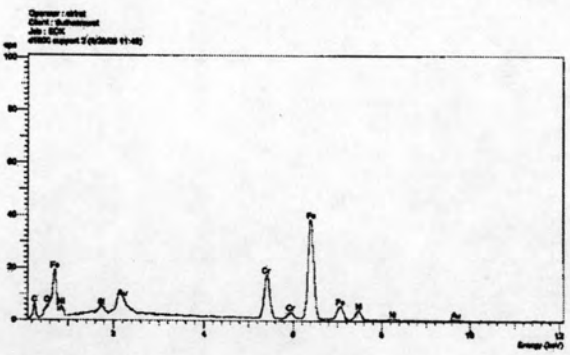

(c) EDS spectrum of porous stainless steel support.

Figure 4.55 SEM micrograph (2500x) and EDS spectra of the cross-section Pd/1.2 μm Cr_2O_3/Oxidized (800°C) PSS disk exposed in helium at 500°C for 24 hours.

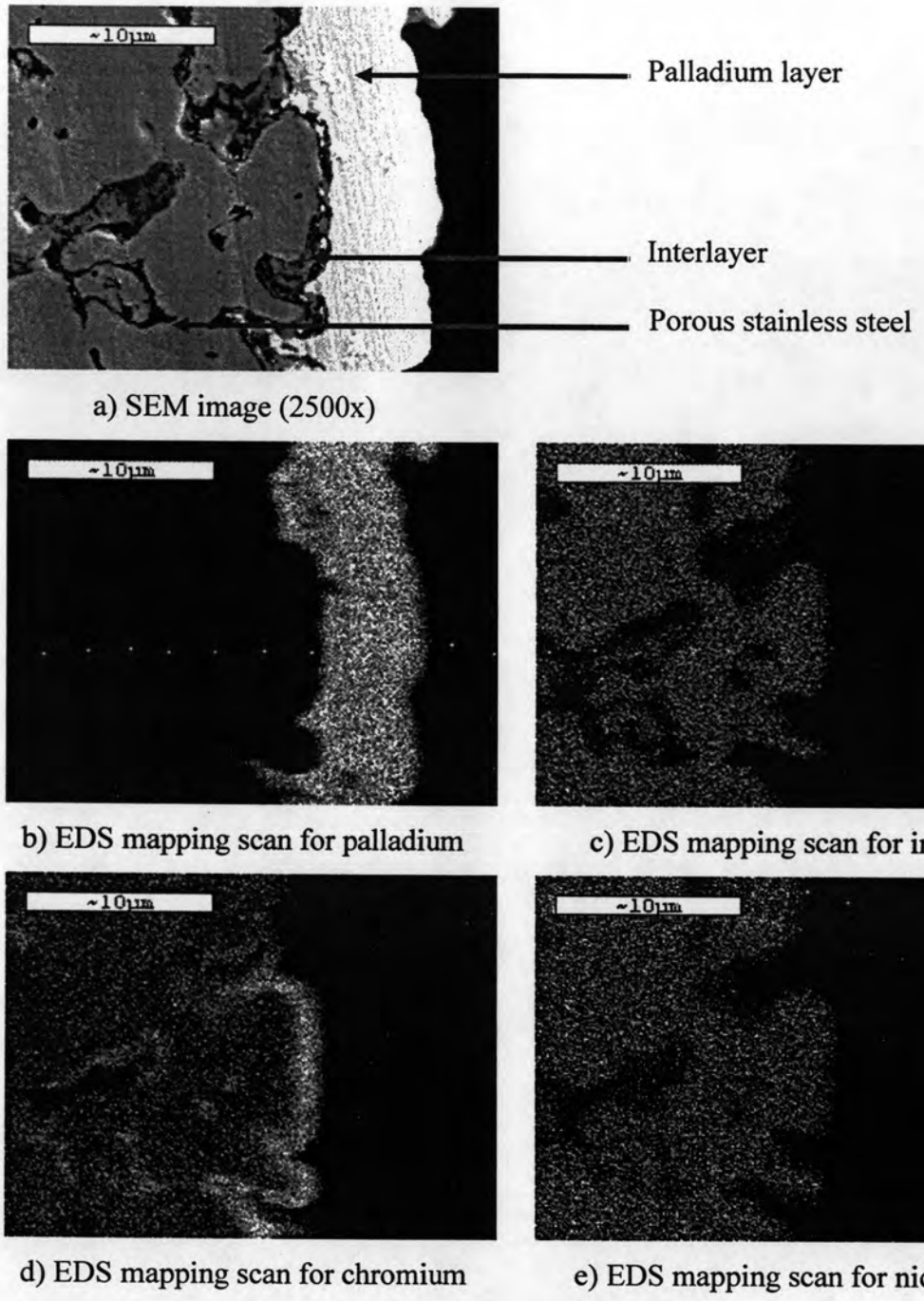

Figure 4.56 SEM micrographs (2500x) with EDS mapping of the cross-section Pd/ 1.2 μm Cr_2O_3/Oxidized (800°C) PSS disk exposed in helium at 500°C for 24 hours.

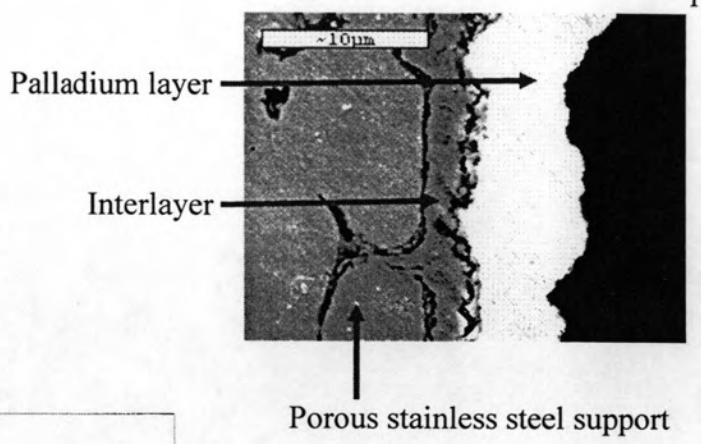

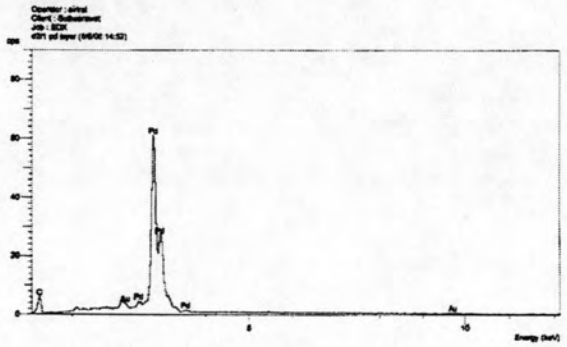

(a) EDS spectrum of palladium layer

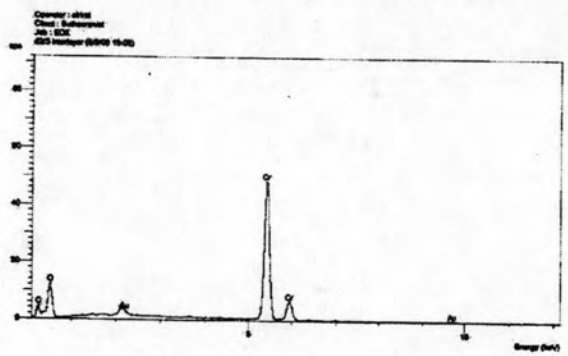

(b) EDS spectrum of interlayer

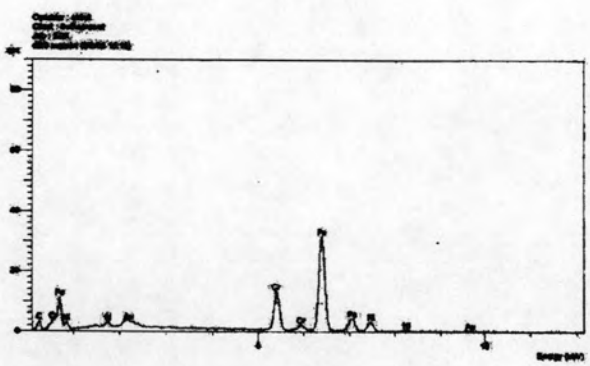

(c) EDS spectrum of porous stainless steel support

Figure 4.57 SEM micrographs (2500x) and EDS spectra of the cross-section Pd/2.0 μm Cr_2O_3/Oxidized (800°C) PSS disk exposed in helium at 500°C for 24 hours.

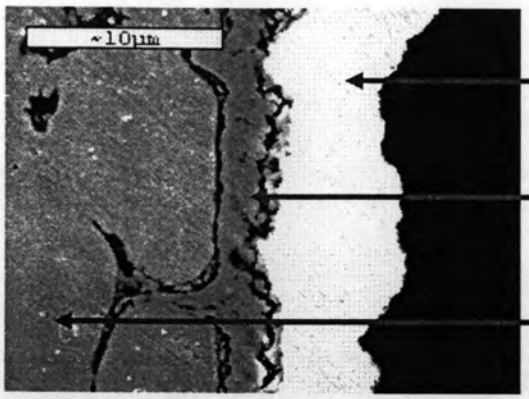

a) SEM image (2500x)

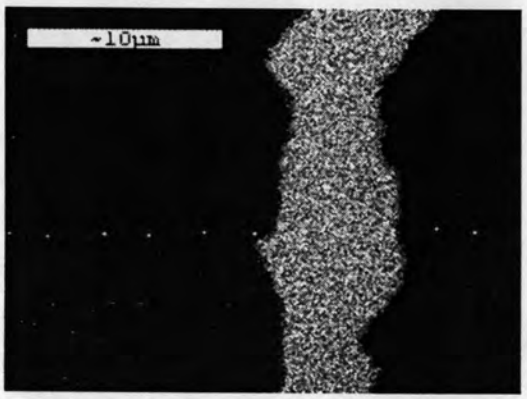

b) EDS mapping scan for palladium

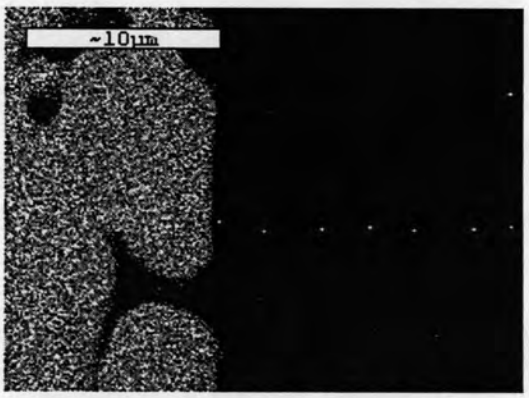

c) EDS mapping scan for iron

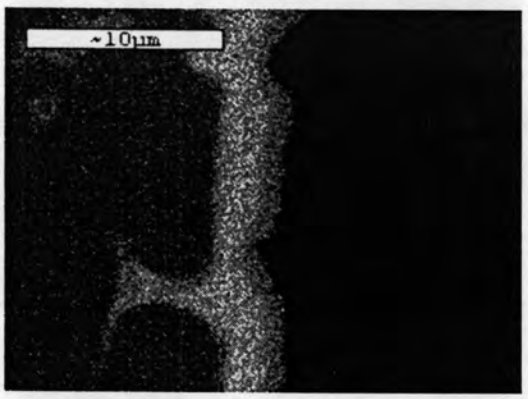

d) EDS mapping scan for chromium

e) EDS mapping scan for nickel

Figure 4.58 SEM micrographs (2500x) with EDS mapping of the cross-section Pd/ 2.0 μm Cr_2O_3/Oxidized (800°C) PSS disk exposed in helium at 500°C for 24 hours.

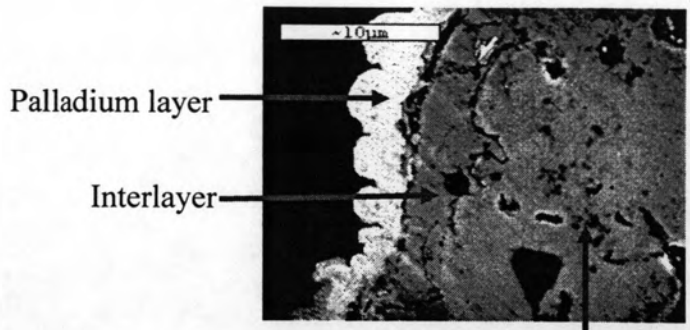

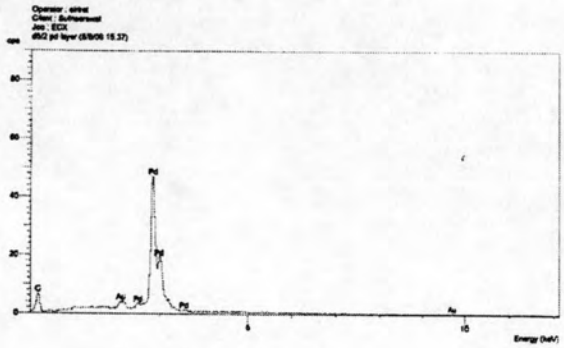

(a) EDS spectrum of palladium layer.

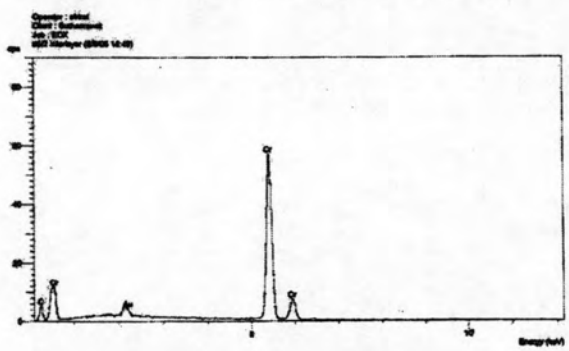

(b) EDS spectrum of interlayer.

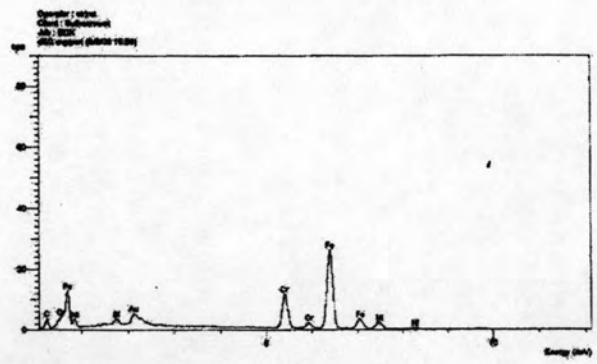

(c) EDS spectrum of porous stainless steel support.

Figure 4.59 SEM micrographs (2500x) and EDS spectra of the cross-section Pd/ 3.5 μm Cr_2O_3/Oxidized (800°C) PSS disk exposed in helium at 500°C for 24 hours.

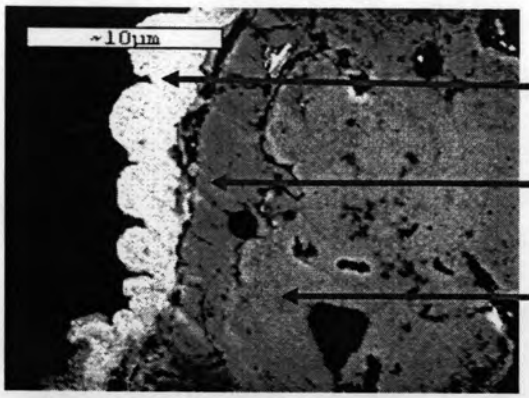

Palladium layer

Interlayer

Porous stainless steel

a) SEM image (2500x)

b) EDS mapping scan for palladium

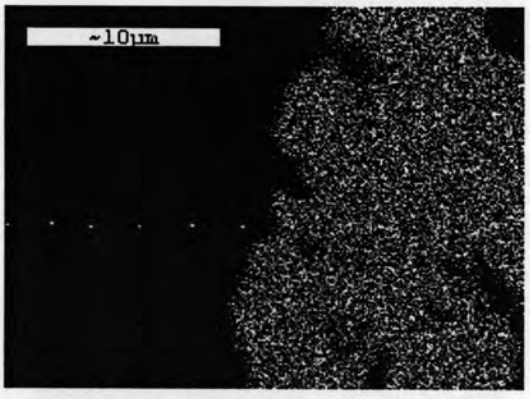

c) EDS mapping scan for iron

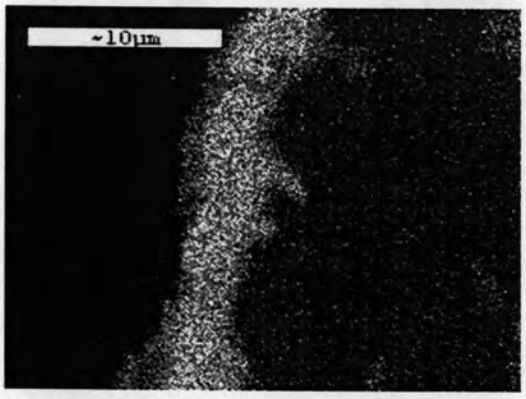

d) EDS mapping scan for chromium

e) EDS mapping scan for nickel

Figure 4.60 SEM micrographs (2500x) with EDS mapping scan of the cross-section Pd/ 3.5 µm Cr_2O_3/Oxidized (800°C) PSS disk exposed in helium at 500°C for 24 hours.

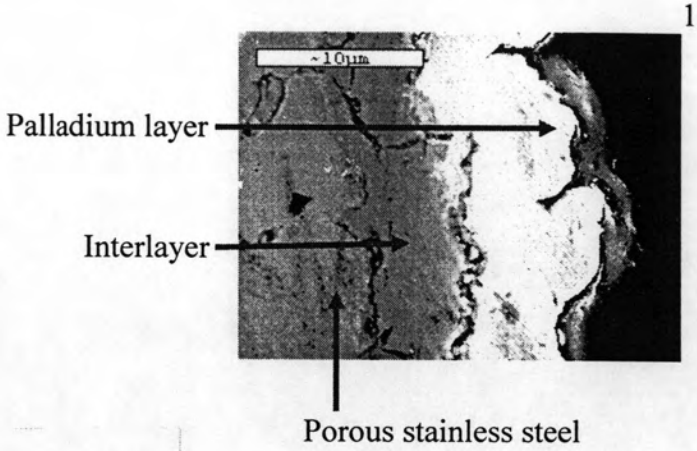

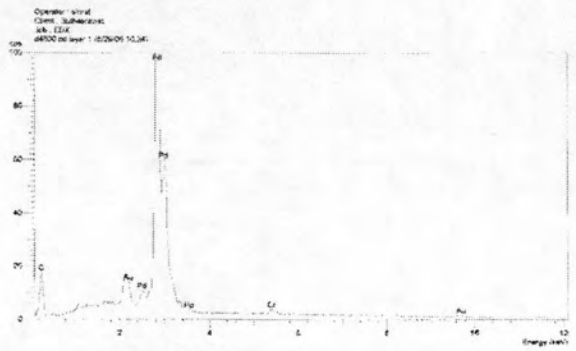

(a) EDS spectrum of palladium layer

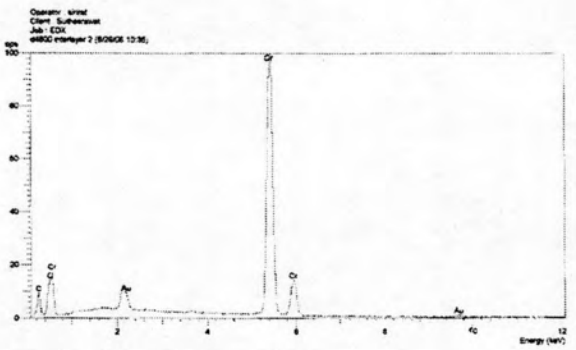

(b) EDS spectrum of interlayer

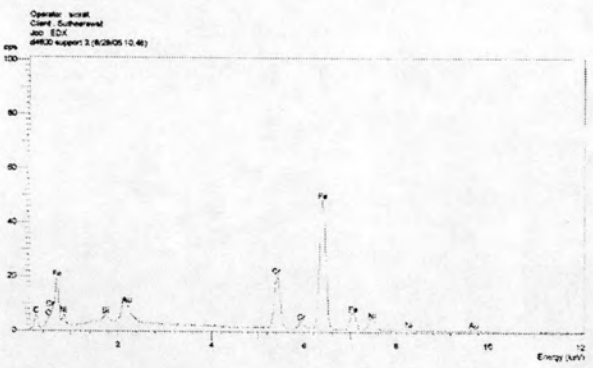

(c) EDS spectrum of porous stainless steel support

Figure 4.61 SEM micrograph (2500x) and EDS spectra of the cross-section Pd/ 6.5 µm Cr_2O_3/Oxidized (800°C) PSS disk exposed in helium at 500°C for 24 hours.

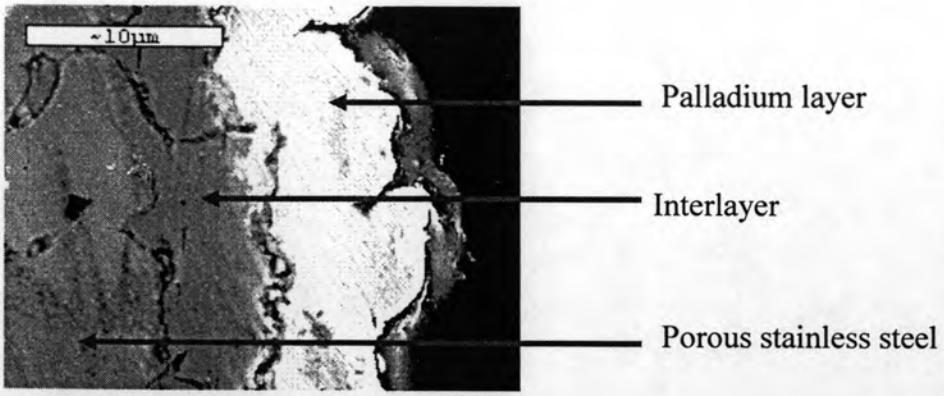

a) SEM image (2500x)

b) EDS mapping scan for palladium

c) EDS mapping scan for iron

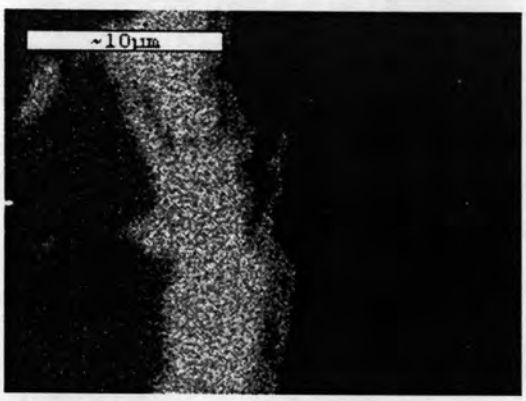

d) EDS mapping scan for chromium

e) EDS mapping scan for nickel

Figure 4.62 SEM micrographs (2500x) with EDS mapping scan of the cross-section of Pd/ 6.5 μm Cr_2O_3/Oxidized (800°C) PSS disk exposed in helium at 500°C for 24 hours.

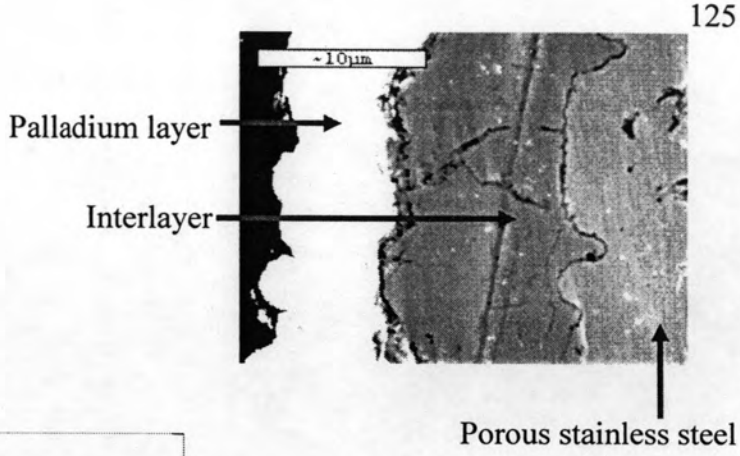

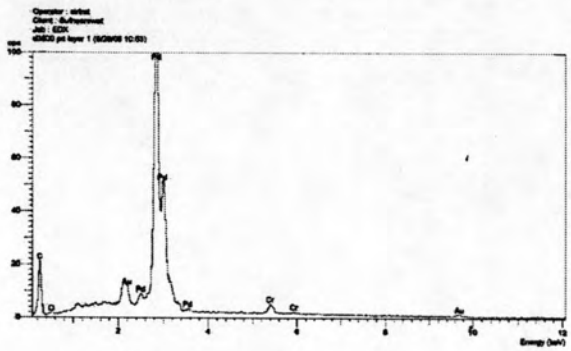

(a) EDS spectrum of palladium layer

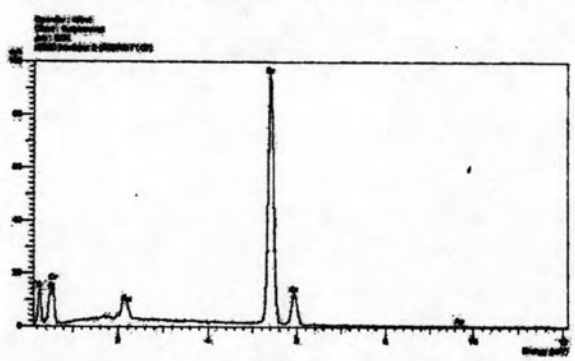

(b) EDS spectrum of interlayer

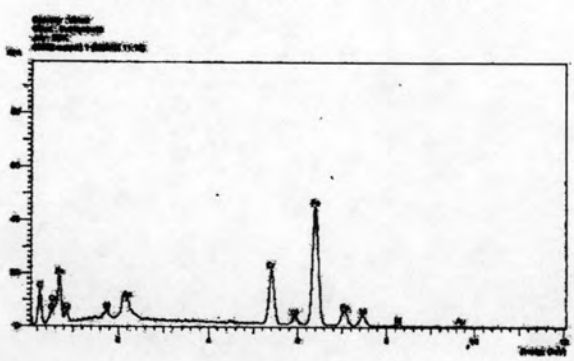

(c) EDS spectrum of porous stainless steel support

Figure 4.63 SEM micrograph (2500x) and EDS spectra of the cross-section Pd/8 μm Cr_2O_3/Oxidized (800°C)PSS disk exposed in helium at 500°C for 24 hours.

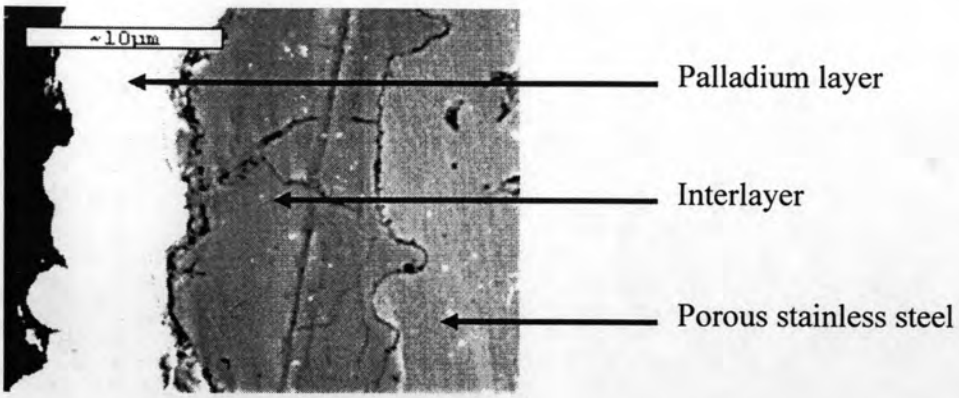

a) SEM image (2500x)

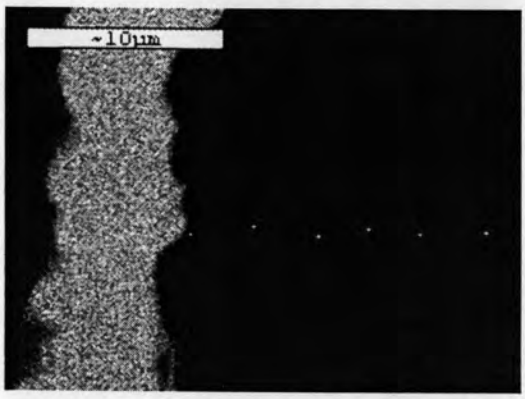

b) EDS mapping scan for palladium

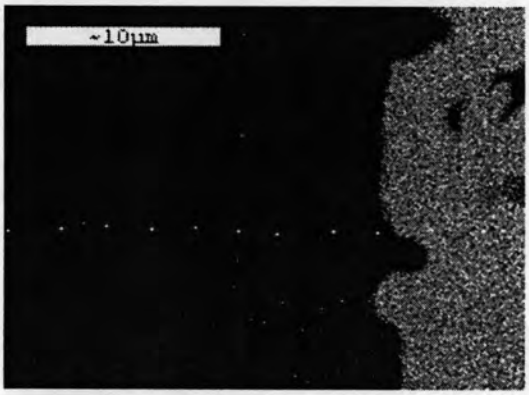

c) EDS mapping scan for iron

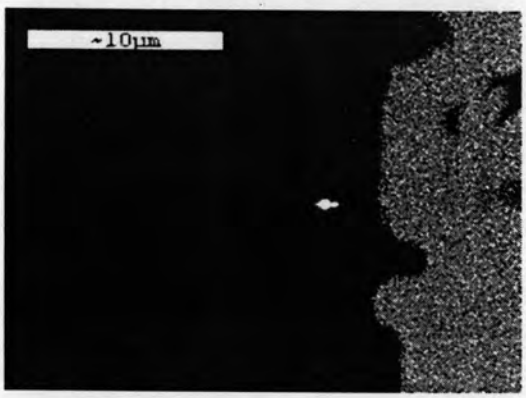

d) EDS mapping scan for chromium

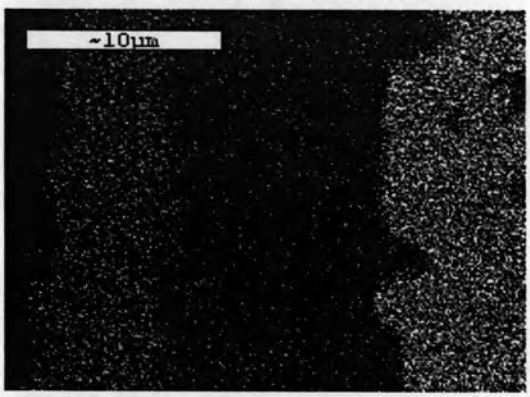

e) EDS mapping scan for nickel

Figure 4.64 SEM micrographs (2500x) with EDS mapping of the cross-section Pd/ 8 μm Cr_2O_3/Oxidized (800°C) PSS disk exposed in helium at 500°C for 24 hours.

Table 4.9 Metal distribution data of Pd/Cr2O3/PSS disk with various thicknesses

Disk number (Thickness)		Pd layer (%)				Interlayer (%)				Porous stainless steel (%)			
		Pd	Fe	Cr	Ni	Pd	Fe	Cr	Ni	Pd	Fe	Cr	Ni
1 (1.2μm)	1	100.03	null	null	null	null	0.98	98.67	null	null	70.92	18.52	10.09
	2	99.90	null	null	null	null	1.10	94.93	null	null	70.72	18.98	10.12
	3	98.82	0.51	null	0.49	null	1.18	98.95	null	null	71.33	18.99	9.61
	Avg	99.58	null	null	null	null	1.09	97.52	null	null	70.99	18.83	9.94
	SD	0.66	-	-	-	-	0.10	2.24	-	-	0.31	0.27	0.29
	RSD	0.67	-	-	-	-	9.26	2.30	-	-	0.44	1.43	2.88
2 (2.0μm)	1	87.95	null	null	null	null	0.59	68.25	null	null	60.09	16.62	8.41
	2	87.14	null	null	null	null	0.51	72.16	null	null	59.94	15.96	8.8
	3	85.79	null	0.34	null	null	0.54	64.23	null	null	58.77	15.1	9.29
	Avg	86.96	null	null	null	null	0.55	68.21	null	null	59.60	15.89	8.83
	SD	1.09	-	-	-	-	0.04	3.97	-	-	0.72	0.76	0.44
	RSD	1.25	-	-	-	-	7.39	5.81	-	-	1.21	4.80	4.99
3 (3.5μm)	1	85.03	null	null	null	null	1.42	72.32	null	null	47.83	12.63	7.00
	2	83.46	null	null	null	null	1.62	68.85	null	null	47.61	13.14	6.56
	3	84.42	null	0.7	null	null	1.72	61.22	null	null	45.77	13.08	6.74
	Avg	84.30	null	null	null	null	1.59	67.46	null	null	47.07	12.95	6.77
	SD	0.79	-	-	-	-	0.15	5.68	-	-	1.13	0.28	0.22
	RSD	0.94	-	-	-	-	9.63	8.42	-	-	2.40	2.15	3.27
4 (6.5μm)	1	98.65	null	2.18	null	null	0.64	99.13	null	null	69.66	19.35	10.53
	2	97.38	null	2.14	null	null	0.55	98.98	null	null	69.84	19.68	10.02
	3	97.16	null	2.17	null	1.21	0.59	98.42	null	null	70.36	19.89	9.92
	Avg	97.73	null	2.16	null	null	0.59	98.84	null	null	69.95	19.64	10.16
	SD	0.80	-	0.02	-	-	0.05	0.37	-	-	0.36	0.27	0.33
	RSD	0.82	-	0.96	-	-	7.60	0.38	-	-	0.52	1.39	3.22
5 (8.0μm)	1	98.19	null	2.32	0.42	null	null	99.96	null	null	71.47	17.33	11.22
	2	97.35	null	2.62	null	null	null	99.82	null	null	71.49	18.08	10.33
	3	96.27	0.00	2.79	null	null	null	99.65	null	null	70.86	17.92	10.90
	Avg	97.27	null	2.58	null	null	null	99.81	null	null	71.27	17.78	10.82
	SD	0.96	-	0.24	-	-	-	0.16	-	-	0.36	0.40	0.45
	RSD	0.99	-	9.24	-	-	-	0.16	-	-	0.50	2.22	4.17

null = cannot be detected
Avg = Average
SD = Standard deviation
RSD = Relative standard deviation

It was found that there was no Fe, Cr, and Ni diffusing into the palladium layer when the thickness of chromium layer was 1.2, 2.0, and 3.5 μm. However, the palladium layer was obtained the chromium metal when the thickness of chromium layer was higher than 3.5 μm,. It was because the formation of oxide layer by air oxidation at 800°C was not complete when the chromium layer was too thick. Therefore, the chromium metal could diffuse into palladium layer.

It is known that the most oxides are reduced to metallic state under hydrogen atmosphere. No reduction took place the oxides-metal interface if the inner oxide layer consists of Cr-rich phase which has a high resistance to reduction under hydrogen atmosphere even at high temperature [84]. In this case, even if the inert oxide layer is a Fe-rich phase and reduction occurs, the effectiveness of the barrier layer will not be compromised because of the presence of the stable Cr-oxide phase. It

concluded that the Cr_2O_3 layer could be used as barrier for metallic diffusion on palladium membrane at high temperature.

From this study, it was found that silver-tungsten layer, silica and chromium metal layer could not be used as an intermetallic diffusion barrier. Whereas the Cr_2O_3 layer could perfectly protect the metallic diffusion from porous stainless steel into palladium layer at 500°C for 24 hours in helium.

4.7 Preparation and characterization of palladium membrane tube with chromium oxide layer as an intermetallic diffusion barrier

4.7.1 The preparation of palladium membrane tube containing the Cr_2O_3 layer

The porous 316L stainless steel tube, 9 mm in outer diameter, 70 mm long and 1 mm thick was used as the support for palladium membrane. The porous stainless steel tube had an average pore size 0.1 μm and 17 % porosity. The porous stainless steel tube welded to non-porous stainless steel tube was purchased from Mott Metallurgical Corporation. The procedures for generating the intermetallic diffusion barrier and palladium plating are shown in Scheme 4.6.

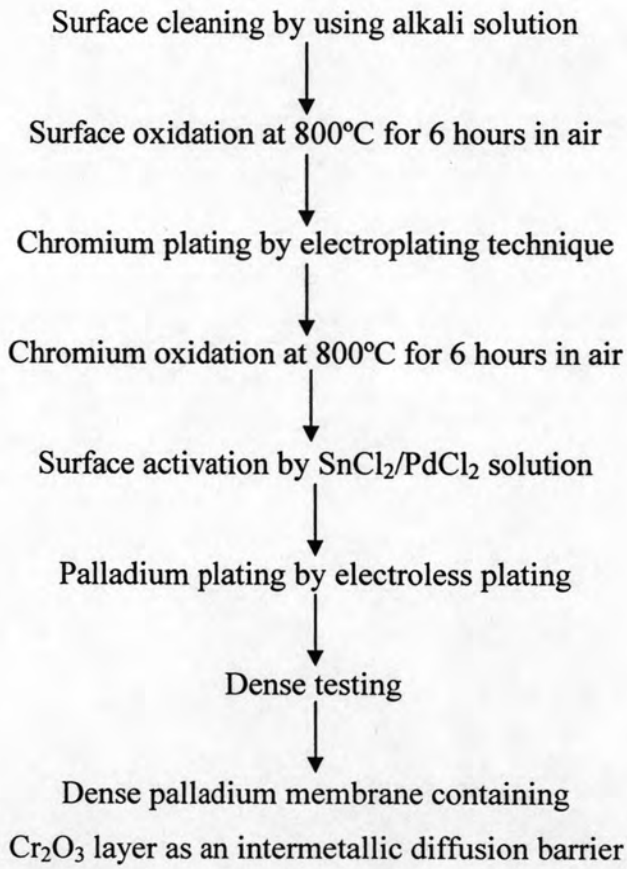

Scheme 4.6 The flow-diagram of the preparation of Pd/ Cr_2O_3/PSS tube.

It started with surface cleaning with alkali solution, chromium plating by electro plating, chromium oxidation at 800°C for 6 hours in air, surface activation by using $SnCl_2/PdCl_2$ solution, and palladium plating by palladium complex solution. The thickness of the palladium layer was determined gravimetrically.

In order to evaluate whether the prepared palladium membrane was dense, helium flux was measured by using the helium flux testing cell described in Section 3.2.3.2. If helium flux at the gas outlet could be detected, it meant that the palladium membrane tube contained some defects on its surface or it was not dense and had to be plated again. Its result was exhibited in Table 4.10.

Table 4.10 The chromium and palladium thickness and helium flux of palladium membrane tube, Tube 3

Number of plating	Weight (g)	ΔWt (g)	Thickness(μm)	He flux (m^3/m^2h)
Before Cr plating	144.42	-	-	>14.96[a]
After Cr plating#1	144.46	0.04	1.98	>14.96[a]
After Pd plating			2.78	
1	144.63	0.17	7.54	>14.96[a]
2	144.79	0.16	12.78	0.0359[b]
3	144.94	0.15	17.69	0.0003[b]
4	145.14	0.20	24.25	0.0001[b]
5	145.45	0.31	34.37	dense
Total thickness (μm)			34.37	
Chromium oxide thickness total (μm)			1.98	
Palladium thickness total (μm)			32.39	

Remark: a) gas flow rate > 500 ml/min

b) measured with capillary flow meter

From above data, in the beginning the helium flux of porous stainless steel tube was always higher than 14.96 $m^3/m^2.h$. Because of the limitation of digital gas flow meter at 500 mL/min, if gas flow is higher than 500 mL/min, the gas flow rate can not be determined. Therefore, the gas flow rate is reported as more than 500 mL/min (>500 mL/min) or higher than 14.96 $m^3/m^2.h$ for helium flux. When the

palladium thickness was thicker, the helium flux was decreased. Finally, Tube 3 was completely densed which contained 1.98 μm of chromium thickness and 32.38 μm palladium thickness. However, the palladium thickness of Tube 3 was thicker than both Tube 1 and Tube 2. This was attributed to the coarser different morphology of palladium formed (Figure 4.65) when hydrazine hydrate was used. It thus needed more palladium plating to make the membrane dense.

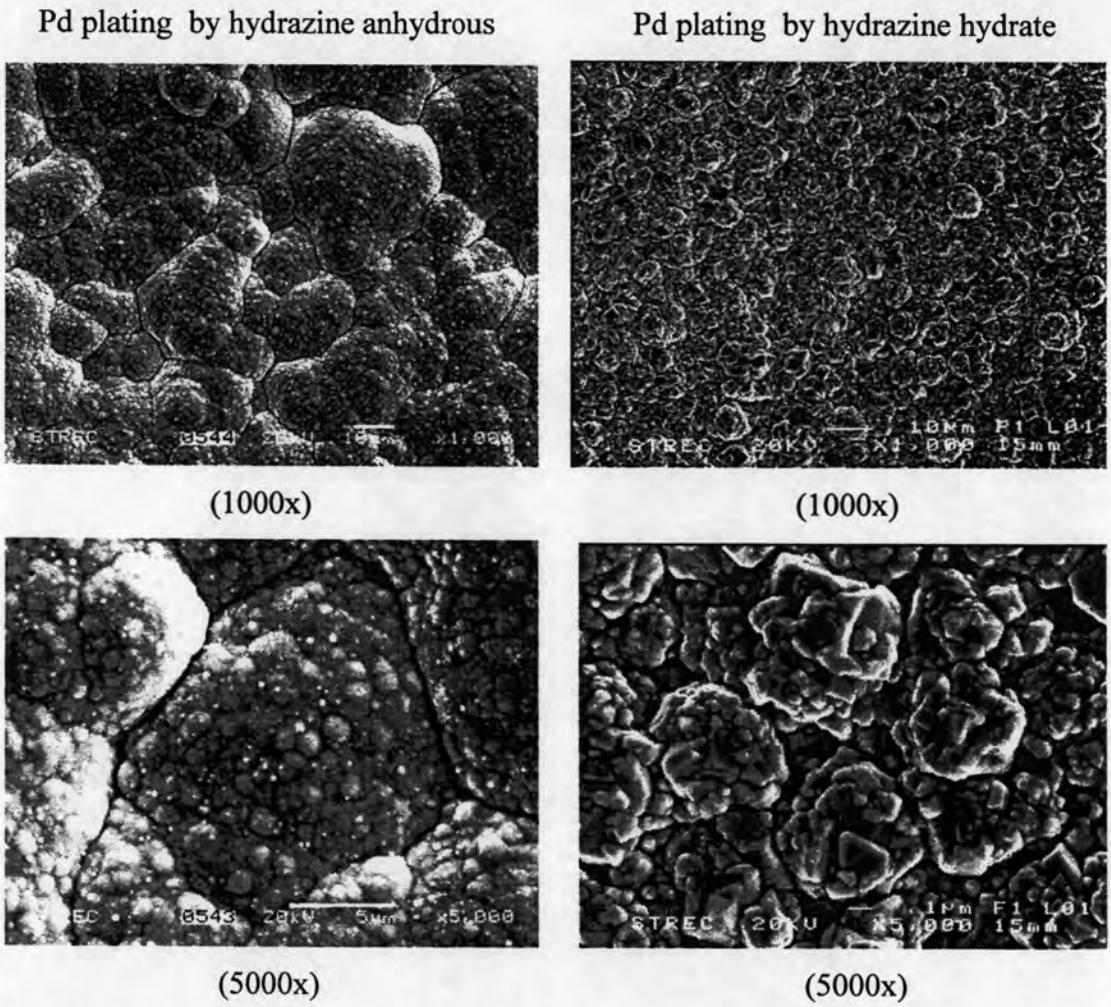

Figure 4.65 SEM micrographs of palladium layer prepared by using (a) hydrazine anhydrous (b) hydrazine hydrate.

It was found that the surface of palladium layer using the hydrazine anhydrous was smoother and flatter than the one using hydrazine hydrate. In case of using hydrazine hydrate, it was difficult to make the dense palladium membrane. It might be the reason why the thickness of tube 3 was thicker than tube 1 and tube 2.

In summary, the palladium membrane tube containing the Cr_2O_3 as an intermetallic diffusion barrier was successfully prepared with palladium thickness 32.38 μm.

4.8 The performance testing of palladium membrane tube

The above data indicated clearly that the prepared palladium membrane tube, Tube3, was the defect free dense palladium membrane tube by observing the helium flux. It was found that the helium flux of the Tube 3 could not be detected at room temperature, pressure difference 1 atm. The hydrogen permeation flux and selectivity coefficient were then evaluated at the temperature range 350–500°C.

4.8.1 Hydrogen permeation flux and selectivity coefficient

Tube 3 was assembled in the reactor and hydrogen permeation flx was measured. Not only the pressure difference but also the temperature were varied from 1-3 atm and 350-500°C, respectively. The relationship between the hydrogen permeation flux and the square root of pressure difference ($P^{0.5} - P_0^{0.5}$) was plotted as shown in Figure 4.66. The linear relationship between the hydrogen permeation flux and the difference of the square root of pressure was obtained. This was a clear indication that the Sieverts' law was followed and the slopes of the lines gave the permeance of the membrane, which are 5.6, 7.4, 9.0 and 10.9 $m^3(STP)/m^2h\text{-}atm^{0.5}$ at 350°C, 400°C, 450°C, and 500°C, respectively.

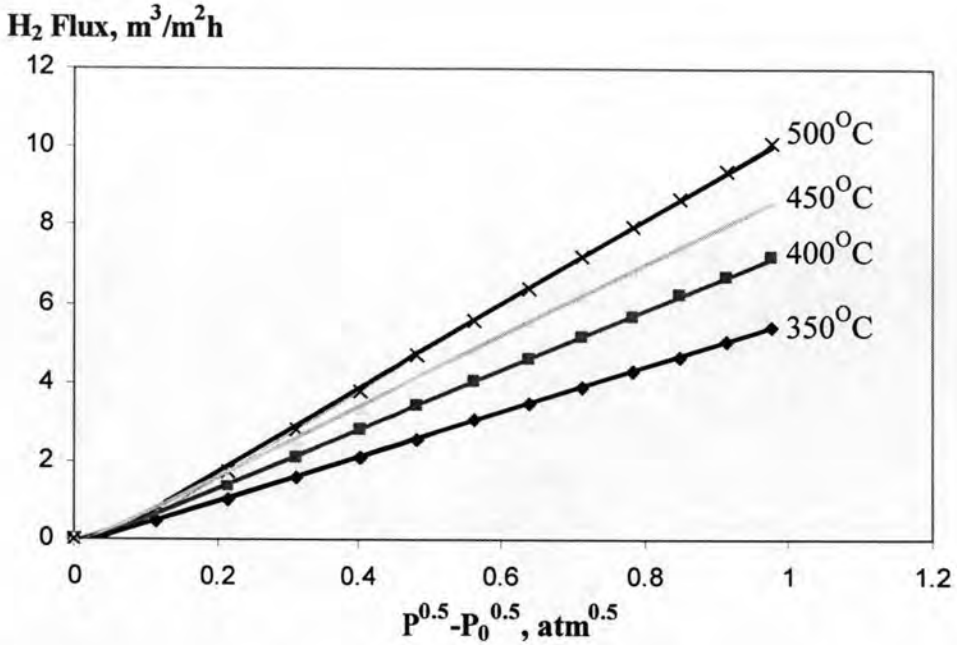

Figure 4.66 Hydrogen permeation flux of Tube 3 as a function of the square root of the pressure difference.

The hydrogen permeation also showed that the mechanism of hydrogen gas diffusing through the bulk of palladium layer was the solution-diffusion mechanism. Moreover, the rate-determining step for the hydrogen permeation of Tube 3 was the hydrogen diffusion through the bulk of palladium layer. It meant that Tube 3 was a dense palladium membrane. In term of selectivity, it was also investigated. The ideal selectivity coefficient is defined as the ratio of flux of two pure gases. In this study, hydrogen gas and helium gas were used. Since no helium flux could be detected at pressure difference 1 atm, the ideal selectivity coefficient was essentially infinite at room temperature. This strongly supported that Tube 3, a palladium membrane tube containing the Cr_2O_3 as an intermetallic diffusion barrier, was a defect free palladium membrane giving a high ideal selectivity coefficient.

4.8.2 Activation energy

The Arrhenius plot of the hydrogen permeance versus the reciprocal of the absolute temperature is shown in Figure 4.67.The activation energy of hydrogen permeation was calculated from the slope of the straight line to be 17.6 kJ/mol, which was consistent with values reported in the literatures [85-87].

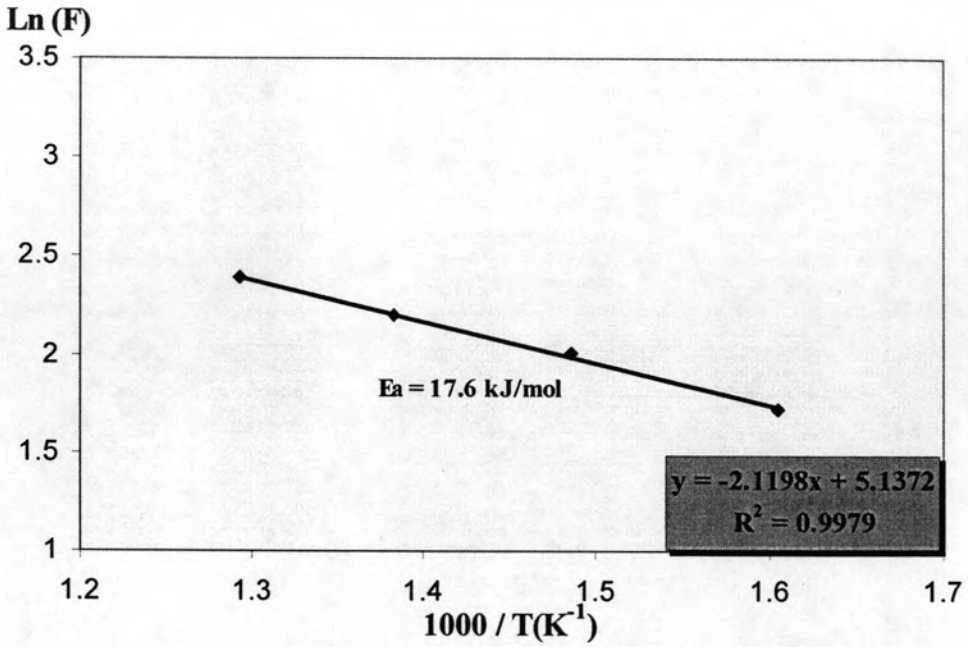

Figure 4.67 Arrhenius relations between the hydrogen permeation and invert operation temperature of tube 3 with 32um thickness.

Moreover, in order to compare the performance of Cr_2O_3 as an intermetallic diffusion barrier, the hydrogen permeation flux measurement at pressure difference 1 atm of palladium membrane tube without Cr_2O_3 and Tube 3, the palladium membrane containing the Cr_2O_3 versus temperature was shown in Figure 4.68.

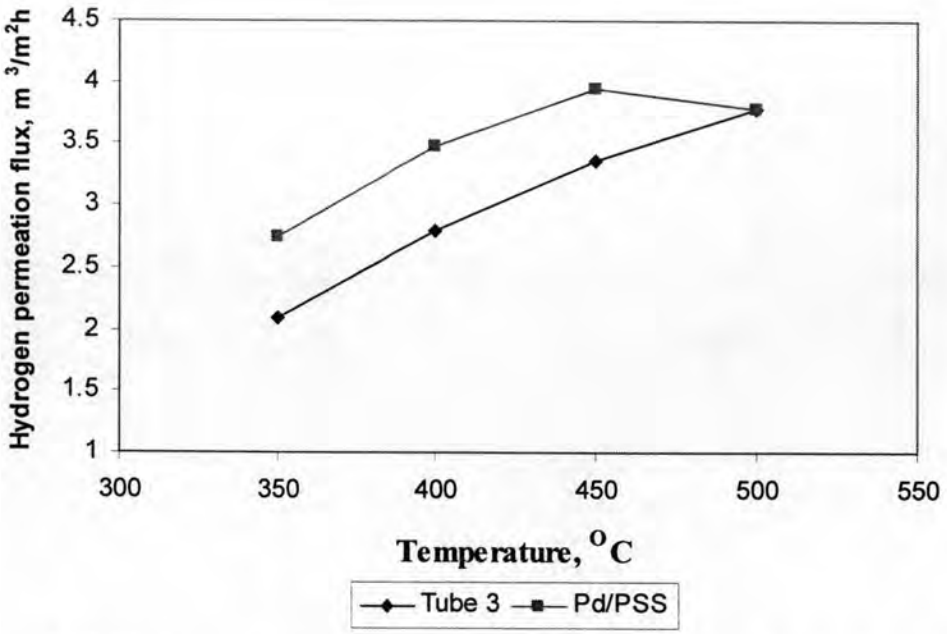

Figure 4.68 Hydrogen permeation flux versus temperature of palladium membrane with / without Cr_2O_3 in hydrogen atmosphere at various temperature for 24 hours.

It was found that the hydrogen permeation flux of palladium membrane tube without Cr_2O_3 layer started to deviate when the temperature was higher than 450°C. Whereas the hydrogen permeation flux of Tube 3 was not declined at 500°C. However, the hydrogen permeation flux of Tube 3 was lower than the previous one at every temperature except equal at 500°C. This is probably due to the higher thickness of palladium membrane Than tube 3. It can be concluded that Cr_2O_3 could protect the intermetallic diffusion at 500°C.

In summary, when palladium membrane supported on porous stainless steel was operated a temperature higher 450°C, the hydrogen permeation flux was declined because of intermetallic diffusion. In order to overcome this problem, the intermetallic diffusion barrier was applied in between palladium layer and porous stainless steel. Silver-tungsten layer, silica, metal oxide layer from oxidation of porous stainless steel, chromium layer, and chromium oxide layer were studied. It was found that the most suitable barrier was chromium oxide layer because chromium oxide was stable at high temperatures even under reducing atmosphere. However, the proper thickness of the chromium oxide layer should be about 1.2 – 3.5 μm. The Cr_2O_3 was formed by chromium electroplating and chromium oxidation in air at

800°C for 6 hours. In addition, the palladium membrane tube containing Cr_2O_3 as a barrier was successfully prepared with 2 μm chromium thickness and 32 μm palladium thickness.